Impact of Dynamical Fermions on the Vacuum of Quantum Chromodynamics

Peter John Moran

Supervisor: Derek B. Leinweber

The University of Adelaide
School of Chemistry and Physics
Discipline of Physics

February 2010

Chapter 1

Introduction

In his seminal paper of 1974 [1] Wilson formulated a technique for quantising a continuum gauge theory onto a hypercubic grid or lattice. This work eventually lead to the formation of a new field of study in the area of high energy particle physics, Lattice Quantum Chromodynamics (QCD). As is well known, the self interactions of gluons render the empty vacuum unstable to the formation of nontrivial quark and gluon fields, which alter significantly the long distance behaviour of quarks. This inhibits the traditional approach of perturbation theory for studying QCD in the low energy regime. In Lattice QCD, the introduction of a regulator through the finite distance between nodes, allows researchers to perform *ab initio* investigations into QCD. Since Wilson's paper, a dedicated effort from the Lattice QCD community has produced a wealth of information on how to simulate QCD using modern computational techniques. Excellent starting points for the new researcher include Refs. [2–4].

It is currently a very interesting and exciting time to be a researcher in the field of Lattice QCD. The advanced algorithms and compute resources currently available are enabling the first studies of full dynamical QCD towards the physical point of the quark mass parameter space. This will enable predictions from QCD to be directly compared with experiment, in the search for possible physics beyond the standard model.

In the author's opinion, a primary attraction of Lattice QCD is not just its ability to compare with experiment, but is also the way in which lattice simulations can be used to provide researchers with information otherwise unattainable through standard experimental methods. This allows researchers to gain a deeper understanding of the quantum mechanical processes and indeed the *physics* that underlies the experimentally observed results. It is for this reason that studies of the topological structure of the QCD vacuum are so fascinating.

We begin in the next few sections by providing a short introduction to Quantum Chromodynamics, the calculation of expectation values, and topology in QCD. Following this, the lattice approach is briefly outlined in Sec. 1.4, after which a sample lattice calculation of the strong coupling constant α_s is presented in Sec. 1.5. This calculation serves to highlight the effectiveness of Lattice QCD, whilst also emphasising the need to carefully monitor and control the errors and methodologies of lattice simulations. Finally, an outline of the remainder of the thesis is provided in Sec. 1.6.

1.1 Quantum Chromodynamics

In the Standard Model of particle physics the strong interactions are described by the theory of Quantum Chromodynamics. These are the interactions between quarks and gluons, quarks being those particles which combine together to form all baryons and mesons in the universe and carry a colour charge (red, green, or blue).

Due to the presence of these three colour charges, gauge fields in Lattice QCD are represented mathematically as elements of the $SU(3)$ group. The $SU(3)$ group is composed of all complex 3×3 matrices that are unitary, $U^\dagger U = U U^\dagger = \mathbb{I}$, and have determinant 1. The non-Abelian[1] nature of the $SU(3)$ group gives rise to asymptotic freedom; at short distances the effective quark-gluon and gluon-gluon coupling becomes small.

The QCD Lagrangian density, which governs the motion of strongly interacting particles, is given by

$$\begin{aligned} \mathcal{L}_{QCD} &= \bar{\psi}(x)\,(i\gamma^\mu D_\mu - m)\,\psi(x) - \frac{1}{2}\mathrm{tr}(F_{\mu\nu}F^{\mu\nu}) \\ &= \mathcal{L}_F + \mathcal{L}_G\,, \end{aligned} \tag{1.1}$$

where γ^μ are the Dirac γ-matrices, D_μ is the covariant derivative

$$D_\mu \equiv \partial_\mu + igA_\mu\,, \tag{1.2}$$

and the field strength tensor $F_{\mu\nu}$ is defined by

$$igF_{\mu\nu} \equiv [D_\mu, D_\nu]\,. \tag{1.3}$$

The gauge fields, and thus also the field strength tensor, are proportional to the generators of $SU(3)$

$$A_\mu(x) = \sum_{a=1}^{8} \frac{\lambda^a}{2} A^a_\mu(x)\,, \qquad F_{\mu\nu}(x) = \sum_{a=1}^{8} \frac{\lambda^a}{2} F^a_{\mu\nu}(x)\,, \tag{1.4}$$

where the λ^a are the generators of the SU(3) group. The generators are represented as 3×3 traceless Hermitian matrices satisfying $\mathrm{tr}(\lambda^a\lambda^b) = \delta^{ab}$ and $\left[\frac{\lambda^a}{2}, \frac{\lambda^b}{2}\right] = if^{abc}\frac{\lambda^c}{2}$, where the f^{abc} are the totally antisymmetric structure constants [5].

The QCD action is the space-time integral of the Lagrangian density (1.1)

$$\begin{aligned} S_{QCD} &= \int d^4x\, \mathcal{L}_{QCD}(\psi, \bar{\psi}, A_\mu) \\ &= \int d^4x\, \bar{\psi}(x)\,(i\gamma^\mu D_\mu - m)\,\psi(x) - \frac{1}{2}\int d^4x\, \mathrm{tr}(F_{\mu\nu}F^{\mu\nu}) \\ S_{QCD} &= S_F + S_G\,, \end{aligned} \tag{1.5}$$

which is often separated into the fermionic and gluonic components respectively. The Lagrangian density (1.1) and action (1.5) are necessarily invariant under both global SU(3) transformations

$$\begin{aligned} \psi(x) &\to G\,\psi(x)\,, \\ \bar{\psi}(x) &\to \bar{\psi}(x)\,G^{-1}\,, \end{aligned} \tag{1.6}$$

where $G = e^{i\omega^a\lambda_a}$ is x-independent, and local SU(3) transformations

[1] A non-Abelian group G is one for which $A, B \in G \Rightarrow AB \neq BA$ in general.

$$\begin{aligned}
\psi(x) &\rightarrow G(x)\,\psi(x)\,, \\
\bar{\psi}(x) &\rightarrow \bar{\psi}(x)\,G^{-1}(x)\,, \\
A_\mu(x) &\rightarrow G(x)\,A_\mu(x)\,G^{-1}(x) - \frac{i}{g}G(x)\,\partial_\mu(G^{-1}(x))\,,
\end{aligned} \tag{1.7}$$

with $G(x) = e^{i\omega^a(x)\lambda_a}$. It is these symmetries that give rise to colour charge conservation in the theory.

For our lattice simulations it will be necessary to work in Euclidean space-time. To shift from Minkowski to Euclidean space-time we make the substitutions $x^0 \rightarrow -ix_4$ and[2] $A^0 \rightarrow +iA_4$. Upon making these substitutions the Euclidean action is given by [3]

$$iS^{Min} \rightarrow -S^{Eucl}\,, \tag{1.8}$$

with

$$\begin{aligned}
S^{Eucl}_{QCD} &= \int d^4x \bar{\psi}(x)(\gamma_\mu D_\mu + m)\psi(x) + \frac{1}{2}\int d^4x\,\mathrm{tr}(F_{\mu\nu}F_{\mu\nu}) \\
&\equiv S^{Eucl}_F + S^{Eucl}_G\,,
\end{aligned} \tag{1.9}$$

where we have selected to use a Euclidean metric $g_{\mu\nu} = \delta_{\mu\nu}$, and the γ-matrices are defined in the Sakurai [6] representation (see App. B).

1.2 Expectation values

Observables in QCD can be calculated by computing the vacuum expectation values of the relevant operators using the Feynmann path integral formalism. For some generic fields ϕ_i, the vacuum expectation value is given by [7]

$$\langle\Omega|\phi_1(x_1)\,\phi_2(x_2)\ldots|\Omega\rangle = \frac{1}{Z}\int \mathcal{D}\phi\; e^{iS(\phi)}\,\phi_1(x_1)\,\phi_2(x_2)\ldots\,, \tag{1.10}$$

where $|\Omega\rangle$ denotes the vacuum state,

$$Z = \int \mathcal{D}\phi\; e^{iS(\phi)}\,, \tag{1.11}$$

and $\mathcal{D}\phi$ represents an integral over all possible field values at all possible points in space-time. If we then switch to Euclidean space using Eq. (1.8), the weight factor becomes $e^{-S^{Eucl}}$. Thus, when the integral is replaced by a sum on the lattice, the evaluation of correlation functions becomes a statistical problem, that can be solved using Monte Carlo techniques.

If we now apply this methodology to QCD using the action in Eq. (1.9), then for some operator, or product of operators

$$O(\psi,\bar{\psi},A_\sigma) = O_1(\psi,\bar{\psi},A_\sigma)\,O_2(\psi,\bar{\psi},A_\sigma)\ldots\,, \tag{1.12}$$

[2] To see this, consider the case where A_μ is a pure gauge field, $A_\mu = \partial_\mu\omega^a(x)\lambda_a$. Then $x^0 \rightarrow -ix_4$ implies $\partial_0 \rightarrow +i\partial_4$. [3]

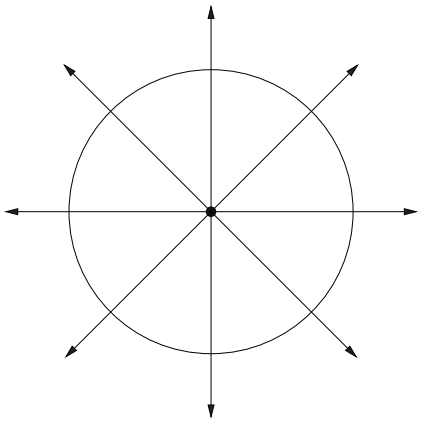

Figure 1.1: A single point test charge with a closed loop that encircles the charge.

we find

$$\langle\Omega|O(\psi,\bar{\psi},A_\sigma)|\Omega\rangle = \frac{1}{Z}\int \mathcal{D}\psi\,\mathcal{D}\bar{\psi}\,\mathcal{D}A_\sigma\; O(\psi,\bar{\psi},A_\sigma)\,e^{-S_F^{Eucl}-S_G^{Eucl}}\,, \tag{1.13}$$

with

$$Z = \int \mathcal{D}\psi\mathcal{D}\bar{\psi}\mathcal{D}A_\sigma\; e^{-S_F^{Eucl}-S_G^{Eucl}}\,. \tag{1.14}$$

The fermion fields ψ, $\bar{\psi}$ anti-commute $\{\psi_\mu,\psi_\nu\}=0$ and are described mathematically by Grassmann variables. The integrals over ψ, $\bar{\psi}$ can therefore be evaluated analytically using Grassmann algebra, giving [3],

$$\langle\Omega|O(\psi,\bar{\psi},A_\sigma)|\Omega\rangle = \frac{1}{Z}\int \mathcal{D}A_\sigma\; O(M^{-1},A_\sigma)\,\det(\not{D}+m)\,e^{-\frac{1}{2}\int d^4x\;\mathrm{tr}(F_{\mu\nu}F_{\mu\nu})}\,, \tag{1.15}$$

where the operator O in the integrand depends on the inverse of the fermion matrix $M \equiv \not{D}+m$ evaluated over the gauge fields A_σ. M^{-1} describes how the particles associated with ψ, $\bar{\psi}$ propagate through the vacuum. The determinant describes the roles of quark loops in the vacuum and is renowned for being difficult to simulate due to computational demands. From Eq. (1.15) it is clear that observables are calculated as path integrals over all possible vacuum gauge field configurations A_σ.

1.3 Topology and instantons

The work of this thesis focuses primarily on the topological structure of the QCD vacuum. In order to introduce the concept of topology, consider the simple case of a single point charge with electric field lines radiating outwards. Now suppose we are interested in some closed loop that encircles this charge, such as that depicted in Fig. 1.1. Beginning at some point on the loop, take the unit vector defined by the direction of the electric field at that point, and integrate the vector around the loop. As the vector is moved around the loop the vector will rotate, and we see that by the time the vector has returned to its initial point it will have gone through a single 360° rotation. Such a process is depicted in Fig. 1.2. It therefore seems reasonable to associate a *winding*

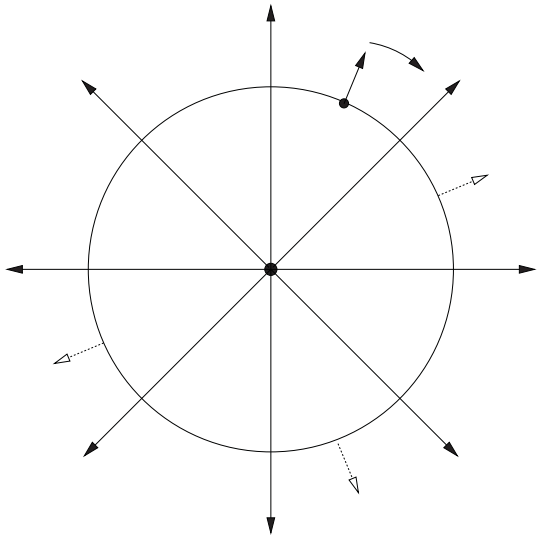

Figure 1.2: As a unit vector pointing in the direction of the electric field moves around the closed loop it will perform a full 360° rotation. Here the vector starts in the top right and circles clockwise around the loop.

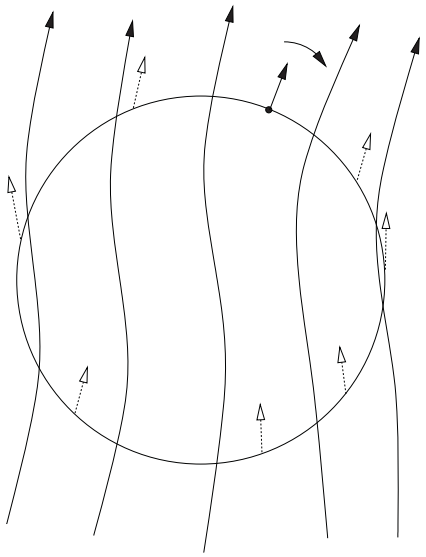

Figure 1.3: An example of a closed loop where the unit vector pointing in the direction of the electric field will not perform a rotation as it moves around the path.

number of 1 (corresponding to one rotation of the vector) to the closed path, and we can refer to this winding number as the topological charge Q. Another example of a closed loop is depicted in Fig. 1.3. In this case, we see that as the unit vector, pointing in the direction of the electric field, is integrated around the loop it will never perform an entire rotation. In this case we therefore have $Q = 0$.

In any gauge theory, it is also possible to associate a integer valued winding number, or topological charge, with the gauge fields. For Quantum Chromodynamics one has,

$$Q \equiv \int d^4x\, q(x) = \frac{g^2}{32\,\pi^2} \int d^4x\, \epsilon_{\mu\nu\rho\sigma}\, \mathrm{tr}\, \left(F_{\mu\nu}(x) F_{\rho\sigma}(x)\right) . \tag{1.16}$$

To derive such a formula one typically works in an $SU(2)$ subgroup of $SU(3)$ and considers the mapping of a three-sphere in four-dimensional Euclidean space to $SU(2)$ space. The final chapter of Ref. [5] provides a nice discussion.

We would like to know what, if any, topological objects in the QCD vacuum contribute to the topological charge. One such object is the "pseudo-particle" solution, known as the instanton, which was discovered in 1975 by Belavin, *et al.* [8].

The instanton is a minimal action solution to the Yang-Mills $SU(2)$ equation,

$$S_{\mathrm{YM}} = \frac{1}{2} \int d^4x\, \mathrm{tr}(F_{\mu\nu} F_{\mu\nu})\,. \tag{1.17}$$

Using the relation,

$$\frac{1}{4} \int d^4x\, \mathrm{tr}(F_{\mu\nu} \pm \tilde{F}_{\mu\nu})^2 \geq 0\,, \tag{1.18}$$

along with,

$$(F_{\mu\nu} \pm \tilde{F}_{\mu\nu})^2 = 2(F_{\mu\nu}\, F_{\mu\nu} \pm F_{\mu\nu}\, \tilde{F}_{\mu\nu})\,, \tag{1.19}$$

and the properties $F_{\mu\nu}\, F_{\mu\nu} = \tilde{F}_{\mu\nu}\, \tilde{F}_{\mu\nu}$, and $F_{\mu\nu}\, \tilde{F}_{\mu\nu} = \tilde{F}_{\mu\nu}\, F_{\mu\nu}$ one can see that,

$$S_{\mathrm{YM}} \geq \left| \frac{1}{2} \int d^4x\ \mathrm{tr}(F_{\mu\nu}\, \tilde{F}_{\mu\nu}) \right| . \tag{1.20}$$

The equality occurs when $F_{\mu\nu} = \mp \tilde{F}_{\mu\nu}$ and the field is *self-dual*. The instanton provides a non-trivial solution and is given by [8],

$$A_\mu(x) = \frac{x^2}{x^2 + \rho^2} \left(\frac{i}{g}\right) \partial_\mu(S)\, S^{-1}\,, \tag{1.21}$$

with

$$S = \frac{x_4 \pm i\, \vec{x} \cdot \vec{\sigma}}{\sqrt{x^2}}\,, \tag{1.22}$$

where the $\vec{\sigma}$ are the usual Pauli matrices, ρ denotes the size of the instanton, and the $+$ corresponds to an instanton whilst the $-$ corresponds to anti-instantons. Here, $\vec{\sigma}$ resides in the $SU(2)$ colour space. The solution links the spatial and colour degrees of freedom.

Instantons have an integer topological charge $Q = \pm 1$, and allow tunnelling between vacuum states which differ by a unit of topological charge. Isolated instantons also give

rise to exact zero eigenmodes of the Dirac operator [9], with zeromodes from instantons having positive chirality, and anti-instanton zeromodes having negative chirality.

In the present work we will focus on the presence (or absence) of instanton-like objects in gauge fields generated from Monte Carlo simulations. As such we are primarily interested in topology in lattice simulations, rather than the phenomenological applications of instantons. For a discussion of instanton related phenomenology in QCD see the review of Ref. [9].

Another reason why topology is interesting is that the topological charge density appears in a resolution to the $U(1)$ problem [10]. In the massless limit, the continuum QCD Lagrangian observes the $U(1)_V \times U(1)_A \times SU(3)_L \times SU(3)_R$ symmetry. The spontaneous breaking of the chiral $SU(3)_L \times SU(3)_R$ symmetry in nature gives rise to a set of near-massless bosons, the three pions and octet of 0^- mesons. The current corresponding to the $U(1)_V$ symmetry is

$$j^B_\mu(x) \equiv \bar{\psi}(x)\,\gamma_\mu\,\psi(x)\,, \tag{1.23}$$

and manifests itself as baryon number conservation. The relevant current for the $U(1)_A$ symmetry is

$$j^5_\mu(x) \equiv \bar{\psi}(x)\,\gamma_\mu\gamma_5\psi(x)\,, \tag{1.24}$$

but in this case, there is no corresponding physical symmetry observed in nature. Therefore, one would expect this symmetry to be realised as a Goldstone mode, with a corresponding massless Goldstone boson, however no such particle exists. The possible candidate, the η' meson, is far heavier than the π, K and η mesons, and is therefore excluded. This is the so-called $U(1)$ problem.

A resolution to this problem is provided by the non-conservation of the flavour singlet axial current,

$$\partial_\mu\, j^5_\mu(x) = 2N_f\, q(x)\,, \tag{1.25}$$

where N_f is the number of flavours, which is proportional to the topological charge density introduced previously.

The Adler-Bell-Jackiw axial anomaly of Eq. (1.25) means that the $U(1)_A$ symmetry of the classical continuum Lagrangian is not present in the quantum theory, and therefore the η' does not become a Goldstone boson in the massless limit. Formally, the mass of the η' can be related to the topological susceptibility,

$$\chi \equiv \frac{\langle Q^2\rangle}{V} = \int d^4x \langle q(x)q(0)\rangle\,, \tag{1.26}$$

through the Witten-Veneziano formula,

$$\chi^{Que} \simeq \frac{f_\pi^2}{4N_f}(m^2_{\eta'} + m^2_\eta - 2m^2_K)\,, \tag{1.27}$$

where the topological susceptibility must be calculated in pure Yang-Mills theory, i.e. quenched QCD. The topology of QCD vacuum can therefore be studied through the non-perturbative calculation of $q(x)$ using the techniques of the Lattice QCD.

1.4 Lattice QCD

The lattice formalism provides the ability to perform non-perturbative, *ab initio* calculations of QCD expectation values in Euclidean space. We will now present a brief introduction to the various techniques of Lattice QCD. The material presented will be developed further in later chapters as is necessary.

As we have already seen, the path integral formalism provides the following formula for calculating the expectation value $\langle O \rangle \equiv \langle \Omega | O(\psi, \bar{\psi}, A_\sigma) | \Omega \rangle$ of some operator O,

$$\langle O \rangle = \frac{1}{Z} \int \mathcal{D}A_\sigma \; O(A_\sigma)\, e^{-\int d^4x\, \mathcal{L}(A_\sigma)} \,, \tag{1.28}$$

where $\mathcal{L} = \frac{1}{2}\int d^4x \; \mathrm{tr}(F_{\mu\nu}F_{\mu\nu}) - \ln\det(\not{D} + m)$ is the effective QCD Lagrangian. This infinite dimensional integral is calculated by approximating continuous space-time with a 4-dimensional grid, or lattice. Typically the spatial length of the lattice is denoted L_s, and the lattice spacing a is the distance between nodes. Because of this discretisation, derivatives are replaced with finite differences,

$$\partial_\mu f(x) \to \frac{1}{2a}\left[f(x + a\hat{\mu}) - f(x - a\hat{\mu}) \right] \,, \tag{1.29}$$

and integrals are replaced with finite sums,

$$\int d^4x \to a^4 \sum_x \,. \tag{1.30}$$

On our lattice, the fermion fields ψ will reside on the nodes of the lattice while the gauge fields A_μ exist as *gauge links* between the nodes. All variables on the lattice are also replaced by their dimensionless counterparts[3],

$$m \;\to\; \frac{1}{a}\, m \,, \tag{1.31}$$

$$\psi(x) \;\to\; \frac{1}{a^{3/2}}\, \psi(x) \,, \tag{1.32}$$

$$\bar{\psi}(x) \;\to\; \frac{1}{a^{3/2}}\, \bar{\psi}(x) \,, \tag{1.33}$$

$$\partial_\mu \psi(x) \;\to\; \frac{1}{a^{5/2}}\, \partial_\mu \psi(x) \,. \tag{1.34}$$

Monte Carlo techniques are then used to generate a number, N, of typical vacuum gauge field configurations $U(A_\mu)$, with a fixed-point probability distribution of $\frac{1}{Z} e^{-\int d^4x\, \mathcal{L}(A_\mu)}$. The path integral of Eq. (1.28) is then easily calculated as a sum over these gauge fields,

$$\langle O \rangle = \frac{1}{N} \sum_U O(U) \,. \tag{1.35}$$

Note that because the fermion fields are integrated out analytically, the effects of dynamical sea quarks are accounted for in the Monte Carlo generation of the gauge fields.

[3]The physical units are easily recovered by multiplying with the appropriate powers of the lattice spacing a, which has units of fm, and $\hbar c \simeq 0.197327$ GeV fm.

This means that the gauge fields are composed entirely of gauge links, and further, one can study the effects of dynamical sea quarks by directly analysing these fields.

The effects of dynamical sea quarks can be neglected in lattice simulations by setting $\det(\not{D} + m) = \text{constant}$. This is called the *quenched* approximation and is equivalent to removing vacuum polarisation effects from the simulation.

1.4.1 Gauge fields in Lattice QCD

In the continuum, the colour gauge fields A_μ describe gluons and mediate the interactions between quarks. In moving a quark from some position x to y the fermion picks up a phase factor equal to the Schwinger line integral of A_μ between x and y,

$$\psi(y) = \mathcal{P} e^{\int_x^y ig A_\mu(z)\, dz_\mu} \psi(x)\,, \tag{1.36}$$

where $\mathcal{P}$ denotes the path ordering operator. This motivates the definition of a gauge link to be the line integral of A_μ between two adjacent nodes on the lattice. For a link between x and $x + \hat{\mu}$ one has,

$$U_\mu(x) = e^{\int_x^{x+\hat{\mu}} ig A_\mu(z)\, dz_\mu} \approx e^{ig A_\mu(x+\hat{\mu})\delta_{x_\mu}}\,. \tag{1.37}$$

The reverse link going from $x + \hat{\mu}$ to x is given by $U_\mu^\dagger(x)$.

Closed products of gauge links are called Wilson loops. The simplest Wilson loop is the square, or plaquette,

$$W_{\mu\nu}(x) = U_\mu(x)\, U_\nu(x+\hat{\mu})\, U_\mu^\dagger(x+\hat{\nu})\, U_\nu^\dagger(x)\,. \tag{1.38}$$

Under a gauge transformation, we have from Eq. (1.7) that the links transform as,

$$U_\mu(x) \to G(x)\, U_\mu(x) G^{-1}(x+\hat{\mu})\,, \tag{1.39}$$
$$U_\mu^\dagger(x) \to G(x+\hat{\mu})\, U_\mu^\dagger(x) G^{-1}(x)\,. \tag{1.40}$$

For example,

$$\begin{aligned}
U_\mu(x) &\approx e^{igA_\mu(x+\hat{\mu})\delta_{x_\mu}} \\
&= 1 + ig\, A_\mu(x)\, \delta x_\mu + \mathcal{O}(\delta x_\mu^2) \\
&\to 1 + ig \left(G(x)\, A_\mu(x)\, G^{-1}(x) - \frac{i}{g} G(x)\, \partial_\mu \left(G^{-1}(x) \right) \right) \delta x_\mu + \mathcal{O}(\delta x_\mu^2) \\
&= G(x) \left(1 + ig\, A_\mu(x)\, \delta x_\mu\right) G^{-1}(x) + G(x)\, \partial_\mu \left(G^{-1}(x) \right) \delta x_\mu + \mathcal{O}(\delta x_\mu^2) \\
&= G(x) \left(1 + ig\, A_\mu(x)\, \delta x_\mu\right) \left(G^{-1}(x) + \partial_\mu \left(G^{-1}(x) \right) \delta x_\mu \right) + \mathcal{O}(\delta x_\mu^2) \\
&= G(x)\, U_\mu(x)\, G^{-1}(x+\hat{\mu})\,,
\end{aligned} \tag{1.41}$$

where we have used a Taylor expansion for $G^{-1}(x+\hat{\mu})$. Thus, the plaquette will transform as, $W_{\mu\nu}(x) \to G(x) W_{\mu\nu}(x) G^{-1}(x)$, and taking the colour trace gives a gauge invariant quantity. Using the Baker-Campbell-Hausdorff formula to expand Eq. (1.38), one finds that,

$$W_{\mu\nu}(x_0) = e^{ia^2 g\, F_{\mu\nu}(x) + O(ga^3)}\,. \tag{1.42}$$

From this one can infer a lattice transcription of the pure gauge action,

$$\begin{aligned} S_W &\equiv \beta \sum_x \sum_{\mu<\nu} \left[1 - \frac{1}{3} (\mathrm{Re}\,\mathrm{tr}\, W_{\mu\nu}) \right] \\ &= \beta \sum_x \sum_{\mu<\nu} \left[1 - \frac{1}{3} \mathrm{tr}(\mathbb{I}) + \frac{1}{6} g^2 a^4 \,\mathrm{tr}(F_{\mu\nu}^2) + O(a^6) \right] \\ S_W &= \frac{1}{2} a^4 \sum_x \sum_{\mu,\nu} \mathrm{tr}(F_{\mu\nu}^2) + O(a^6)\,, \end{aligned} \tag{1.43}$$

where we have defined the lattice coupling $\beta = 6/g^2$ to recover the continuum action. S_W is called the Wilson gauge action and has errors of $\mathcal{O}(a^2)$. In order to remove the discretisation errors, this standard action can be improved through a process known as Symanzik improvement [11]. This improvement scheme will be discussed in Chapter 2.

1.4.2 Fermion fields on the lattice

In order to construct a lattice version of the fermion action,

$$S_F = \int d^4x\, \bar{\psi}(x)\, (\not{D} + m)\, \psi(x)\,, \tag{1.44}$$

the derivatives are replaced with finite differences, and gauge links are inserted to maintain gauge invariance. The naive fermion action is thus,

$$\begin{aligned} S_N &= m \sum_x \bar{\psi}(x)\, \psi(x) + \\ &\quad \frac{1}{2a} \sum_{x,\mu} \bar{\psi}(x)\, \gamma_\mu \left[U_\mu(x)\, \psi(x+\hat{\mu}) - U_\mu^\dagger(x-\hat{\mu})\,, \psi(x-\hat{\mu}) \right] \\ &\equiv \sum_{x,y} \bar{\psi}(x)\, M_{xy}^N[U]\, \psi(y)\,, \end{aligned} \tag{1.45}$$

where the interaction matrix M^N is

$$M_{i,j}^N[U] = m\, \delta_{ij} + \frac{1}{2a} \sum_\mu [\gamma_\mu\, U_{i,\mu}\, \delta_{i,j-\mu} - \gamma_\mu\, U_{i-\mu,\mu}^\dagger\, \delta_{i,j+\mu}]\,, \tag{1.46}$$

where the sum over μ links the site i with its nearest neighbour in each dimension. The naive action of Eq. (1.45) preserves chiral symmetry, and a Taylor expansion shows that it has errors of $\mathcal{O}(a^2)$. Unfortunately, in the continuum limit the action gives rise to 16 flavours of quarks. This is easily seen by considering the inverse of the free field propagator, obtained by taking the Fourier transform of the action with all $U_\mu = 1$,

$$S^{-1}(p) = m_q + \frac{i}{a} \sum_\mu \gamma_\mu \sin p_\mu a\,, \tag{1.47}$$

which has 16 zeros within the Brillouin cell in the limit $m \to 0$,

$$p_\mu = (0,0,0,0),\ (\pi/a,0,0,0),\ (\pi/a,\pi/a,0,0)\,,\ \text{etc.} \tag{1.48}$$

This is the well known fermion doubling problem, and renders the naive fermion action unacceptable.

The fermion doublers can be removed by adding irrelevant dimension-five operators to the fermion action, such that the doublers are given an infinite mass in the continuum limit.[4] Because these extra operators are proportional to the lattice spacing a, they vanish in the continuum limit. Wilson proposed just such a fermion action, the aptly named Wilson action,

$$S_W = \bar{\psi}(x) \left[\sum_\mu \left(\gamma_\mu \nabla_\mu - \frac{1}{2} r\, a\, \Delta_\mu \right) + m \right] \psi(x) \;, \tag{1.49}$$

where r is the "Wilson coefficient" (almost always $r = 1$),

$$\nabla_\mu \psi(x) = \frac{1}{2a} [U_\mu(x)\, \psi(x + \hat{\mu}) - U^\dagger_\mu(x - \hat{\mu})\, \psi(x - \hat{\mu})] \,, \tag{1.50}$$

and

$$\Delta_\mu \psi(x) = \frac{1}{a^2} [U_\mu(x)\, \psi(x + \hat{\mu}) + U^\dagger_\mu(x - \hat{\mu})\, \psi(x - \hat{\mu}) - 2\, \psi(x)]. \tag{1.51}$$

With these definitions the interaction matrix for the Wilson action is,

$$M^W_{xy}[U]\, a = \delta_{xy} - \kappa \sum_\mu \Big[(r - \gamma_\mu)\, U_{x,\mu}\, \delta_{x,y-\mu} + (r + \gamma_\mu)\, U^\dagger_{x-\mu,\mu}\, \delta_{x,y+\mu} \Big] \,, \tag{1.52}$$

such that $S_W = \sum_{x,y} \bar{\psi}^L_x M^W_{xy} \psi^L_x$, with a field renormalisation,

$$\begin{aligned} \kappa &= 1/(2\, m_q\, a + 8\, r) \,, \\ \psi^L &= \psi/\sqrt{2\,\kappa} \,. \end{aligned} \tag{1.53}$$

The Wilson action in Eq. (1.49) has no doublers for $r > 0$ as the Wilson term gives the extra fifteen species at $p_\mu = \pi/a$ a mass proportional to r/a. Unfortunately, the introduction of the Wilson term leads to $\mathcal{O}(a)$ errors in the fermion action and explicitly breaks chiral symmetry.

Clover improvement [15] describes the process of adding another dimension-five operator,

$$-\frac{i\, g\, a\, C_{SW}\, r}{4} \bar{\psi}\, \sigma_{\mu\nu}\, F_{\mu\nu}\, \psi \,, \tag{1.54}$$

to the fermion action in order to cancel off these $\mathcal{O}(a)$ errors. This gives the Sheikholeslami-Wohlert, or clover fermion action [15],

$$S_{SW} = S_W - \frac{i\, g\, a\, C_{SW}\, r}{4}\; \bar{\psi}(x)\, \sigma_{\mu\nu}\, F_{\mu\nu}\, \psi(x) \;, \tag{1.55}$$

The removal of the $\mathcal{O}(a)$ discretisation errors at tree-level can be observed by performing a Taylor series expansion of the operators. For more details see Refs. [11, 15] or Ref. [16]

[4] An alternate approach that won't be discussed here is the staggered, or Kogut-Susskind fermion action [12]. Two more recent formalisms, the overlap and domain-wall, are more computationally intensive than staggered and Wilson/clover actions, however they preserve chiral symmetry. The overlap will be discussed later. See Refs. [13, 14] for details of the domain-wall approach.

for a good discussion. By properly tuning the clover coefficient C_{SW}, it is possible to remove the $\mathcal{O}(a)$ errors from the fermion action.

At tree level in the non-interacting theory $C_{sw} = 1$. Non-perturbative improvement [17] tunes the clover coefficient to all powers in g^2 by matching to some physical observable. For example, in the Schrödinger functional method, C_{SW} is tuned such that the axial Ward-Takahashi identity is satisfied for a given volume [18]. Unfortunately this approach is susceptible to the problem of exceptional configurations. For small quark masses, the additive mass renormalisation caused by the chiral symmetry breaking of the clover action can give rise to singularities. This can prevent the simulation of light quark masses at finite volumes [19, 20]. Modern simulations [21] use large lattice volumes and small lattice spacings to alleviate this problem, however this is very computationally intensive.

Another approach uses fat, or smeared, links in the construction of the fermion action, leading to the so-called "fat-link" fermion actions [22–26]. These types of actions can overcome the exceptional configuration problem, and reduce the renormalisation of the action improvement coefficients. However, smearing the gauge links will remove gluon interactions at the scale of the cut-off. The effect this has on the quark propagator will be addressed later in Chapter 7. To limit these effects one can consider an action in which only the irrelevant terms of the fermion action are smeared. Giving rise to a fat-link irrelevant clover (FLIC) action [27, 28]. Combined with mean-field improvement, in which all gauge links are replaced by,

$$U_\mu(x) \to \frac{U_\mu(x)}{u_0}\,, \qquad U_\mu^{\mathrm{FL}}(x) \to \frac{U_\mu^{\mathrm{FL}}(x)}{u_0^{\mathrm{FL}}}\,, \tag{1.56}$$

where u_0 (u_0^{FL}) is the mean-link for the original (fat) link, this leads to greatly reduced tadpole contributions and enables tree-level tuning of the clover coefficient, i.e. $C_{SW} = 1$.

Regardless of the approach used, all clover actions still suffer from explicit chiral symmetry breaking. In order to derive a fermion matrix, or Dirac operator, that preserves chiral symmetry and is free doublers on the lattice, it must satisfy the Ginsparg-Wilson relation [29],

$$M\gamma_5 + \gamma_5 M = aMR\gamma_5 M\,, \tag{1.57}$$

where R is a local operator. One solution to the GW relation is provided by the overlap operator [30, 31]. The exact form of the overlap operator and a deeper discussion of the GW relation is provided in later chapters. An alternate solution is the domain-wall formalism [13, 14], which will not be discussed.

1.4.3 Lattice topological charge density

We have discussed how the gauge and fermion fields are transcribed onto the lattice. Let us now consider how the topological charge density can be extracted from a lattice simulation. Unfortunately, the straightforward transcription of Eq. (1.16) onto the lattice suffers from large renormalisations [32, 33], and the geometric transcription of Eq. (1.16) [34, 35] to the lattice is strongly affected by the presence of short distance dislocations in the gauge field [36]. The calculation of the "gluonic" topological charge density therefore requires the application of either a cooling or smearing algorithm.

These algorithms systematically reduce the action of the gauge field by filtering out the UV fluctuations at the scale of the lattice spacing, where discretisation effects are significant, and thereby suppress the large renormalisations that would otherwise be present. A detailed discussion of these algorithms is given in Chapter 2. For now, we will denote the topological charge density extracted in this manner as $q_{sm}(x)$,

$$q_{sm}(x) \equiv \frac{g^2}{16\,\pi^2}\,\mathrm{tr}\,\left(F_{\mu\nu}(x)\tilde{F}_{\mu\nu}(x)\right)\,, \tag{1.58}$$

where $F_{\mu\nu}$ now refers to the lattice field strength tensor calculated after some amount of smearing, and the total topological charge is given by,

$$Q_{sm} = \sum_x q_{sm}(x)\,. \tag{1.59}$$

The presence of short-distance fluctuations in the gauge field means that the total topological charge is typically non-integer valued for small levels of smearing.

An alternate definition of the topological charge density is provided by the massless overlap Dirac operator $D(0,x)$,

$$q_{ov}(x) = -\mathrm{tr}\left[\gamma_5\,\left(1-\frac{a}{2}\,D(0,x)\right)\right]\,. \tag{1.60}$$

As already mentioned, the overlap Dirac operator observes an exact chiral symmetry on the lattice. The benefits of this "fermionic" topological charge density are that it can be calculated on unfiltered gauge fields, and that it exactly satisfies the Atiyah-Singer index theorem [37]. This theorem relates the topological charge to the number of positive, n_+, and negative chirality, n_-, Dirac zeromodes,

$$Q_{ov} = n_- - n_+\,. \tag{1.61}$$

The overlap operator therefore gives exact integer values for the topological charge Q_{ov}.

One problem associated with the gluonic definition of the topological charge density is that the level of applied filtering is arbitrary. There are also no obvious reasons as to why the topological charge density extracted with either the gluonic or fermionic methods should agree. These issues will be addressed in later chapters.

1.5 Example: Lattice determination of $\alpha_s(M_Z)$

The content of this section is based on the publication: K. Maltman, D. Leinweber, P. Moran and A. Sternbeck, Phys. Rev. *D 78, 114504 (2008) [arXiv:0807.2020 [hep-lat]].*

We now present a sample lattice calculation, a determination of the strong coupling constant α_s using Wilson loops. The $n_f = 5$ QCD coupling in the $\overline{MS}$ scheme at the conventionally defined reference scale $\mu = M_Z$ represents one of the fundamental parameters of the Standard Model. Consequently this calculation is included to represent the validity and utility of the lattice approach.

A high precision determination of $\alpha_s(M_Z)$ based on the perturbative analysis of short-distance-sensitive lattice observables computed using the $a \sim 0.09$, 0.12 and 0.18

Table 1.1: Recent non-lattice determinations of $\alpha_s(M_Z)$

Source	$\alpha_s(M_Z)$
Global EW fit [40, 41]	0.1191 ± 0.0027
H1+ZEUS NLO inclusive jets [42, 43]	0.1198 ± 0.0032
H1 high-Q^2 NLO jets [44]	0.1182 ± 0.0045
NNLO LEP event shapes [45]	0.1240 ± 0.0033
NNNLL ALEPH+OPAL thrust distributions [46]	0.1172 ± 0.0022
$\sigma[e^+e^- \to hadrons]$ (2-10.6 GeV) [47]	$0.1190^{+0.0090}_{-0.0110}$
$\frac{\Gamma[\Upsilon(1s)\to\gamma X]}{\Gamma[\Upsilon(1s)\to X]}$ [48]	$0.1190^{+0.0060}_{-0.0050}$
hadronic τ decay [49, 50]	0.1187 ± 0.0016

fm $n_f = 2+1$ MILC[5] data was presented in Ref. [38]. The result, $\alpha_s(M_Z) = 0.1170(12)$, plays a dominant role in fixing the central value of the current Particle Data Group (PDG) assessment [39], $\alpha_s(M_Z) = 0.1176(20)$.

Recently, a number of improved non-lattice determinations of $\alpha_s(M_Z)$ have appeared, in a variety of independent processes, over a wide range of scales [40–50]. The results, given in Table 1.1 (with all errors combined in quadrature), yield a weighted average, $\alpha_s(M_Z) = 0.1190(10)$, $\sim 2\sigma$ higher than the lattice determination. This difference, though not large, motivates revisiting the lattice analysis, especially in light of the existence of new high-scale ($a \sim 0.06$ fm) lattice data not available at the time of the earlier study.

We begin by outlining the original analysis, specifying our own strategy for implementing the underlying approach, and clarifying the difference between our implementation and that of the earlier study and recent HPQCD re-analysis. Following this, we discuss the details of, and input to, our version of the analysis and finally we present and discuss our results.

1.5.1 The original HPQCD/UKQCD analysis

In Ref. [38], $\alpha_s(M_Z)$ was extracted by studying perturbative expansions for a number of UV-sensitive lattice observables, O_k. The generic form of this expansion is

$$O_k = \sum_{N=1} \bar{c}_N^{(k)} \alpha_V(Q_k)^N \equiv D_k \alpha_V(Q_k) \sum_{M=0} c_M^{(k)} \alpha_V(Q_k)^M \tag{1.62}$$

where $Q_k = d_k/a$ are the Brodsky-Lepage-Mackenzie (BLM) scales [51] for the O_k, and $c_0^{(k)} \equiv 1$. The coefficients $\bar{c}_{1,2,3}^{(k)}$ (equivalently, $D_k, c_1^{(k)}$, and $c_2^{(k)}$) have been computed in 3-loop lattice perturbation theory [52], and, with the corresponding d_k, tabulated for a number of O_k in Refs. [38, 52, 53]. In Eq. (1.62), $\alpha_V(\mu)$ is a coupling with the same expansion to $O(\alpha_s^3)$ (with α_s the $\overline{MS}$ coupling) as the heavy quark potential coupling, α_V^p, but differing from it, beginning at $O(\alpha_s^4)$, in a way that will be specified below. The expansion coefficients are known to $O(\alpha_s^4)$, and hence the β function of α_V, defined in our conventions by $\mu^2 da_V(\mu)/d\mu^2 = -\sum_{n=0} \beta_n^V a_V^{n+2}(\mu)$, with $a_V \equiv \alpha_V/\pi$, is determined to

[5]MIMD Lattice Computation (MILC) Collaboration

4 loops by the known coefficients, $\beta_0, \cdots, \beta_3$, of the 4-loop $\overline{MS}$ β function [54, 55]. The coefficients $\bar{c}_1^{(k)}$, $\bar{c}_2^{(k)}$, and $\bar{c}_3^{(k)}$ tabulated in Refs. [38, 52, 53] are valid for expansions of the O_k in terms of any variable, α_T, sharing the same expansion as α_V out to $O(\alpha_s^3)$.

With only the known, third order terms in the expansions of the O_k, no value for the reference scale coupling, $\alpha_V(7.5\text{ GeV}) \equiv \alpha_V^0$, was found to produce a simultaneous fit to the data at all three lattice spacings employed [38]. Consequently, terms out to tenth order in the expansion of Eq. (1.62) were incorporated, the unknown coefficients $\bar{c}_{4,\cdots,10}^{(k)}$ being fitted using input Bayesian prior constraints. The 4-loop version of β^V was used to run α_V^0 to the scales Q_k relevant to each of the given observables at each of the three lattice spacings. Linear extrapolation in the quark masses was employed, and possible residual mass-independent non-perturbative (NP) contributions estimated, and subtracted, using the known leading-order gluon condensate contributions to the relevant Wilson loops [56].

The scales r_1/a and r_1, which determine the lattice spacing, a, in physical units, as well as the gluon condensate, $\langle \alpha_s G^2/\pi \rangle$, required for the mass-independent NP subtraction, were determined as part of the independent fit performed for each of the O_k. This was accomplished using an augmented χ^2 function in which the squared deviations of the relevant parameters from their input central values were scaled by the squares of the input prior widths. For r_1/a and r_1 the central values and widths were provided by the measured values and their uncertainties. For $\langle \alpha_s G^2/\pi \rangle$, a central value 0 and uncertainty ± 0.010 GeV^4 ($\sim$ the conventional SVZ value 0.012 GeV^4 [57]) were employed. While this procedure allows r_1/a and r_1 (which should be characteristic of the lattice under consideration) to take on values which vary slightly with the O_k being analysed, one should bear in mind that the measured uncertainties, which set the range of these variations, are small compared to the variation of scales across the $a \sim 0.09, 0.12$ and 0.18 fm lattices employed in the analysis. The impact of any potential unphysical observable-dependence of the physical scales on the fitted α_V^0 and $\bar{c}_n^{(k)}$ should thus be safely negligible. The situation with regard to the independent fitting of $\langle \alpha_s G^2/\pi \rangle$ for each O_k is potentially more complicated, and will be discussed further below.

The resulting best fit value for α_V^0, averaged over the various observables, was then matched to the $n_f = 3$ $\overline{MS}$ coupling, and the corresponding $n_f = 5$ result, $\alpha_s(M_Z)$, obtained via standard running and matching at the flavor thresholds [58][6], yielding the result, $\alpha_s(M_Z) = 0.1170(12)$, already quoted above.

Regarding the conversion from α_V to α_s, one should bear in mind that, while the expansion for α_V in terms of α_s is, in principle, defined to all orders (see below for more on this point), the coefficients beyond $O(\alpha_s^4)$ involve the currently unknown $\overline{MS}$ β function coefficients $\beta_4, \beta_5, \cdots$. The $n_f = 3$ conversion step is thus subject to a (hopefully small) higher order perturbative uncertainty. As will be explained in Sec. 1.5.3, with the definition of α_V employed in Ref. [38], the higher order perturbative uncertainties are, in fact, entirely isolated in the $V \to \overline{MS}$ conversion step of the analysis.

[6] To be explicit, a self-consistent combination of 2-loop matching and 3-loop running [58] was employed, with the $n_f = 3 \to 4$ and $n_f = 4 \to 5$ flavor thresholds taken to be at $m_c(m_c) = 1.25$ GeV and $m_b(m_b) = 4.25$ GeV, respectively. The use of 2-loop matching and 3-loop running rather than 3-loop matching and 4-loop running is inessential; the resulting value at scale M_Z is lowered by only 0.0002 if one uses the latter approach, a change which is small on the scale of the final quoted error.

1.5.2 An alternate implementation of the HPQCD/UKQCD approach

The higher order perturbative uncertainty encountered in matching α_V to α_s can be removed entirely by working with any expansion parameter, α_T, whose expansion in α_s is fully specified. We take α_T to be defined by the third-order-truncated form of the relation between $\alpha_V^p(\mu^2)$ and $\alpha_s(\mu^2)$ [59] which, for $n_f = 3$, yields

$$\alpha_T(\mu^2) = \alpha_s(\mu^2)\left[1 + 0.5570\alpha_s(\mu^2) + 1.702\alpha_s^2(\mu^2)\right] \ . \tag{1.63}$$

The β function for α_T, β^T, is then determined to 4-loops by the known values of $\beta_0, \cdots, \beta_3$. With all coefficients on the RHS positive, α_T runs much faster than α_s, a fact reflected in the significantly larger values of the non-universal β function coefficients, $\beta_2^T = 33.969$ and $\beta_3^T = -324.393$. This makes running α_T using the 4-loop-truncated β^T function typically unreliable at the BLM scales corresponding to the coarsest ($a \sim 0.18$ fm) lattices considered here. Since, however, the 4-loop-truncated $\overline{MS}$ running of α_s remains reliable down to these scales, and the relation, Eq. (1.63) is, by definition, exact, the running of α_T may be performed by converting from α_T to α_s at the initial scale, running α_s to the final scale, and then converting back to α_T. This procedure will be especially reliable for O_k like $\log(W_{11})$ and $\log(W_{12})$ with lowest BLM scales > 3 GeV.

Though the conversion from the fitted reference scale α_T value to the equivalent $\overline{MS}$ coupling α_s can be accomplished without perturbative uncertainties, higher order perturbative uncertainties do remain in the analysis. To see where, define $\alpha_0 \equiv \alpha_T(Q_0)$, with $Q_0 = Q_k^{max} = d_k/a_{min}$ the maximum of the BLM scales (corresponding to the finest of the lattice spacings, a_{min}) for the observable in question. Expanding the couplings at those BLM scales corresponding to coarser lattices, but the same observable, in the standard manner as a power series in α_0, $\alpha_T(Q_k) = \sum_{N=1} p_N(t_k)\alpha_0^N$ (where $t_k = \log(Q_k^2/Q_0^2)$, and the $p_N(t)$ are polynomials in t), one finds, on substitution into Eq. (1.62),

$$\begin{aligned}\frac{O_k}{D_k} = \cdots &+ \alpha_0^4\left(c_3^{(k)} + \cdots\right) + \alpha_0^5\left(c_4^{(k)} - 2.87c_3^{(k)}t_k + \cdots\right) + \alpha_0^6\left(c_5^{(k)} - 0.0033\beta_4^T t_k\right. \\ &-3.58c_4^{(k)}t_k + [5.13t_k^2 - 1.62t_k]c_3^{(k)} + \cdots\Big) + \alpha_0^7\left(c_6^{(k)} - 0.0010\beta_5^T t_k\right. \\ &+[0.0094t_k^2 - 0.0065c_1^{(k)}t_k]\beta_4^T - 4.30c_5^{(k)}t_k + [7.69t_k^2 - 2.03t_k]c_4^{(k)} \\ &+[-7.35t_k^3 + 6.39t_k^2 - 4.38t_k]c_3^{(k)} + \cdots\Big) + \cdots \ .\end{aligned} \tag{1.64}$$

where the known numerical values of $\beta_0^T, \cdots, \beta_3^T$ have been employed, and we display only terms involving one or more of the unknown quantities $\beta_4^T, \beta_5^T, \cdots, c_3^{(k)}, c_4^{(k)}, \cdots$.

Running the $\overline{MS}$ coupling numerically using the 4-loop-truncated β function is equivalent to keeping terms involving $\beta_0, \cdots, \beta_3$ to all orders, and setting $\beta_4 = \beta_5 = \cdots = 0$. Neglecting $\beta_4, \beta_5 \cdots$ means that $\beta_4^T, \beta_5^T, \cdots$ also do not take on their correct physical values, leading to an alteration of the true t_k-dependence, beginning at $O(\alpha_0^6)$. Since it is the scale-dependence of O_k which is used to fit the unknown coefficients $c_{3,4,\ldots}^{(k)}$, as well as α_0, we see immediately that the 4-loop truncation necessarily forces compensating

changes in at least the coefficients $c^{(k)}_{4,5,\cdots}$. A shift in $c^{(k)}_4$, however, also alters the $O(\alpha_0^5)$ coefficient, which will, in general, necessitate an approximate compensating shift in $c^{(k)}_3$ as well, and, in consequence, a further compensating shift in α_0. From Eq. (1.64), the size of such effects, associated with the truncation of the running, and unavoidable at some level, can be minimised by taking Q_0 as large as possible (achieved by working with the observable with the highest intrinsic BLM scale) and keeping t_k from becoming too large (achieved by restricting one's attention, if possible, to a subset of finer lattices)[7].

1.5.3 More on the relation between the two implementations

For $n_f = 3$, in our notation, the relation between α^p_V and α_s, to $O(\alpha_s^3)$, is [59]

$$\alpha^p_V(q^2) = \alpha_s(\mu^2)\left[1 + \kappa_1(\mu^2/q^2)\alpha_s(\mu^2) + \kappa_2(\mu^2/q^2)\alpha_s(\mu^2)\right] \tag{1.65}$$

where $\kappa_2(x) = \left[a_2 + 16\beta_0^2\log^2(x) + (16\beta_1 + 8\beta_0 a_1)\log(x)\right]/16\pi^2$, with $a_2 = \frac{695}{6} + 36\pi^2 - \frac{9}{4}\pi^4 + 14\zeta(3)$, and $\kappa_1(x) = \left[7 + 4\beta_0\log(x)\right]/4\pi$. Our expansion parameter, $\alpha_T(q^2)$ is defined to be equal to the RHS of Eq. (1.65) with $\mu^2 = q^2$, leading to the numerical result given in Eq. (1.63). The conversion from α_T to α_s can be performed exactly but the absence in $\beta^T_{4,5,\cdots}$ of terms $\propto \beta_{4,5,\cdots}$ induces a perturbative uncertainty in the values of our fitted parameters, one which can, however, be reduced by working with high scale observables and fine lattices. It is also possible to test for its presence by expanding the fits to include coarser lattices, where the effects of the omitted contributions will be larger.

The construction of the expansion parameter α_V is somewhat more complicated, but turns out to be equivalent to the following. One first takes the RHS of Eq. (1.65), with $\mu^2 = e^{-5/3}q^2$, to define an intermediate coupling, $\alpha'_V(q^2)$. The corresponding β function, β', is then determined to 4-loops by $\beta_0, \cdots, \beta_3$. The higher order coefficients, $\beta'_{4,5,\cdots}$, however, depend on the presently unknown $\beta_{4,5,\cdots}$, are hence are themselves unknown. The final HPQCD coupling, α_V, is obtained from α'_V by adding terms of $O(\alpha_s^5)$ and higher with coefficients chosen to make $\beta^V_4 = \beta^V_5 = \cdots = 0$. Since $\beta_{4,5,\cdots}$ are not known, the values of the coefficients needed to implement these constraints are also not known. The coupling is nonetheless, in principle, well-defined, with higher order coefficients computable as soon as the corresponding higher order β_k become available. Since the 4-loop-truncated β^V function is, by definition, exact, the distortions of the fit parameters induced, in general, by the 4-loop truncation of the running are absent for the α_V coupling. The price to be paid for this advantage is the unknown perturbative

[7]The non-universal $\beta^T_{n>1}$ receive contributions from all of the $\overline{MS}$ coefficients β_m with $m \le n$. Numerically, one has $\beta^T_2 = \beta_2 + 23.9090 = 33.9689$, $\beta^T_3 = \beta_3 - 371.6215 = -324.3934$, $\beta^T_4 = \beta_4 - 758.1717$, $\beta^T_5 = \beta_5 - 7\beta_4 + 30807.8757$, $\cdots$, where the additive numerical terms reflect the known contributions of the lower order β_k. Since terms involving $\beta_0, \cdots, \beta_3$ are kept to all orders in our analysis, only the parts of $\beta^T_4, \beta^T_5, \cdots$ proportional to $\beta_4, \beta_5, \cdots$ are not properly included. The expressions for $\beta^T_{2,3}$, show that the lower order terms in fact dominate in those cases. The expressions for $\beta^T_{4,5}$ will also be dominated by the already-fully-included lower order contributions unless an extremely rapid growth with order occurs for the $\overline{MS}$ β function coefficients. The distortion of the t_k-dependence discussed in the text should thus, in fact, be considerably weaker than it might appear from the original form of the argument. It nonetheless remains sensible to treat with greater confidence analyses which are based on high scale observables and employ the finest lattices.

uncertainty in the relation between α_V and α_s, which affects the conversion and running to $\alpha_s(M_Z)$. With this definition, α_V differs from α_T beginning at $O(\alpha_s^4)$.

The other difference between the two re-analyses lies in the treatment of r_1/a, r_1, and $\langle\alpha_s G^2/\pi\rangle$. In Ref. [38], these are allowed to vary independently, though within the range of the input prior constraints, for each O_k, whereas in our analysis, they are treated as fixed external input, and have the same central values for all O_k. As noted above, the difference in the treatment of r_1/a and r_1 is expected to have a negligible impact. The impact of the differing treatments of $\langle\alpha_s G^2/\pi\rangle$ should be similarly negligible for observables with intrinsic scales high enough that the associated correction is small.

The two different implementations of the original HPQCD/UKQCD approach will thus, when restricted to high-scale observables, correspond to isolating residual higher order perturbative uncertainties in different sectors of the analysis. If these uncertainties are, as desired, small in both cases, the two analyses should be in good agreement. Such agreement (which is, in fact, observed, provided comparison is made to the very recent HPQCD update) serves to increase confidence in the results of both analyses.

1.5.4 Details of our re-analysis

In our analysis, we have calculated the desired Wilson loops using the publicly available $a \sim 0.09$, 0.12, 0.15 and 0.18 fm MILC $n_f = 2 + 1$ ensembles and incorporated information on W_{11} and W_{12} for the three $a \sim 0.06$ fm USQCD ensembles provided to us by Doug Toussaint of the collaboration.

We follow the basic strategy of the earlier analysis, using the same 3-loop perturbative input, but with the following differences in implementation. First, we employ the expansion parameter α_T throughout. All running of α_T is carried out using exact 4-loop-truncated running of the intermediate variable, α_s, whose relation to α_T is given by Eq. (1.63). Second, to minimise the effect of our incomplete knowledge of the running of α_T beyond 4-loop order, the impact of which will be larger for coarser lattices, we perform "central" 3-fold versions of our fits using the three finest lattices, with $a \sim 0.12$, 0.09 and 0.06 fm. Expanded 5-fold fits then serve as a way of studying the impact of the truncated running, as well as of the truncation of the perturbative expansion for the O_k. Since we do not currently have access to the actual $a \sim 0.06$ fm configurations, we are restricted to analysing the three observables indicated above. One of these, $\log(W_{12}/u_0^6)$, has a significantly lower BLM scale, and hence is particularly useful for studying the impact of these truncations. As in Ref. [38], we extrapolate linearly in the quark masses[8], and estimate (and subtract) residual mass-independent NP effects using the known form of the leading order gluon condensate contributions to the relevant Wilson loops.

Regarding the mass extrapolation, the sets of configurations for different mass combinations am_ℓ/am_s corresponding to approximately the same lattice spacing a in fact have

[8]We have performed a number of supplementary studies of the mass extrapolation, restricting our attention to subsets of the data for different am_ℓ/am_s but common a and allowing also a quadratic component in the fit function. The zero-mass-extrapolated values are very stable to such variations. Moreover, not only are the quadratic coefficients returned by the extended optimised fits very small, but a χ^2/dof significantly less than 1 is already produced by the linear fits alone. We conclude that the quark masses of the ensembles employed are already sufficiently small that the mass-dependent NP contributions can be reliably removed by a linear extrapolation.

slightly different measured r_1/a. Since the O_k we study are themselves scale-dependent, full consistency requires converting the results corresponding to the different am_ℓ/am_s to a common scale before extrapolation. This could be done with high accuracy if the parameters appearing in the perturbative expansion of the O_k were already known. Since, however, some of these parameters are to be determined as part of the fit, the extrapolation and fitting procedure must be iterated. With sensible starting points, convergence is achieved in a few iterations. The dominant uncertainty in the converged iterated extrapolated values is that associated with the uncertainties in r_1/a. There is also a 100%-correlated global scale uncertainty associated with that on r_1. We employ $r_1 = 0.318(7)$ fm, as given in the MILC Lattice 2007 pseudoscalar project update [60].

The mass-independent NP subtractions are estimated using the leading order (LO) $D = 4$ gluon condensate contribution, $\delta_g W_{mn}$, to the $m \times n$ Wilson loop, W_{mn} [56]

$$\delta_g W_{mn} \;=\; \frac{-\pi^2}{36} m^2 n^2 a^4 \langle \alpha_s G^2/\pi \rangle \tag{1.66}$$

and the central value, $\langle \alpha_s G^2/\pi \rangle \;=\; (0.009 \pm 0.007)$ GeV^4, of the updated charmonium sum rule analysis [61, 62]. Since the error here is already close to 100%, we take the difference between results obtained with and without the related subtraction as a measure of the associated uncertainty. This should be sufficiently conservative if the correction is small. If not, the measured O_k values may contain additional non-negligible mass-independent contributions, of dimension $D > 4$, which we do not know how to estimate and subtract. O_k for which this occurs will thus provide a less reliable determination of α_s.

Fortunately, for the observables we consider, the gluon condensate correction is, as desired, small. For $O_k = \log(W_{11})$, the corrections required for the 3-fold (5-fold) fit do not exceed $\sim 0.1\%$ ($\sim 0.5\%$). The corrections remain small (less than $\sim 0.4\%$ ($\sim 1.8\%$)) for $O_k = \log(W_{12})$. The effect is somewhat larger for $\log(W_{12}/u_0^6)$, as a consequence of cancellations encountered in combining the uncorrected $\log(W_{11})$ and $\log(W_{12})$ values, but still reaches only $\sim 1.3\%$ ($\sim 5.6\%$) for the 3-fold (5-fold) fit[9].

In line with what was seen in Ref. [38], we find that the known terms in the perturbative expansions of the O_k are insufficient to provide a description of the observed scale-dependence, even when only the three finest lattices are considered. When $c_3^{(k)}$ is added to the fit, however, we find very good fits, with $\chi^2/dof < 1$ (very significantly so for the 3-fold fits). With current errors, it is thus not possible to sensibly fit additional coefficients $c_{m>3}^{(k)}$. This raises concerns about possible truncation uncertainties. Comparison of the results of the 3-fold and 5-fold fits provides one handle on such an uncertainty since the relative weight of higher order to lower order terms grows with decreasing scale. If neglected higher order terms are in fact *not* negligible, the growth

[9]The relative size of the gluon condensate correction grows rapidly with loop dimension. For the 2×3 loop, for example, the correction to $O_k = \log(W_{23})$, would reach $\sim 8\%$ for the 3-fold fit, and $\sim 31\%$ for the coarsest of the lattices entering the 5-fold fit (where the "correction", $\delta_g W_{23}$, has, in fact, grown to a factor of ~ 2 larger in size than the measured W_{23} itself). A further enhancement, similar to that encountered for $\log(W_{12}/u_0^6)$, occurs when O_k is the logarithm of one of the Creutz ratios or tadpole-improved ratios. For example, the size of the "corrections" for $O_k = \log(W_{23}/u_0^{10})$, $\log(W_{11}W_{23}/W_{12}W_{13})$ and $\log(W_{14}/W_{23})$, which represent the three extreme "outliers" of the original HPQCD/UKQCD analysis, are 56%, 82% and 101%, respectively.

Table 1.2: Central fit results for $\alpha_s(M_Z)$ and the $c_3^{(k)}$

O_k	$\alpha_s(M_Z)$	$c_3^{(k)}$
$\log(W_{11})$	0.1192 ± 0.0011	-3.8 ± 0.6
$\log(W_{12})$	0.1193 ± 0.0011	-4.0 ± 0.9
$\log(W_{12}/u_0^6)$	0.1193 ± 0.0011	-1.7 ± 0.8

with decreasing scale of the resulting fractional error should show up as an instability in the values of the parameters extracted using the different fits. We see no signs for such an instability within the errors of our fits, but nonetheless include the difference of central values obtained from the 3-fold and 5-fold fits as a component of our error estimate.

1.5.5 Results

Central inputs for our fits are the measured lattice observables (whose errors are tiny on the scale of the other uncertainties), the computed D_k, $c_1^{(k)}$ and $c_2^{(k)}$ [38, 52], r_1/a, r_1 and $\langle \alpha_s G^2/\pi \rangle$, and the choice of the 3-fold fitting procedure. In addition to the uncertainties generated by the errors on r_1/a, r_1 and $\langle \alpha_s G^2/\pi \rangle$, are those due to uncertainties in numerical evaluations of the D_k, $c_1^{(k)}$ and $c_2^{(k)}$.

We construct an "overall scale uncertainty error" by adding *linearly* the fit uncertainties generated by those on r_1 and the r_1/a. This combined error is added in quadrature to (1) uncertainties produced by varying the $c_2^{(k)}$ (and, if relevant, $c_1^{(k)}$) within their errors, (2) the difference between results obtained with and without the gluon condensate correction, and (3) the difference between the results of the 3-fold and 5-fold fits. Because of the iterative nature of the fit procedure, the mass extrapolation uncertainty is incorporated into what we have here identified as the overall scale uncertainty.

We run our $n_f = 3$ results to M_Z using the self-consistent combination of 4-loop running and 3-loop matching at the flavor thresholds, taking the flavor thresholds to lie at $rm_c(m_c)$ and $rm_b(m_b)$, with $m_c(m_c) = 1.286(13)$ GeV and $m_b(m_b) = 4.164(25)$ GeV [63], and r allowed to vary between 1 and 3. These uncertainties in the matching thresholds, together with standard estimates for the impact of the truncated running and matching, produce an evolution contribution to the uncertainty on $\alpha_s(M_Z)$ of ± 0.0003 [40].

Our central fit results for $\alpha_s(M_Z)$ and the $c_3^{(k)}$ are given in Table 1.2. For comparison, the results for $\alpha_s(M_Z)$ obtained in Ref. [38] were 0.1171(12), 0.1170(12) and 0.1162(12), for $\log(W_{11})$, $\log(W_{12})$ and $\log(W_{12}/u_0^6)$, respectively. Our $\alpha_s(M_Z)$ are significantly larger, and in closer mutual agreement. The recent HPQCD update [53] also finds significantly larger values. The very good agreement between the $\alpha_s(M_Z)$ values obtained in our fits using both low- and high-scale observables suggests that the effects of the truncated running, present at some level in all such fits, are small in the cases we have studied.

One-sided versions of the various components of the total errors on $\alpha_s(M_Z)$ are displayed in Figure 1.4. The difference of the 3-fold and 5-fold determinations is ~ 0.0004, significantly smaller than the ~ 0.0009 overall scale uncertainty. The results

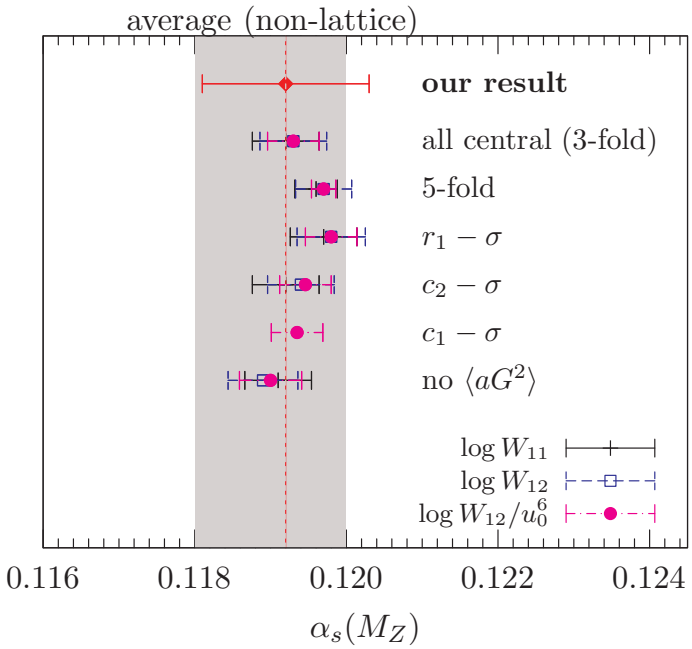

Figure 1.4: Contributions to the errors on $\alpha_s(M_Z)$. Shown are the $\alpha_s(M_Z)$ obtained using (i) the 3-fold fit strategy, with all central input, (ii) the alternate 5-fold fit strategy, with all central input, and (iii) the 3-fold fit strategy, with, one at a time, each input shifted from its central value by 1σ, retaining central values for the remaining input parameters. The error bars shown are those associated with the uncertainties in r_1/a.

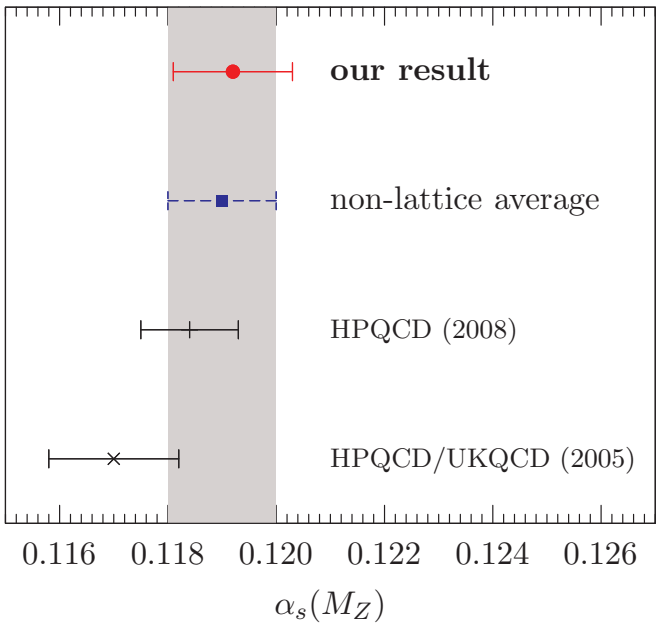

Figure 1.5: Comparison of the results for $\alpha_s(M_Z)$ from our fits, the fits of Ref. [38] and the updated fits of Ref. [53] with the average of recent non-lattice determinations.

thus show no evidence for any instability associated with opening up the fit to lower scales.

While the total error on $\alpha_s(M_Z)$ is the same for all three O_k considered, the general arguments above lead us to believe that the most reliable determination is that obtained using the highest-scale observable, $\log(W_{11})$, and highest-scale (3-fold fit) analysis window. Our final assessment,

$$\alpha_s(M_Z) = 0.1192 \pm 0.0011 \ , \tag{1.67}$$

is in excellent agreement with the non-lattice average and the result, 0.1184 ± 0.0009, of the independent HPQCD analysis. The various results are shown for comparison in Figure 1.5.

1.6 Outline

The aim of the work presented in the following chapters is to perform multiple in depth studies of QCD vacuum structure within the context of Lattice QCD. As such, a large portion of the thesis is devoted to the analysis of the algorithms used to analyse the topological structure of the vacuum. In arranging this thesis, the intention was that each chapter be essentially independent of the remaining chapters. It should therefore be possible to read any chapter with only minor references to the preceding chapters. Perhaps the only exception to this rule is the following chapter on over-improved stout-link smearing as this algorithm is used extensively throughout the remainder of the thesis. The overall structure of the thesis is as follows:

We begin with an introduction to cooling and smearing algorithms on the lattice in Chapter 2. Following this, we define our own algorithm, a topologically stable, over-improved stout-link smearing algorithm. We perform an analysis of the new algorithm against standard stout-link smearing. The results of this chapter demonstrate the importance of using improved smearing algorithms for topological studies of the QCD vacuum.

Chapter 3 performs a comparison of the topological charge density, extracted with this new smearing algorithm, against the topological charge density from the overlap operator. The results reveal a good correlation between the important structures in the QCD vacuum, from both algorithms. This provides further support for the use of over-improved smearing in vacuum studies.

In Chapter 4 a similar comparison is performed, however this time it is the overlap operator that is examined. Specifically, we examine the extent to which the topological charge density from the overlap operator depends on the input (negative) Wilson-mass parameter. In this formulation, the Wilson-mass is used in the negative mass region and acts as a regulator governing the scale at which the Dirac operator is sensitive to topological aspects of the gauge field. A clear dependence is observed, and the results are calibrated against over-improved stout-link smearing.

With the analysis of the smearing algorithm and overlap operator complete, in Chapter 5 we proceed to analyse the structure of the QCD vacuum. Of interest, are the contrasting pictures of the vacuum that are revealed at different energy scales. Perhaps

more importantly, this chapter also presents a study of the impact of dynamical sea quarks on the QCD vacuum.

The further usefulness of smearing algorithms is then demonstrated in Chapter 6. Here we show how smearing can be used as a preconditioner for Maximal Centre Gauge fixing algorithms. This is achieved through an analysis of centre vortices in the $SU(3)$ gauge theory, and the results demonstrate the effectiveness of smearing as a preconditioner.

Chapter 7 assesses the impact of smearing on the overlap quark propagator. This is important since the work of the preceding chapters has been primarily focused on the QCD vacuum. Here we examine the connection between vacuum structure and the manner in which quarks propagate in the vacuum. The overlap quark propagator is chosen because of its excellent chiral properties. The results indicate that dynamical mass generation in the quark propagator is compromised after smearing. This raises concerns on the use of smearing in all links of a fermion action.

The analysis of the dynamical vacuum is continued in Chapter 8 with a calculation of the proton and Δ^+ charge radii and magnetic moments using dynamical gauge fields. This study of the electromagnetic properties of baryons allows us to investigate the non-perturbative effects of the dynamical QCD vacuum on physical particles. We demonstrate how the absence of dynamical sea-quark loops in previous quenched calculations leads to a negative chiral curvature in the μ_{Δ^+}/μ_p magnetic moment ratio. We show how this negative chiral curvature is suppressed in full QCD and discuss the reasons for this behaviour.

Finally, Chapter 9 presents a discussion and draws conclusions from the work contained herein.

Chapter 2

Over-improved stout-link smearing and the QCD vacuum

The content of this chapter is based on the publication: P. J. Moran and D. B. Leinweber, Phys. Rev. *D 77, 094501 (2008) [arXiv:0801.1165 [hep-lat]].*

In this chapter we present an introduction to cooling and smearing algorithms on the lattice. A new over-improved stout-link smearing algorithm, designed to stabilise instanton-like objects, is then presented. A method for quantifying the selection of the over-improvement parameter, ϵ, is demonstrated. The new smearing algorithm is compared with the original stout-link smearing, and Symanzik improved smearing through calculations of the topological charge and visualisations of the topological charge density. We find the incorporation of improvement in stout-link smearing to be essential for the accurate study of QCD vacuum structure.

2.1 Introduction

Studies of long distance physics in Lattice QCD simulations often require the suppression of short-range UV fluctuations. This is normally achieved through the application of a smoothing algorithm. The most common prescriptions are cooling [64–66], APE [67, 68], and improved APE smearing [69], HYP smearing [70] and more recently, EXP or stout-link smearing [71] and LOG smearing [72]. Filtering methods such as these are also regularly used in calculations of physical observables to improve overlap with low energy states.

All smoothing methods are based on an approximation to the continuum gluonic action

$$S_g = \frac{1}{2}\int d^4x \ \mathrm{tr}\left(F_{\mu\nu}F_{\mu\nu}\right) \ . \tag{2.1}$$

Because space-time is approximated by a 4-D lattice, these approximations contain unavoidable discretisation errors. These errors can have a negative effect on the topological objects present in the gauge field being studied and are detrimental to the smoothing process.

There are two noteworthy approaches for dealing with these discretisation errors and both have so far been restricted to cooling algorithms. One approach is to eliminate he

discretisation errors through a strategic combination of larger Wilson loops [11, 69, 73, 74] leading to the so-called 3-, 4-, and 5-loop $\mathcal{O}(a^4)$-improved actions. These actions are used in the cooling algorithm to identify the individual link that will maximally reduce the local action. The difficulty with this approach is that relatively long link paths are combined with the plaquette in improving the action. The preferred 3- and 5-loop improved actions include the 3×3 Wilson loop which involves 8 links more than the plaquette. Early in the application of cooling, it is essential to accommodate for the large renormalisations of the improvement coefficients and the best practice [74] is to consider tadpole-improvement via the mean link, u_0. However, early in the cooling procedure, a mean-field estimate of $1/u_0^8$ for the coefficient renormalisation is not accurate and the utility of highly-improved actions on rough configurations is of concern.

Ideally one seeks a solution involving only the most local link paths, the plaquette and the rectangle. Unfortunately, as shown by Perez, *et al.* [75] and briefly reiterated below, the $\mathcal{O}(a^4)$ errors remaining after the removal of the $\mathcal{O}(a^2)$ errors act to spoil instanton-like objects in the field. They proposed the second noteworthy approach of over-improved cooling as a means of taming these errors via the introduction of a new tunable parameter ϵ into their action [75]. They selected the combination of 1×1 and 2×2 link paths, exacerbating problems associated with the renormalisation of the coefficients.

Thus there is a need to investigate the utility of over-improvement in the maximally local case of 1×1 and 1×2 link paths. Here the standard tactics of tadpole improvement will be the most effective. To the best of our knowledge this is the first derivation of the over-improved 1×1 plus 1×2 action and as such, the first investigation of its utility in both classical instanton configurations and in preserving topological structure in lattice Monte-Carlo generated configurations.

We also note that there has been remarkably little, if any, focus on the role of improvement and over-improvement in the context of smearing algorithms. As such the work presented here leads an important new area of study and presents the first application of (over-)improvement in the popular stout-link smearing algorithm.

Smearing is preferred to cooling for several reasons. Unlike cooling, smearing provides a well defined and differentiable lattice action suitable for use in dynamical-fermion simulations. Moreover, the presence of a smearing parameter enables greater control over the amount of smoothing performed in the important early stages of the smoothing process.

In Sec. 2.2 we begin by presenting a brief summary of the most common smoothing algorithms and illustrate the role of the lattice action in both cooling and smearing. We then describe the creation of a new over-improved stout-link smearing algorithm based on 1×1 plus 1×2 paths in Sec. 2.3. Here, the lattice discretisation errors of a single classical instanton are considered. As emphasised above, this is the first exploration of over-improvement utilising the maximally local 1×1 and 1×2 link paths.

In Sec. 2.4 we present the first quantitative method for tuning the over-improvement parameter, ϵ. This is essential for ensuring topological objects larger than the dislocation threshold are not distorted under continued smearing. Whereas the previous study [75] simply selected the value of -1, we have discovered this choice is less than optimal.

Finally, in Sec. 2.5 we demonstrate the utility of the over-improved stout-link smear-

ing algorithm on a variety of lattices, including large $28^3 \times 96$ light dynamical gauge fields from the MILC collaboration [76, 77]. Of particular note is our illustration of the destruction of topologically nontrivial objects in real gauge field configurations under standard stout-link smearing and the preservation of these objects under over-improved stout-link smearing. To the best of our knowledge, this is the first time such a comparison has been illustrated using any (over-)improved smoothing algorithm.

2.2 Smoothing algorithms

Standard cooling proceeds via a systematic sequential update of all links $U_\mu(x)$ on the lattice, where at each link update the local Wilson action [1] is minimised. The local Wilson action corresponding to $U_\mu(x)$ is defined as

$$S_W(x) = \beta \sum_{\substack{\nu \\ \nu \neq \mu}} \frac{1}{3} \mathrm{Re}\,\mathrm{tr}\,(1 - U_\mu(x)\Sigma_{\mu\nu}(x)) \;, \tag{2.2}$$

where

$$\Sigma_{\mu\nu}(x) = U_\nu(x+\hat{\mu})\,U_\mu^\dagger(x+\hat{\nu})\,U_\nu^\dagger(x) + U_\nu^\dagger(x+\hat{\mu}-\hat{\nu})\,U_\mu^\dagger(x-\hat{\nu})\,U_\nu(x-\hat{\nu}) \tag{2.3}$$

is the sum of the two staples touching $U_\mu(x)$ which reside in the μ-ν plane. From (2.2), we can see that S_W will be minimised when $\mathrm{Re}\,\mathrm{tr}\,(1 - U_\mu(x)\Sigma_{\mu\nu}(x)) = 0$. It naturally follows that when cooling, the aim is to replace $U_\mu(x)$ with a new link that optimises

$$\max \mathrm{Re}\,\mathrm{tr} \left(U_\mu(x) \sum_{\substack{\nu \\ \nu \neq \mu}} \Sigma_{\mu\nu}(x) \right) . \tag{2.4}$$

When performing this update in parallel, one must be careful not to replace any link which is included in the local action of a neighbouring link. This requirement means that cooling is a relatively slow operation computationally, but fast in regard to the removal of action from the gauge field.

APE smearing differs from standard cooling in that all links can be simultaneously updated in a single sweep through the lattice, resulting in a significant speed increase. In APE smearing one first calculates a smeared link $U'_\mu(x)$, which is the weighted sum of its nearest neighbours,

$$U'_\mu(x) = (1-\alpha)\,U_\mu(x) + \frac{\alpha}{6} \sum_{\substack{\nu \\ \nu \neq \mu}} \Sigma^\dagger_{\mu\nu}(x) \,, \tag{2.5}$$

where $\Sigma_{\mu\nu}$ is defined as in (2.3), and α is a real parameter, usually set to ≈ 0.7. The new link $U'_\mu(x)$ is then projected back into the $SU(3)$ group via some projection operator $\mathcal{P}$,

$$\tilde{U}_\mu(x) = \mathcal{P}\,U'_\mu(x) \,. \tag{2.6}$$

The projection of (2.6) is necessary because we have performed an additive step in (2.5), which is not an $SU(3)$ group operation. The projection step is not uniquely defined, but the preferred method is to select the new smeared link $U_\mu(x)$ such that it maximises

$$\mathrm{Re}\,\mathrm{tr}\left(U_\mu(x)\,U'^{\dagger}_\mu(x)\right)\,. \tag{2.7}$$

In the limit $\alpha \to 1$ we see that (2.5) becomes

$$U'_\mu(x) \to \frac{1}{6}\sum_{\substack{\nu \\ \nu\neq\mu}} \Sigma^{\dagger}_{\mu\nu}(x)\,. \tag{2.8}$$

Substituting this result into (2.7) shows how the projection method has become equivalent to cooling (2.4), and that there exists a direct link between APE smearing and cooling in the limit that links are updated sequentially. The simultaneous update of APE smearing limits $\alpha < 0.75$ [78].

The more recent smearing technique, stout-link smearing [71], makes use of the exponential function to remain within the gauge group and remove the need for a projection step. Beginning with the staples (2.3), define

$$C_\mu(x) = \sum_{\substack{\nu \\ \nu\neq\mu}} \rho_{\mu\nu}\Sigma^{\dagger}_{\mu\nu}(x)\,, \tag{2.9}$$

where we will choose an isotropic four-dimensional constant $\rho_{\mu\nu} = \rho_{\mathrm{sm}}$, but other selections are possible. The matrix $Q_\mu(x)$ defined by

$$Q_\mu(x) = \frac{i}{2}(\Omega^{\dagger}_\mu(x) - \Omega_\mu(x)) - \frac{i}{6}\mathrm{tr}(\Omega^{\dagger}_\mu(x) - \Omega_\mu(x))\,, \tag{2.10}$$

with

$$\Omega_\mu(x) = C_\mu(x)\,U^{\dagger}_\mu(x)\,, \tag{2.11}$$

is by definition Hermitian and traceless, and hence $e^{iQ_\mu(x)} \in SU(3)$. The new smeared link is then defined by

$$\tilde{U}_\mu(x) = \exp(iQ_\mu(x))\,U_\mu(x)\,. \tag{2.12}$$

An expansion of the exponential in (2.12) results in the same sum of paths, to first order in ρ_{sm}, as for APE smearing [71]. Given this, and the already established link between APE smearing and cooling, it follows that there exists a connection between cooling and stout-link smearing. Indeed, simulations of Lattice QCD show that for any given gauge field, the structures revealed by the smoothing procedures are remarkably similar.

2.3 Discretisation errors and improvement

The corrosion of topological structures during the smoothing process is a well known side-effect of both cooling and smearing [69, 73, 74]. It is the unavoidable discretisation errors in the lattice action that are the cause of this observed behaviour. This obviously

inhibits our ability to study topological excitations on the lattice with the most local operators and it would be beneficial if it could be prevented.

When a gauge field is smoothed, the topological structures within are subjected to the effects of lattice discretisation errors. One such topological excitation is the instanton. To understand how the errors will alter instanton distributions, first consider the clover Wilson action given by

$$S_W = \beta \sum_x \sum_{\mu>\nu} (1 - P_{\mu\nu}(x)) \ , \tag{2.13}$$

where $P_{\mu\nu}(x)$ denotes 1/3 of the real trace of the clover average of the four plaquettes touching the point x.

Following Ref. [75], S_W can be expanded in powers of the lattice spacing, a, giving:

$$\begin{aligned} S_W = a^4 \sum_x \sum_{\mu>\nu} \mathrm{tr} \Bigg(& \frac{1}{2} F_{\mu\nu}^2(x) - \frac{a^2}{24} \left((\mathcal{D}_\mu F_{\mu\nu}(x))^2 + (\mathcal{D}_\nu F_{\mu\nu}(x))^2 \right) \\ & - \frac{a^4}{24} \Bigg(g^2 F_{\mu\nu}^4(x) - \frac{1}{30} \left((\mathcal{D}_\mu^2 F_{\mu\nu}(x))^2 + (\mathcal{D}_\nu^2 F_{\mu\nu}(x))^2 \right) \\ & - \frac{1}{3} \mathcal{D}_\mu^2 F_{\mu\nu}(x) \mathcal{D}_\nu^2 F_{\mu\nu}(x) + \frac{1}{4} (\mathcal{D}_\mu \mathcal{D}_\nu F_{\mu\nu}(x))^2 \Bigg) \Bigg) + O(a^{10}, g^4) \, , \end{aligned} \tag{2.14}$$

where $igF_{\mu\nu} = [D_\mu, D_\nu]$, $D_\mu = \partial_\mu + igA_\mu$, and $\mathcal{D}_\mu \phi = \ [D_\mu, \phi]$, for arbitrary ϕ.

The goal is to substitute the instanton solution [8] given by

$$A_\mu(x) = \frac{x^2}{x^2 + \rho_{\mathrm{inst}}^2} \left(\frac{i}{g} \right) \partial_\mu(S) \, S^{-1} \, , \tag{2.15}$$

where

$$S \equiv \frac{x_4 \pm i \, \vec{x} \cdot \vec{\sigma}}{\sqrt{x^2}} \, , \tag{2.16}$$

for instantons/anti-instantons with σ the Pauli matrices, into the expanded Wilson action (2.14). This requires the use of the lattice approximation $a^4 \sum_x \approx \int d^4x$. Substituting the instanton solution (2.15) into Eq. (2.14) and performing the integration then yields,

$$S_W^{\mathrm{inst}} = \frac{8\pi^2}{g^2} \left[1 - \frac{1}{5} \left(\frac{a}{\rho_{\mathrm{inst}}} \right)^2 - \frac{1}{70} \left(\frac{a}{\rho_{\mathrm{inst}}} \right)^4 \right] . \tag{2.17}$$

Notice that the leading error term in (2.17) is negative and depends upon the instanton size ρ_{inst}. When the Wilson action is used in a smoothing algorithm these errors cause the action density to be under-estimated. Additionally, by decreasing ρ_{inst} the action will be further reduced. The smoothing algorithms, which are trying to decrease the action, will therefore shrink ρ_{inst} in order to reduce the action. Repeated application of the smoothing procedures will eventually lead to overwhelming discretisation errors and cause instantons to "fall through the lattice" and disappear.

Improved actions aim to fix the problem of discretisation errors by including different sized Wilson loops in the calculation of the action. By choosing the coefficients of the loop combinations carefully it is possible to eliminate the leading order error terms.

The Symanzik improved action uses a linear combination of plaquette and rectangular loops to eliminate the $\mathcal{O}(a^2)$ errors.

$$S_S = \beta \sum_x \sum_{\mu>\nu} \left[\frac{5}{3}(1 - P_{\mu\nu}(x)) - \frac{1}{12}\big((1 - R_{\mu\nu}(x)) + (1 - R_{\nu\mu}(x))\big) \right]. \tag{2.18}$$

Analogous to $P_{\mu\nu}$, $R_{\mu\nu}$ and $R_{\nu\mu}$ denote the different possible orientations of the rectangular loops.

This can be expanded in terms of a, and the instanton solution substituted as above to find, in agreement with [75], that

$$S_S^{\text{inst}} = \frac{8\pi^2}{g^2} \left[1 - \frac{17}{210} \left(\frac{a}{\rho_{\text{inst}}} \right)^4 \right]. \tag{2.19}$$

The $\mathcal{O}(a^2)$ error term has been removed by design, but we see that the $\mathcal{O}(a^4)$ term is still negative. Therefore, this action will still not preserve instantons.

2.4 Over-Improvement

2.4.1 Formalism

In 1993, Perez, *et al.* [75] introduced the notion of over-improved cooling, also known as ϵ-cooling. The essential idea was that instead of trying to use different loop combinations to completely eliminate higher order error terms, they would instead choose their coefficients such that the leading order error terms become positive.

Introducing the parameter ϵ, they defined the following action,

$$S_P(\epsilon) = \beta \sum_x \sum_{\mu>\nu} \left[\frac{4-\epsilon}{3}(1 - P_{\mu\nu}(x)) + \frac{\epsilon - 1}{48}(1 - W_{\mu\nu}(x)) \right], \tag{2.20}$$

where $W_{\mu\nu}(x)$ denotes the clover average of the 2×2 squares (windows) touching the point x. Note that in (2.20), ϵ has been introduced such that $\epsilon = 1$ gives the standard Wilson action and $\epsilon = 0$ results in an $\mathcal{O}(a^2)$ improved action. Expanding (2.20) in terms of a and substituting the instanton solution in Eq. (2.15) gives

$$S_P^{\text{inst}} = \frac{8\pi^2}{g^2} \left[1 - \frac{\epsilon}{5} \left(\frac{a}{\rho_{\text{inst}}} \right)^2 + \frac{4 - 5\epsilon}{70} \left(\frac{a}{\rho_{\text{inst}}} \right)^4 \right], \tag{2.21}$$

where the $\mathcal{O}(a^2)$ term is directly proportional to $-\epsilon$. Thus, by making $\epsilon < 0$ the leading order discretisation errors become positive, and the modified action should preserve instantons.

In the interests of preserving locality we choose to use the traditional combination of plaquettes and rectangles as in the Symanzik improved action in preference to the combination of the 1×1 and 2×2 loops used in [75]. As emphasised in the introduction, this has the benefit of reducing the coefficient renormalisation that is applied to the

link paths, because of the smaller difference in the number of links utilised. This then enables precision tuning of ϵ.

We now introduce the parameter ϵ into the Symanzik improved action (2.18). By requiring that $\epsilon = 0$ gives the $\mathcal{O}(a^2)$ improved Symanzik action, and that $\epsilon = 1$ gives the standard Wilson action. This implies the following form for the action,

$$S(\epsilon) = \beta \sum_x \sum_{\mu>\nu} \left[\frac{5-2\epsilon}{3}(1 - P_{\mu\nu}(x)) - \frac{1-\epsilon}{12}\big((1 - R_{\mu\nu}(x)) + (1 - R_{\nu\mu}(x))\big) \right]. \quad (2.22)$$

Performing the expansion in a gives:

$$\begin{aligned} S(\epsilon) = a^4 \sum_x \sum_{\mu>\nu} \mathrm{tr} \Bigg[& \frac{1}{2} F_{\mu\nu}^2(x) - \frac{\epsilon\, a^2}{24} \left((\mathcal{D}_\mu F_{\mu\nu}(x))^2 + (\mathcal{D}_\nu F_{\mu\nu}(x))^2 \right) \\ & + \frac{a^4}{24} \Bigg(g^2(1-2\epsilon) F_{\mu\nu}^4(x) + \frac{5\epsilon - 4}{30} \left((\mathcal{D}_\mu^2 F_{\mu\nu}(x))^2 + (\mathcal{D}_\nu^2 F_{\mu\nu}(x))^2 \right) \\ & + \frac{2\epsilon - 1}{3} \mathcal{D}_\mu^2 F_{\mu\nu}(x) \mathcal{D}_\nu^2 F_{\mu\nu}(x) + \frac{1-2\epsilon}{4} (\mathcal{D}_\mu \mathcal{D}_\nu F_{\mu\nu}(x))^2 \Bigg) \Bigg] + O(a^{10}, g^4)\,, \end{aligned} \quad (2.23)$$

into which we substitute the instanton solution to find that

$$S^{\mathrm{inst}}(\epsilon) = \frac{8\pi^2}{g^2} \left[1 - \frac{\epsilon}{5} \left(\frac{a}{\rho_{\mathrm{inst}}} \right)^2 + \frac{14\epsilon - 17}{210} \left(\frac{a}{\rho_{\mathrm{inst}}} \right)^4 \right]. \quad (2.24)$$

As in (2.21), negative values of ϵ will result in a positive leading error term, and should preserve instantons.

We introduce the over-improvement parameter into the stout-link smearing algorithm by modifying the link combinations used in Eq. (2.9). Whereas the original $C_\mu(x) = \rho_{\mathrm{sm}} \sum\{1 \times 1 \text{ paths touching } U_\mu(x)\}$, the modified stout-link $C_\mu(x)$ has the form

$$\begin{aligned} \mathcal{C}_\mu(x) = \rho_{\mathrm{sm}} \sum \Bigg\{ & \frac{5-2\epsilon}{3} (1 \times 1 \text{ paths touching } U_\mu(x)) \\ & - \frac{1-\epsilon}{12} (1 \times 2 + 2 \times 1 \text{ paths touching } U_\mu(x)) \Bigg\}, \end{aligned} \quad (2.25)$$

and the definition of the smearing parameter ρ_{sm} is unchanged. Note that both forward and backward horizontally orientated rectangles are included in the 2×1 paths, such that $\Omega_\mu(x)$ resembles the local action.

2.4.2 Tuning

Of course, this now begs the question: How negative should ϵ be in order to preserve instantons? Perez *et al.* reported a value of $\epsilon = -1$ to preserve instantons, and indeed it does. However, just as positive values of ϵ can shrink instantons, so too can negative values cause instantons to grow. Just as small instantons can fall through the lattice, big instantons can grow so large that they are destroyed by the smoothing procedure [79].

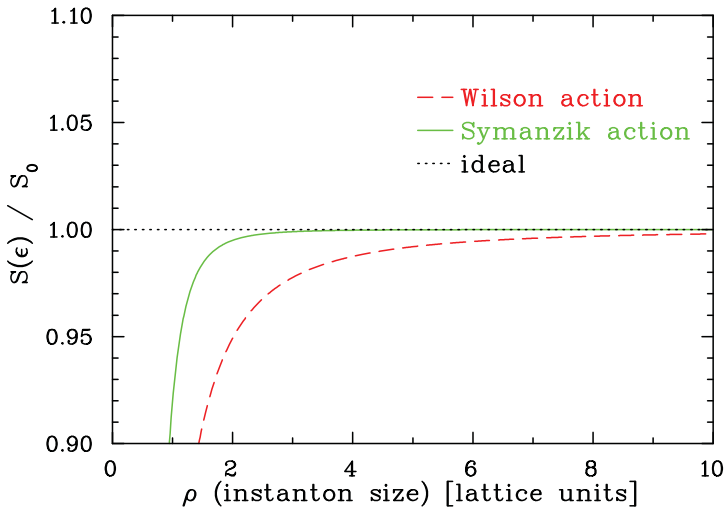

Figure 2.1: $S(\epsilon)/S_0$ versus the instanton size for the Wilson and Symanzik improved actions. The ideal action would produce a flat line at $S(\epsilon)/S_0 = 1$. The positive slope on both curves means that instantons will shrink if the Wilson or Symanzik actions are used to smooth the gauge field.

Additionally, one does not want to unnecessarily distort the instanton-like objects in the gauge field. Care must therefore be taken not to choose a value of ϵ that is too negative.

In order to quantify the selection of ϵ we propose that one considers the ratio $S(\epsilon)/S_0$, where $S_0 = 8\pi^2/g^2$ is the single instanton action. Ideally $S(\epsilon)/S_0$ should be equal to 1 for all values of the instanton size, $\rho_{\rm inst}$, as it is in the continuum.

Plots of $S(\epsilon)/S_0$ versus $\rho_{\rm inst}$ for the Wilson and Symanzik actions are shown in Fig. 2.1. Note that it is the slope of the curve that will govern whether an instanton shrinks or grows. Although the Symanzik action is closer to the ideal action than the standard Wilson action, the slope is still positive for all $\rho_{\rm inst}$ and using this action will shrink instantons.

The goal is now to select a value of ϵ that results in the flattest line possible, thereby ensuring the stability of instantons. A plot for three different values of ϵ is shown in Fig. 2.2. With $\epsilon = -1$ the curve for $\rho_{inst} > 1\,a$ is similar to the mirror image of the Wilson action. For $\rho_{\rm inst} > 1.5\,a$, $\epsilon = -0.25$ and -0.35 give curves closer to the ideal, however as $|\epsilon|$ is decreased the maximum occurs at larger $\rho_{\rm inst}$. Since it is the slope that is responsible for how an instanton's size changes, the maximum of $S(\epsilon)$ gives the dislocation threshold of the smearing algorithm. Assuming that any topological excitation of length $\geq 2\,a$ is not an unphysical UV fluctuation or lattice artifact, one should aim for a dislocation threshold of $\sim 2\,a$.

Given this, we propose that a value of $\epsilon = -0.25$ will be sufficient. This choice gives a dislocation threshold of $\sim 2.0\,a$, and a curve that is mostly flat down to values of $\rho_{\rm inst} \sim 1.7\,a$. The action $S(\epsilon)/S_0$ is also very close to the ideal.

In Fig. 2.3 we provide a comparison of the Perez *et al.* over-improved action, our over-improved action $S(-0.25)$, and the standard Wilson action. It is clear that $S(-0.25)$ will produce the best results, and presents an important advance beyond the work of

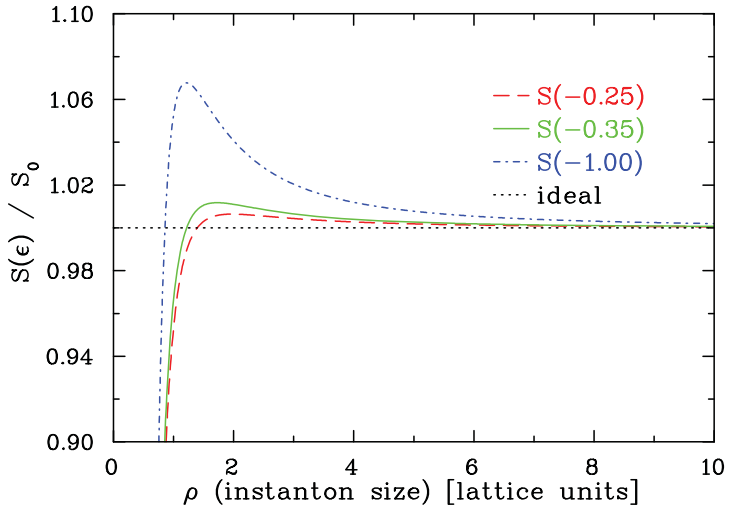

Figure 2.2: $S(\epsilon)$ for three different values of ϵ. The larger $-\epsilon$ is made the further the curve moves from the ideal behaviour and the sharper the maximum.

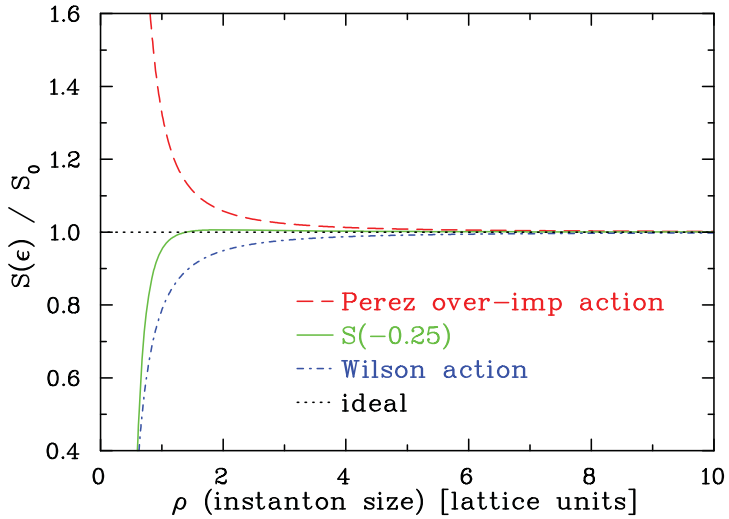

Figure 2.3: A comparison of $S(\epsilon)/S_0$ for the Perez over-improved action, our over-improved action $S(-0.25)$, and the standard Wilson action.

Ref. [75].

Given a value for ϵ one can find a suitable value for the smearing parameter, $\rho_{\rm sm}$. Starting from an arbitrary value, systematically increase $\rho_{\rm sm}$ until u_0 (the mean-plaquette value) no longer increases when smearing. This value sets an upper threshold for $\rho_{\rm sm}$ and one should then choose some $\rho_{\rm sm}$ suitably below this threshold. In what follows we use a value of $\rho_{\rm sm} = 0.06$. A typical value for standard stout-link smearing is $\rho_{\rm sm} \approx 0.1$. The over-improved algorithm is more sensitive to the smearing parameter than standard smearing because of the larger loops used in the smoothing procedure.

2.5 Algorithm comparisons

Given the selection of $\epsilon = -0.25$ it is now important to make a comparison of over-improved stout-link smearing with standard stout-link smearing. We are primarily concerned with the stability of the topological charge under smearing, and the structure of the gluon fields after smearing.

We use two sets of gauge fields for this study. Firstly, an ensemble of large 28×96 dynamical MILC lattices [76, 77], with light quark masses; $am_{u,d} = 0.0062$, $am_s = 0.031$. We will also use a quenched MILC ensemble of the same size and lattice spacing $a = 0.09$ fm. The gauge fields were generated using a Tadpole and Symanzik improved gauge action with $1 \times 1 + 1 \times 2 + 1 \times 1 \times 1$ terms and an AsqTad staggered dynamical fermion action for the $2 + 1$ flavours of dynamical quarks.

We also use quenched CSSM gauge fields created with the $\mathcal{O}(a^2)$ mean-field improved Lüscher-Weisz plaquette plus rectangle gauge action [80] using the plaquette measure for the mean link. The CSSM configurations are generated using the Cabibbo-Marinari pseudo-heat-bath algorithm [81] using a parallel algorithm with appropriate link partitioning [82]. To improve the ergodicity of the Markov chain process, the three diagonal SU(2) subgroups of SU(3) are looped over twice [69] and a parity transformation [83] is applied randomly to each gauge field configuration saved during the Markov chain process.

The local lattice operator [74] to represent the topological density for the stout-link smeared configurations is based on a highly improved field-strength tensor,

$$F^{imp}_{\mu\nu}(x) = k_1 C^{(1,1)}_{\mu\nu}(x) + k_2 C^{(2,2)}_{\mu\nu}(x) + k_3 C^{(1,2)}_{\mu\nu}(x) + k_4 C^{(1,3)}_{\mu\nu}(x) + k_5 C^{(3,3)}_{\mu\nu}(x) \qquad (2.26)$$

with

$$\begin{aligned} k_1 &= \frac{19}{9} - 55k_5 \ , \\ k_2 &= \frac{1}{36} - 16k_5 \ , \\ k_3 &= -\frac{32}{45} + 64k_5 \ , \\ k_4 &= \frac{1}{15} - 6k_5 \ , \end{aligned} \qquad (2.27)$$

and with

$$C^{(nm)}_{\mu\nu}(x) = \frac{1}{8}\left(W^{(n,m)}_{\mu\nu}(x) + W^{(m,n)}_{\mu\nu}(x)\right) \qquad (2.28)$$

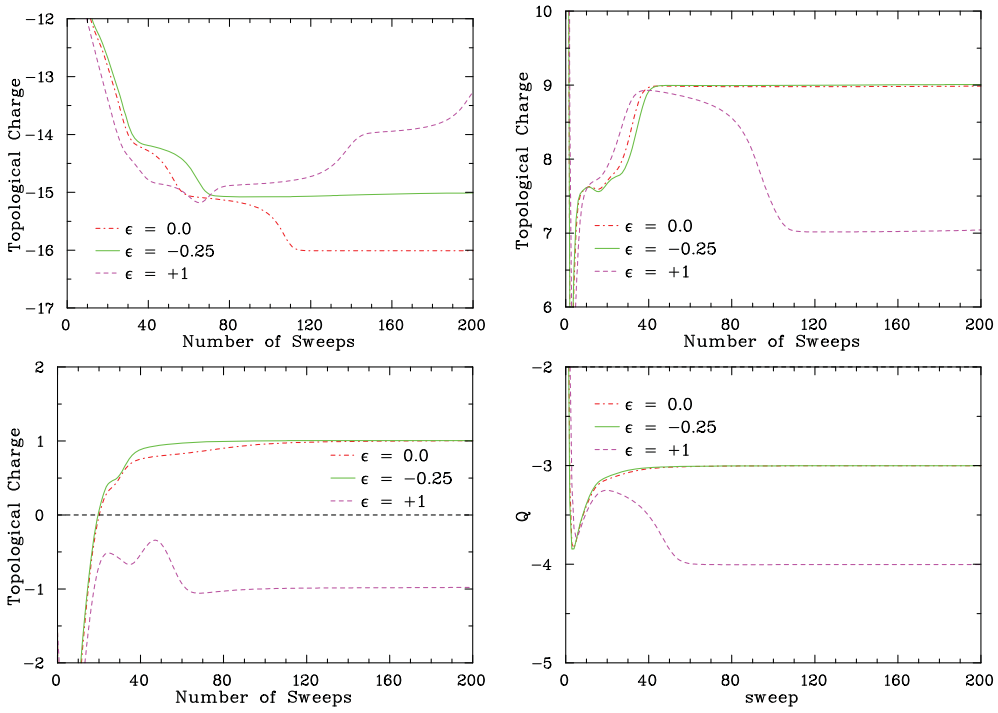

Figure 2.4: Plots showing how the topological charge evolves under standard ($\epsilon = 1$), Symanzik improved ($\epsilon = 0$), and over-improved ($\epsilon = -0.25$) stout-link smearing. The two top graphs are from an ensemble of 28×96 quenched gauge fields. The third graph is from an ensemble of 28×96 dynamical fields with light quark masses. The bottom is a smaller 16×32 quenched gauge field. The features of the graphs are explained in the main text.

being a symmetrised "clover sum" of $(n \times \hat{\mu}, m \times \hat{\nu})$ Wilson loops around the site x. A 3-loop improved field strength tensor can be achieved choosing $k_5 = 1/90$, such that $k_3 = k_4 = 0$. The topological charge density is then represented in the form

$$q_{sm}(x) = \frac{g^2}{16\pi^2} \mathrm{tr} \left(F_{\mu\nu} \tilde{F}_{\mu\nu} \right) , \tag{2.29}$$

as was already discussed in Chapter 1.

2.5.1 Topological charge

Let us first consider the evolution of the total topological charge of a gauge field under stout-link smearing. Typical studies in the past have rated a smearing algorithm's success by its ability to generate and maintain an integer charge. We will also use this test to evaluate the effectiveness of the smearing procedures. It should be noted that we will be smoothing extremely large $28^3 \times 96$ lattices. Due to the vast amount of non-trivial topological charge field fluctuations present it will take a lot of smoothing to generate a stable charge.

Fig. 2.4 provides a sample of 4 different gauge fields smeared by standard ($\epsilon = 1$), Symanzik improved ($\epsilon = 0$), and over-improved ($\epsilon = -0.25$) stout-link smearing. The

first and third are $28^3 \times 96$ quenched MILC gauge fields, the second is a $28^3 \times 96$ light dynamical MILC field, and the last is a smaller $16^3 \times 32$ quenched field.

The top-left graph shows an example of the over-improved stout-link smearing producing a stable result. In this instance the standard stout-link smearing curve is fluctuating widely, and is unable to reach a stable charge within 200 sweeps of smearing. The Symanzik improved smearing is better in that it stabilises at around 120 sweeps, however the over-improved stout-link smearing is clearly superior, stabilising 50 sweeps earlier. At around 70-120 sweeps there must exist a small instanton-like object that has been removed by the errors in the standard and improved smearing algorithms, but preserved by the tuned over-improved stout-link smearing.

The bottom-left graph is another typical example of what one sees when using the three different smearing algorithms. The standard stout-link smearing curve is still clearly the worst of the three, fluctuating the most. Meanwhile, the Symanzik and over-improved smearing algorithms are fairly similar in their behaviour. Both stabilise at the same integer charge, but the over-improved algorithm stabilises earlier. This is also the case in the top-right graph.

The final graph on the bottom-right is a sample of a $16^3 \times 32$ lattice. It is shown here to represent how it is generally easier to smooth a smaller gauge field. For the larger lattices, their larger size means that there is a greater probability of finding an unstable topological object and it becomes more difficult to achieve integer charges rapidly.

These four graphs all demonstrate the benefits of using an improved smearing algorithm over the standard stout-link smearing commonly used in the field at present. Over-improved stout-link smearing typically provides a topological charge that is stable over hundreds of smearing sweeps, and one that approaches an integer much more rapidly than the conventional stout-link smearing.

2.5.2 Topological charge density

For the next part of the analysis we will directly visualise the topological charge density of the gauge fields. Our aim is to observe the differences in the gauge fields revealed by using the standard and over-improved stout-link smearing algorithms.

To achieve this we will require a gauge field where the final topological charges from the two smearing procedures differ. The topological charge of such a configuration, as a function of the number of smearing sweeps, is shown in Fig. 2.5. It appears as though an anti-instanton is being destroyed by the standard stout-link smearing from about 20 sweeps onwards. It will be interesting to visualise $q(x)$ in this region to see if we can observe this behaviour. Indeed, by considering the differences in the charge density, we are able to locate the "anti-instanton" that is removed by the standard stout-link smearing.

In Fig. 2.6 we show how the anti-instanton is affected by the standard stout-link smearing, and in Fig. 2.7 we have the corresponding charge density from the over-improved stout-link smearing. The pictures present a single slice of the charge density of the 4-D lattices as they evolve under the stout-link smearing.

After 30 sweeps we see that both smearing methods have revealed a similar vacuum structure. The effects of the errors in the standard smearing are first seen after 33 sweeps, when the anti-instanton like object on the right begins to unwind in the upper-right

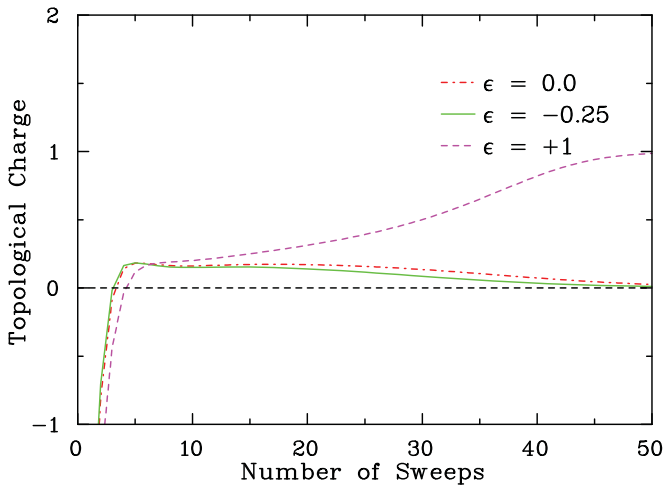

Figure 2.5: The topological charge evolution under smearing for a 16×32 lattice. We see that when standard smearing ($\epsilon = 1$) is used an anti-instanton is destroyed at around 20-40 sweeps. Visualisations of the topological charge density in this region are discussed in the following text.

corner. Here the charge density is approaching zero and therefore is not rendered. In a few sweeps the action density in this region will manifest itself in the opposite winding, largely eliminating the total topological charge. The net effect is to suggest that the instanton-like object on the right invades the neighbouring negative object. However, the change in Q indicates that this is not an instanton - anti-instanton annihilation. At this point the majority of the negative topological charge density is lost and the total Q for the configuration approaches 1. This kind of phenomenon should not be seen as filtering is applied to a lattice, and indeed it does not occur when using the over-improved smearing.

After 36 sweeps the opposite winding has grown in size and it continues to grow in size as more smearing is applied to the lattice. After 39 sweeps the negatively charged object has all but disappeared. Although not shown, eventually the neighbouring positive object expands to engulf the region originally occupied by the negatively charged excitation.

Here we have directly demonstrated how the discretisation errors in the standard stout-link smearing algorithm have resulted in an erroneous picture of the vacuum, and how by modifying these errors in the over-improved algorithm we are able to present a more accurate representation of the vacuum.

2.5.3 Single instanton evolution

We can also contrast the effects of different smearing algorithms by smearing a single instanton gauge field configuration. We create an instanton in singular gauge [84] and avoid Nahm-transform issues [79] via the action appearing at the boundaries of the lattice. Given that over-improved stout-link smearing with $\epsilon = -0.25$ has a dislocation threshold of about $2\,a$ we generate a gauge field containing a single instanton of size

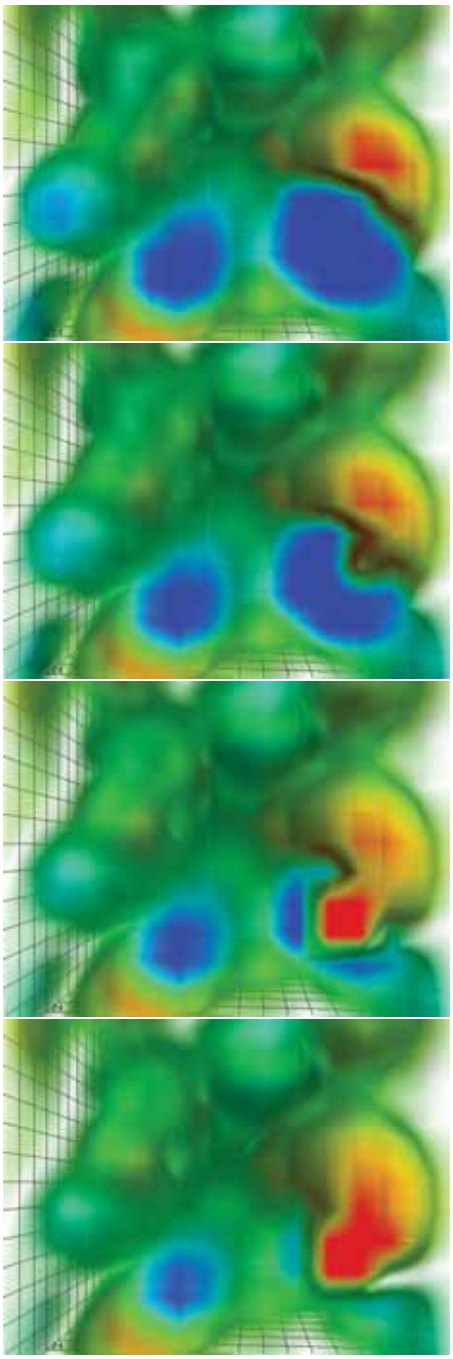

Figure 2.6: The evolution of the topological charge density for various sweeps of standard stout-link smearing. The sweeps shown are; 30 (top), 33, 36, 39 (bottom). Blue to green represents negative topological charge and red to yellow represents positive. We see that a rather large anti-instanton is unstable under this smearing and is removed from the lattice, presenting an erroneous view of the vacuum.

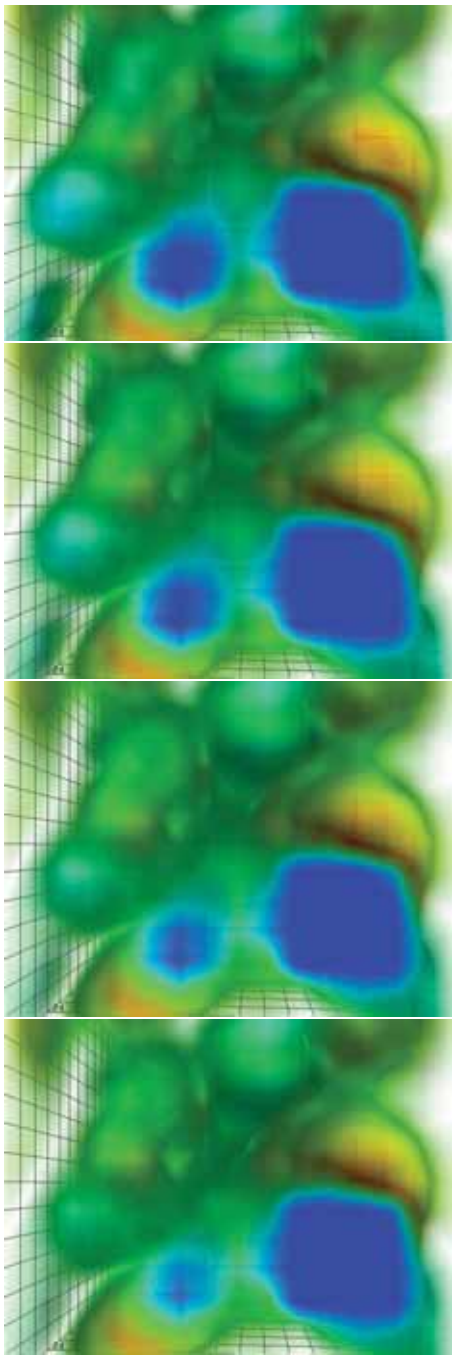

Figure 2.7: A visualisation of the topological charge density of the same gauge field shown in Fig. 2.6, this time with over-improved stout-link smearing. We see that in this case the anti-instanton in the lower right corner of the lattice is stable under smoothing, and remains stable for at least 200 sweeps.

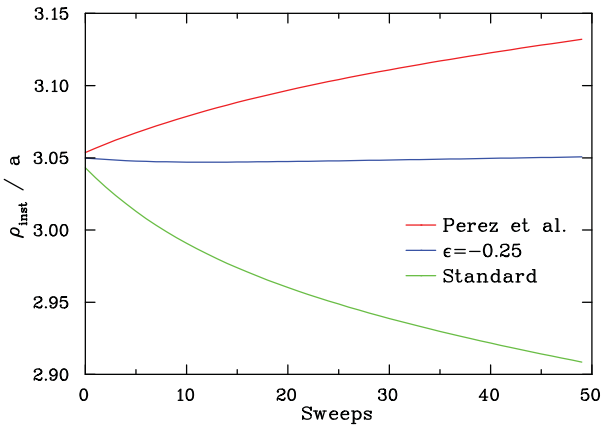

Figure 2.8: The size evolution of single instanton under three different types of smearing. $\epsilon = 0.25$ refers to our over-improvement scheme, whilst Perez *et al.* denotes a stout-link implementation of their over-improvement method. Standard refers to standard unimproved stout-link smearing. The instanton is only stable under our proposed over-improvement scheme.

$\rho_{inst} = 3\,a$.

We compare our over-improved smearing against standard stout-link smearing and a stout-link implementation of the Perez *et al.* over-improvement scheme. An instanton of this size should stay relatively constant under over-improved smearing at $\epsilon = -0.25$. From Fig. 2.3 we anticipate that the Perez *et al.* over-improvement scheme will cause the instanton to grow in size. Similarly, standard stout-link smearing is expected to shrink the instanton. The size of the instanton is monitored by fitting the classical instanton action profile to the lattice action density in a 3^4 hypercube located at the centre of the instanton.

The instanton's size evolution is presented in Fig. 2.8. We see that the instanton's size has remained constant under over-improved smearing. As predicted, Perez *et al.*'s implementation of over-improvement has caused the instanton to grow. In a study of QCD vacuum structure this would lead to an over-estimation of instanton sizes in the vacuum. Also as predicted, using standard stout-link smearing has caused the instanton to shrink. Further smearing would destroy the instanton. This calculation showcases the obvious need for over-improvement in the stout-link smearing algorithm.

2.6 Summary

In this chapter we have demonstrated how to define an over-improved stout-link smearing algorithm, with the aim of preserving instanton-like objects on the lattice. To the best of our knowledge this is the first time link paths beyond the staple have been included in the stout-link smearing algorithm.

Using maximally-local improvement we presented a new quantitative method of selecting a suitable value of the parameter ϵ. With the procedure defined, we demonstrated the success of the over-improved stout-link algorithm in preserving topological structures

which were destroyed when using the standard stout-link smearing algorithm. This was done by analysing both the topological charge and through visualisations of the topological charge density. We also performed a comparison of the over-improved smearing method with standard methods by smoothing a single instanton of size $\rho_{inst} = 3.0a$. Over-improved stout-link smearing is the only algorithm capable of smoothing an instanton of this size without distorting it.

This work highlights the need for improvement schemes to be incorporated into today's modern smearing algorithms. Over-improved stout-link smearing can be used in future studies of vacuum structure or other similar applications, where preserving topology on the lattice is important. Of particular interest is a quantitative comparison with the overlap-Dirac measure of topological charge density presented in Chapter 3. The algorithm is also used to assess the impact of dynamical-fermions on QCD vacuum structure in Chapter 5.

Chapter 3

Comparing the overlap operator to over-improved smearing

The content of this chapter is based on the publication: E. M. Ilgenfritz, D. Leinweber, P. Moran, K. Koller, G. Schierholz and V. Weinberg, Phys. Rev. *D 77, 074502 (2008) [arXiv:0801.1725 [hep-lat]].*

This chapter presents a detailed comparison between the topological structure of quenched QCD, as revealed by the previously discussed over-improved stout-link smearing, and a similar analysis made possible by the overlap-fermionic topological charge density both with and without a variable ultraviolet cutoff λ_{cut}. The matching is twofold, provided by fitting the density-density two-point functions on one hand and by a point-by-point fitting of the topological densities according to the two methods. We point out the similar cluster structure of the topological density for moderate smearing and 200 MeV $< \lambda_{cut} <$ 600 MeV, respectively. We demonstrate the relation of the gluonic topological density, after extensive smearing, to the location of the overlap zero modes and the lowest overlap non-zero mode as found from the unsmeared configurations.

3.1 Introduction

Massless overlap fermions [31, 85] have provided us with a fermionic definition of topological charge [86, 87]. This offers the advantage that, by truncating to the overlap modes with $|\lambda| < \lambda_{cut}$, the effect of ultraviolet filtering can be studied [88] without changing the gauge field itself. A broad study of different aspects of vacuum structure, so far for quenched QCD, was performed in Ref. [89].

On the other hand, during the 80's procedures of cooling or smearing of gauge fields were proposed to exhibit the infrared structure of gauge fields [66, 90]. This has been considered with reservations because it is difficult to assess in which aspect the gauge field configuration could have changed under this procedure. The practitioners of cooling/smearing, in particular those who were focusing on vacuum structure in the form of extended, smooth (semi-classical) structures, have continued to improve their techniques: cooling with improved actions [91], restricted improved cooling [92] etc). Over-improved cooling [75, 93] has been applied in order to prevent instantons or other topological

excitations from collapsing. In the previous chapter we applied the concept of over-improvement to the stout-link smearing algorithm.

In this chapter, we want to characterise the subsequent mapping "link → stout link" as a particular relaxation scheme, eventually leading to a finally classical configuration. One obvious way to discuss this process is to record the local distribution of topological charge density expressed by an improved [74] gluonic definition of field strength and topological density. We shall compare the emergent structures with the topological density provided by the overlap definition [89] with different levels of ultraviolet filtering. Surprisingly, the overlap topological charge density without filtering, that recently has been found to form lower-dimensional structures [89, 94, 95], corresponds to a few steps of smearing. This comparison will lead us to a one-to-one mapping of the ultraviolet cutoff λ_{cut} (mode truncation in the overlap picture) to the number of stout-link smearing iterations over a wide range of smearing iterations. In a similar spirit, the correspondence of APE smearing [96], Laplacian filtering [97] and the topological density filtered according to another Ginsparg-Wilson Dirac operator [98, 99] has been studied recently [100, 101].

Only a few iterations of stout-link smearing are necessary before structures become recognisable with the gluonic definition of the topological density, and these structures are surprisingly far from 4D extended, sign-coherent lumps, such that the topological density compares well with the unfiltered overlap definition. We have two criteria to establish this relation between smearing and filtering. First, it is the behaviour of the two-point correlation function of the topological density that emerges from the respective definition. The second is the actual site-by-site difference of the topological density profile over a set of lattice configurations. The quality of the latter coincidence is surprisingly good, which supports the reliability of both methods to explore the vacuum structure.

Finally, however, this relation becomes loose because stout-link smearing turns the configurations into piecewise classical fields which apparently resemble instantons and anti-instantons. Although the coherence among the lowest overlap modes guarantees a relatively simple picture of the fermionic topological density and the ultraviolet filtered gluonic field strength with low cutoff λ_{cut} [89], there is no argument as to why the overlap picture should be in correspondence to a (link-wise) classical lattice configuration.

It is intriguing to see that the instanton-like structure that is revealed in this late stage of smearing corresponds to the overlap zero mode(s) and the lowest pair(s) of overlap non-zeromodes obtained for the respective unsmeared (equilibrium) configuration. A similar observation has already been made by Negele *et al.* [102]. In Ref. [95] the authors presented a cluster analysis of individual eigenmodes of the overlap Dirac operator. It turns out that the moderate number of clusters that the zero and first non-zero modes consist of (at a level of scalar density below the peak values) are pointing towards the positions where instantons and anti-instantons appear later.

This chapter is organised as follows; in Sec. 3.2 we briefly introduce the overlap operator, in Sec. 3.3 we describe the matching between smearing and ultraviolet filtering, according to the two-point correlator and according to a global fitting of the profile of charge. In Sec. 3.4 we try to relate the clusters that both definitions exhibit to each other. In the final stadium of smearing we shall confront the emergent semi-classical

lumps with the lowest eigenmodes (zero mode and lowest non-zero mode) of the original configurations.

3.2 Configurations and the overlap definition of topological density

The configurations underlying this comparison stem from an extended investigation published in Ref. [89]. The configurations are taken from an ensemble of $16^3 \times 32$ quenched lattices generated with the tadpole improved Lüscher-Weisz action at $\beta = 8.45$.

The (massless) overlap Dirac operator is constructed for the Wilson-Dirac input kernel $D_W = M - \rho/a$, M being the massless Wilson-Dirac operator with $r = 1$, and $\rho = 1.4$. The corresponding solution of the Ginsparg-Wilson relation reads as follows

$$D(0) = \frac{\rho}{a}\left(1 + D_W/\sqrt{D_W^\dagger D_W}\right) = \frac{\rho}{a}\left(1 + \gamma_5 \mathrm{sgn}(H_W)\right) \ , \tag{3.1}$$

with $H_W = \gamma_5 D_W$. Circa 150 overlap eigenmodes have been obtained per configuration. They have been used to construct ultraviolet smeared topological densities according to a cut-off $\lambda_{cut} = 200$ MeV, 400 MeV and 635 MeV. For half of the subset of 10 configurations particularly considered in the present study we have also calculated for Refs. [89, 95] the overlap topological density without mode truncation, the "all-scale" topological density.

The spectrum eventually consists of some zero modes, in addition to pairs of non-zero modes of globally vanishing chirality. The topological density can be formally obtained from the trace of the overlap Dirac operator [87]

$$q(x) = -\mathrm{tr}\left[\gamma_5\left(1 - \frac{a}{2}D(0;x,x)\right)\right] \ . \tag{3.2}$$

Using the spectral representation of the overlap Dirac operator, a family of ultraviolet filtered topological charge densities labelled by $q_{\lambda_{cut}}(x)$ can be obtained [88, 103],

$$q_{\lambda_{cut}}(x) = -\sum_{|\lambda|<\lambda_{cut}}\left(1 - \frac{\lambda}{2}\right)\psi_\lambda^\dagger(x)\gamma_5\psi_\lambda(x) \ . \tag{3.3}$$

The topological charge of each configuration fulfils the Atiyah-Singer index theorem [86]

$$Q = n_- - n_+ \ . \tag{3.4}$$

Note that the zero modes of any given configuration carry the same chirality.

In the following sections we shall demonstrate how the above-mentioned family of densities is well represented by the gluonic topological charge density after an appropriate number of iterations of stout-link smearing. The over-improved stout-link smearing is the same as was discussed in Chapter 2.

n_{sw}	$Q=-8$	$Q=0$	$Q=-1$	$Q=-7$	$Q=0$
1	0.9954	-0.0001	1.0054	0.6442	0.0000
2	0.9634	-0.0001	-21.5369	0.7987	-0.0001
3	0.9494	-0.0001	3.6497	0.8990	-0.0001
4	0.9585	-0.0002	1.8690	0.9485	-0.0001
5	0.9760	-0.0004	1.4537	0.9728	-0.0001
6	0.9903	-0.0008	1.2736	0.9843	-0.0002
7	0.9982	-0.0015	1.1725	0.9894	-0.0004
8	1.0010	-0.0030	1.1105	0.9915	-0.0006

Table 3.1: Table of Z_{sm} values for the initial five configurations. The normalisation procedure is only valid for $Q \neq 0$ and works best for large $|Q|$. The fluctuating values for the configuration with $Q=-1$ occurring at $n_{sw}=2$ are due to Q_{sm} being approximately 0 at this point.

3.3 Matching stout-link smearing to overlap filtering

3.3.1 Matching the two-point correlator

The two-point correlators for stout-link smearing and overlap filtering are matched using a minimisation of the sum of the absolute difference between the correlators. That is, we compute

$$\min\left(\sum_x |\langle q(x)q(0)\rangle_{sm} - \langle q(x)q(0)\rangle_{\lambda_{cut}}|\right) \tag{3.5}$$

as a function of the number of smearing sweeps, n_{sw}, for fixed λ_{cut}.

The topological charge of each overlap filtered configuration is integer valued because they satisfy the Atiyah-Singer index theorem (3.4). For stout-link smearing it can take up to 10 sweeps of smearing to achieve an integer charge on these $16^3 \times 32$ lattices. In order to compare overlap filtering and stout-link smearing for $n_{sw} < 10$ in a fair way a non-perturbative normalisation is applied. Given that we know the topological charge Q from the overlap configurations, we calculate, for each number of smearing sweeps n_{sw}, a normalisation factor Z_{sm} via

$$Q = Z_{sm} \sum_x q_{sm}(x)\,, \tag{3.6}$$

and $q_{sm}(x)$ is then normalised through $q_{sm}(x) \to Z_{sm}\, q_{sm}(x)$. This ensures that $Q_{sm} = Q$. We also experimented with an alternate normalisation where we matched the absolute values of the topological charge density, however this proved less fruitful.

Typical values of Z_{sm} are provided in Table 3.1. For obvious reasons, it is only possible to extract a Z_{sm} factor for $Q \neq 0$, and the procedure works best for Q far from zero. Consequently, the best results are found for the configurations where $Q = -7$ and -8, where the Z_{sm} values rapidly approach 1. This is also the case for the

λ_{cut}	$Q=-8$		$Q=0$		$Q=-1$		$Q=-7$		$Q=0$	
full density	005	005	005	—	005	005	005	004	005	—
all known modes	039	039	043	—	036	036	038	037	034	—
634 MeV	052	052	064	—	048	048	055	055	048	—
400 MeV	127	127	183	—	109	108	139	138	115	—
200 MeV	248	247	300	—	232	232	300	300	271	—

Table 3.2: The best matches for the two-point correlators of five different configurations as determined by Eq. (3.5). For each configuration, the two columns give the number of smearing sweeps that correspond to the best match for a given level of UV filtering. In each case the left column gives the best match for the unnormalised gluonic density and the right column gives the best match for the gluonic density normalised with Z_{sm} (see text). The right columns for the $Q = 0$ configurations are absent because the normalisation procedure fails in these cases.

configuration with $Q = -1$, however Z_{sm} fluctuates at $n_{sw} = 2$, which is due to Q_{sm} being approximately 0 at this point.

In Table 3.2 we present the best matches for the two-point correlators between the filtered overlap densities and the stout-link smeared gluonic densities. Configurations have been used for which the unfiltered overlap topological density (full density) has been measured. The correlators of the fermionic topological density including all known modes, with $\lambda_{cut} = 634$ MeV, with $\lambda_{cut} = 400$ MeV and with $\lambda_{cut} = 200$ MeV are matched against the smeared gluonic correlators.

We show in Fig. 3.1 the two-point correlator of the topological density for a single configuration represented by the unfiltered fermionic topological density (full density) of Eq. (3.2) of the equilibrium configuration on one hand and for the gluonic definition of Eq. (2.29) after 5 smearing steps. It is remarkable that the two correlators follow each other's fluctuations at larger distance. There is some difference in normalisation of the negative peak. This configuration has $Q_{ferm} = -8$, and the gluonic definition gives $Q_{sm} = -8.19$. In this case the "non-perturbative" renormalisation would even slightly increase the difference between the curves as the three curves in Fig. 3.2 show.

In Fig. 3.3 the density-density two-point correlator for the same configuration is compared for an ultraviolet cutoff $\lambda_{cut} = 634$ MeV for the fermionic, overlap definition and the gluonic definition after 52 smearing steps. The filtered correlators match perfectly. The third curve shows the correlator with the gluonic definition after 45 smearing steps. This refers to the case of an optimal point-by-point matching of the densities, as discussed in the next section. The corresponding correlator is somewhat higher and steeper because it uses slightly less smearing iterations.

Fig. 3.4 shows the same configuration for a lower ultraviolet cutoff $\lambda_{cut} = 400$ MeV. After 127 smearing steps the correlator for the gluonic definition fits the correlation function perfectly. Somewhat less smearing steps (103), again optimally fitting the fermionic topological density point by point, tend to overestimate the correlator.

All smeared correlators discussed above were generated using a smearing parameter of $\rho_{sm} = 0.06$. By using a different value for ρ_{sm} it is possible that a different number of smearing sweeps will provide the best fit. This is because the amount of smearing applied

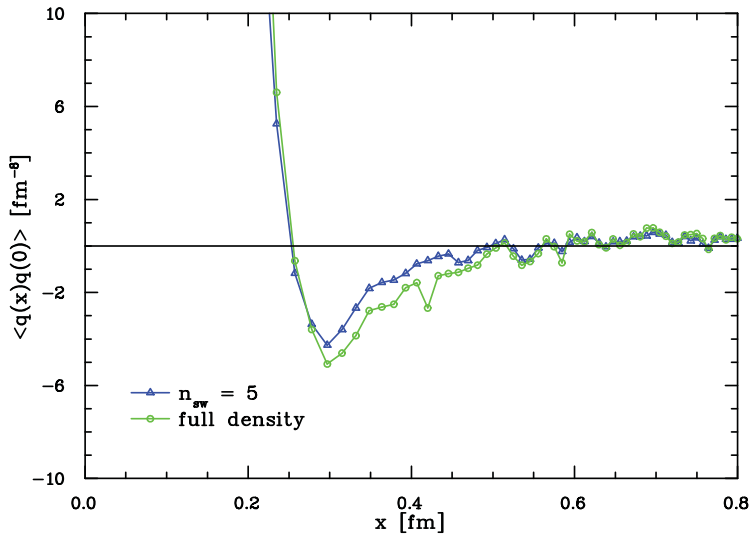

Figure 3.1: The two-point function of the fermionic topological density for one configuration shown without mode truncation compared with the bosonic definition after 5 steps of smearing.

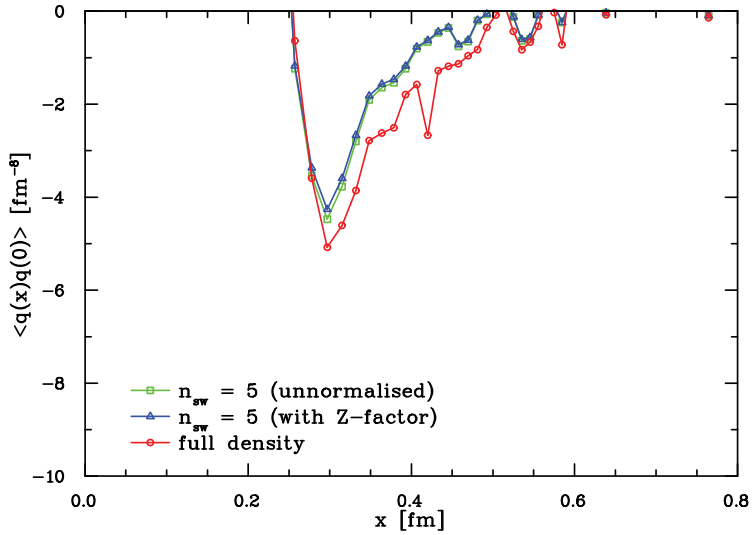

Figure 3.2: The same as in Fig. 3.1 with the effect of the renormalisation factor $Z_{sm} = Q_{ferm}/Q_{sm}$ also shown. ($Q_{ferm} = 8$, $Q_{sm} = 8.19$)

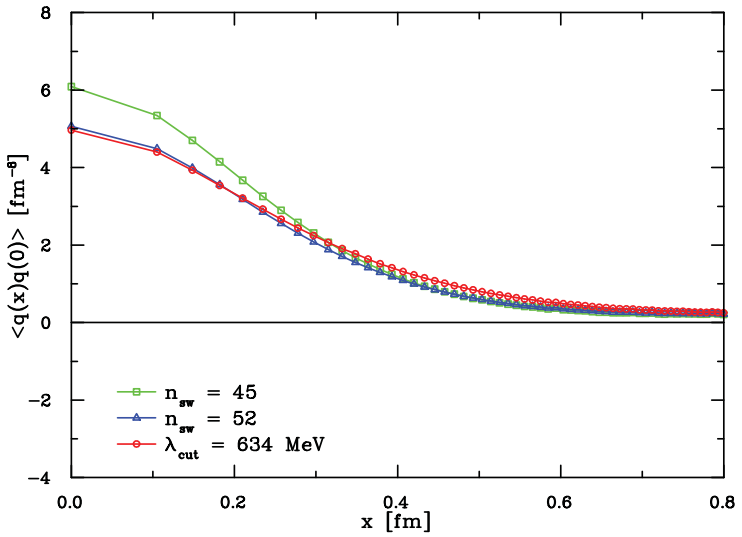

Figure 3.3: The two-point function of the fermionic topological density with an UV cutoff at $\lambda_{cut} = 634$ MeV compared with the bosonic definition after 52 steps of smearing when the correlator is fitted best. Smearing after 45 steps leads to the best global matching of the density $q_{\lambda_{cut}}$ with $\lambda_{cut} = 634$ MeV, but the correlator is steeper.

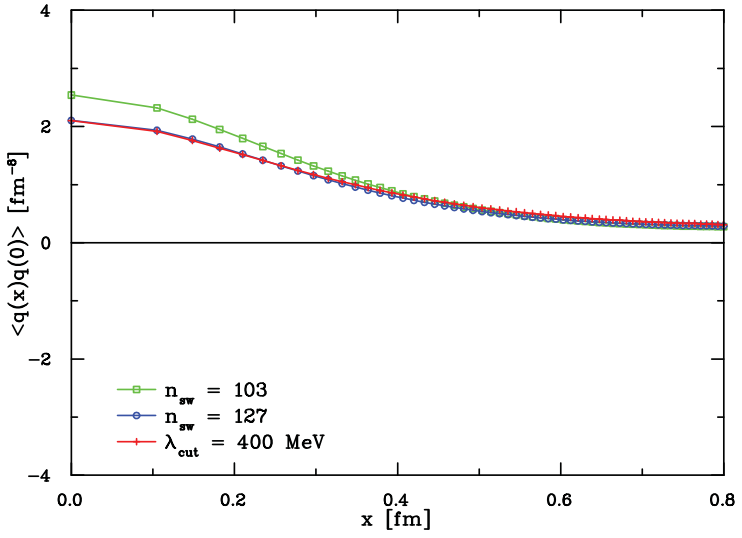

Figure 3.4: The same as Fig. 3.3 with an UV cutoff at $\lambda_{cut} = 400$ MeV fitted best by the bosonic definition after 127 steps of smearing. Smearing after 103 steps leads to the best global matching of the densities, but the correlator is steeper.

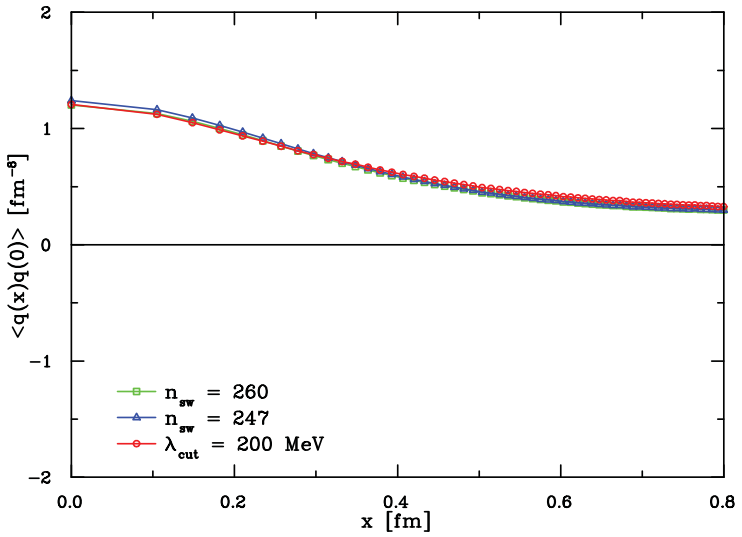

Figure 3.5: The same as Figs. 3.3 and 3.4, now with an UV cutoff at $\lambda_{cut} = 200$ MeV fitted best by 248 sweeps of smearing. 260 sweeps of smearing gives the best match for the topological charge densities.

to a gauge field is proportional to $\rho_{sm}\, n_{sw}$. By varying ρ_{sm} as well as the number of sweeps one has greater fine-grained control over the matching. Using a variable ρ_{sm}, but holding $n_{sw} = 5$ fixed, and applying this to the same configuration considered previously we find that $\rho_{sm} = 0.055$ provides the best match for the unfiltered topological density.

A comparison of some different values for for the smearing parameter is provided in Fig. 3.6. As expected, increasing ρ_{sm} results in a suppression of the negativity of the two-point correlator. Although $\rho_{sm} = 0.055$ provides the best match through a minimisation of the sum of the differences in the two-point functions, $\rho_{sm} = 0.06$ gives the best match for the x-intercept. The two-point function for this larger ρ_{sm} also appears to have a similar shape to the two-point function of the full fermionic topological density.

3.3.2 Matching the topological density point by point

We now aim to match the filtered fermionic densities with the smeared gluonic densities through a point-by-point matching of the respective topological charge densities $q_{\lambda_{cut}}(x)$ and $q_{sm}(x)$. Given some filtered fermionic topological charge density we compare it against the gluonic density $q_{sm}(x)$ after some number of sweeps by calculating the absolute value of the difference between the respective q at each x. To find the best match we compute the minimum of the sum of the differences,

$$\min \left(\sum_x |q_{sm}(x) - q_{\lambda_{cut}}(x)| \right) , \tag{3.7}$$

as a function of the number of smearing sweeps, n_{sw}, for fixed λ_{cut}. The non-perturbative normalisation of Eq. (3.6) will also be applied. The best matches are presented in Table 3.3. For a small number of sweeps the importance of the Z_{sm} normalisation is

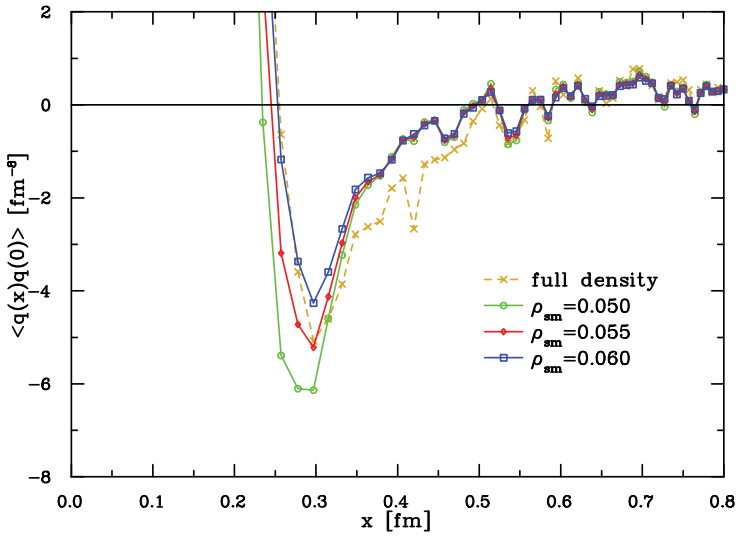

Figure 3.6: A comparison of the smeared two-point function for three different values of the smearing parameter, ρ_{sm}. The configuration shown is the same as that used in the previous figures. A best match as dictated by Eq. (3.5) is given by $\rho_{sm} = 0.055$, however $\rho_{sm} = 0.06$ gives the best match for the x-intercept.

λ_{cut}	$Q=-8$		$Q=0$		$Q=-1$		$Q=-7$		$Q=0$	
full density	300	005	300	—	300	006	300	005	300	—
all known modes	037	036	037	—	035	035	035	035	033	—
634 MeV	045	045	048	—	044	044	048	048	044	—
400 MeV	103	103	098	—	103	103	087	087	093	—
200 MeV	261	260	300	—	236	236	192	191	187	—

Table 3.3: Best matches for $q(x)$ between the filtered overlap densities and smeared gluonic densities. The left columns contain the best matches with the unnormalised gluonic densities, and the right columns contain the best matches when including the Z_{sm} factor. We see the importance of the Z_{sm} normalisation factor when attempting the match the full fermionic density. The right columns are absent for the $Q = 0$ configurations because the normalisation method does not work for this Q.

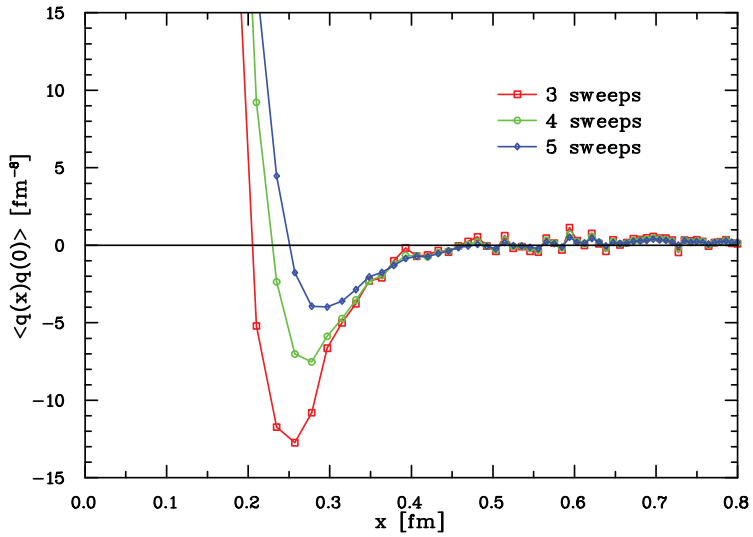

Figure 3.7: The two-point function as a function of smearing sweeps. The correlator has been averaged over the two configurations with $Q = -7$ and $Q = -8$. Both charge densities were normalised by an average of the Z_{sm} values for the two configurations. As the number of sweeps is decreased the negative dip increases in magnitude and the x-intercept moves further toward zero.

apparent. Visualisations of some configurations are shown later in Sec. 3.4.

3.3.3 Towards the no-smearing limit

Increased smearing leads to a flattening of the Euclidean two-point function. It follows that less sweeps of smearing leads to an increasing negative dip in the correlator, and we now study the behaviour of the two-point function in the limit $n_{sw} \to 0$. After only one or two sweeps of smearing there is a non-trivial renormalisation that must be applied to the topological charge density. From Table 3.1 we see that after three smearing iterations the Z_{sm} factors for the $Q = -7$ and $Q = -8$ configurations are in relatively good agreement. We can therefore study the correlator for $n_{sw} \geq 3$, averaging over these two configurations.

Such a comparison leads to a series of correlators which are displayed in Fig. 3.7. The x-intercept also moves further towards zero.

3.4 Comparison of topological clusters

3.4.1 Clusters of both topological densities compared for weak stout-link smearing

Using the matching of Eq. (3.7) we are able to directly compare the overlap topological charge density with some level of UV filtering to a given number of stout-link smearing sweeps. In an early stadium of stout-link smearing the topological density does not yet

show classical, instanton-like features. What is meant by "instanton-like features" and how they gradually emerge from stout-link smearing is illustrated for a configuration with $Q = -1$ in Fig. 3.8. The solid lines represent the relation

$$|q(x_0)| = \frac{6}{\pi^2 \rho_{inst}^4} \ , \tag{3.8}$$

typical for the (anti)instanton solution, between the gluonic topological charge density in the maxima x_0 of the modulus of the density $|q_{sm}(x)|$ and the "instanton radii" ρ_{inst} obtained from a fit of the curvature of the action density in the points neighbouring x_0.

The upper plot has to be considered with a grain of salt because a closer look at the maxima reveals a substantial lack of isotropy of the peaks of topological density which is however implicitly assumed in the fits of ρ_{inst}. The marked difference in this respect between 5 and 40 smearing steps is visible in Fig. 3.9 showing a certain timeslice of the same configuration as in Fig. 3.8.

For a moderate amount of smearing and filtering, respectively, the two topological density definitions are faithfully exhibiting the outstanding clusterisation of charge, provided the cut-off λ_{cut} and the number of stout-link smearing steps are optimally tuned to each other. This is exemplified by Fig. 3.10 which shows the same time-slice of a $Q = 0$ configuration, on the left-hand side portrayed by the overlap-fermionic topological density with $\lambda_{cut} = 634$ MeV and on the right-hand side by the gluonic topological density after 48 stout-link smearing steps.

In Fig. 3.11 we show the fermionic density of the $Q = -8$ configuration, with $\lambda_{cut} = 400$ MeV and the gluonic density after 103 stout-link smearing steps. In this stadium of smearing, the bias in favour of classical lumps is already visible.

Besides the similarity between the two methods, the tendency towards classical lumps becomes obvious in Fig. 3.12. This figure shows the $Q = -7$ configuration with a cutoff of $\lambda_{cut} = 200$ MeV. At this level of UV filtering the best match is provided by 193 sweeps of over-improved stout-link smearing. In this stadium of smearing, in particular because of the over-improved action built into the smearing, the minority positive charge has become stabilised compared with what the fermionic view shows.

3.4.2 Zero modes and lowest non-zeromodes and the instanton content after long smearing

For long smearing with essentially more than 100 smearing steps, the similarity of the topological densities slowly becomes less perfect. Still, the position of the gluonic topological lumps is not completely arbitrary from the point of view of the original configuration. The zero modes (if $Q \neq 0$) and the lowest non-zero modes contain a high predictive power over where these lumps will appear.

For 200 smearing steps, this is illustrated in Fig. 3.13 by a $Q = -1$ configuration. In the left panel the gluonic topological density is shown, in the right panel the scalar density of the zero mode. The zero mode covers three distinct centres of topological charge of appropriate sign only in the selected time-slice. Two more examples of total charge $Q = \pm 1$ are shown in Figs. 3.14 and 3.15. One sees that the zero mode does not always cover all regions of appropriate charge. In other words, the gluonic version of the

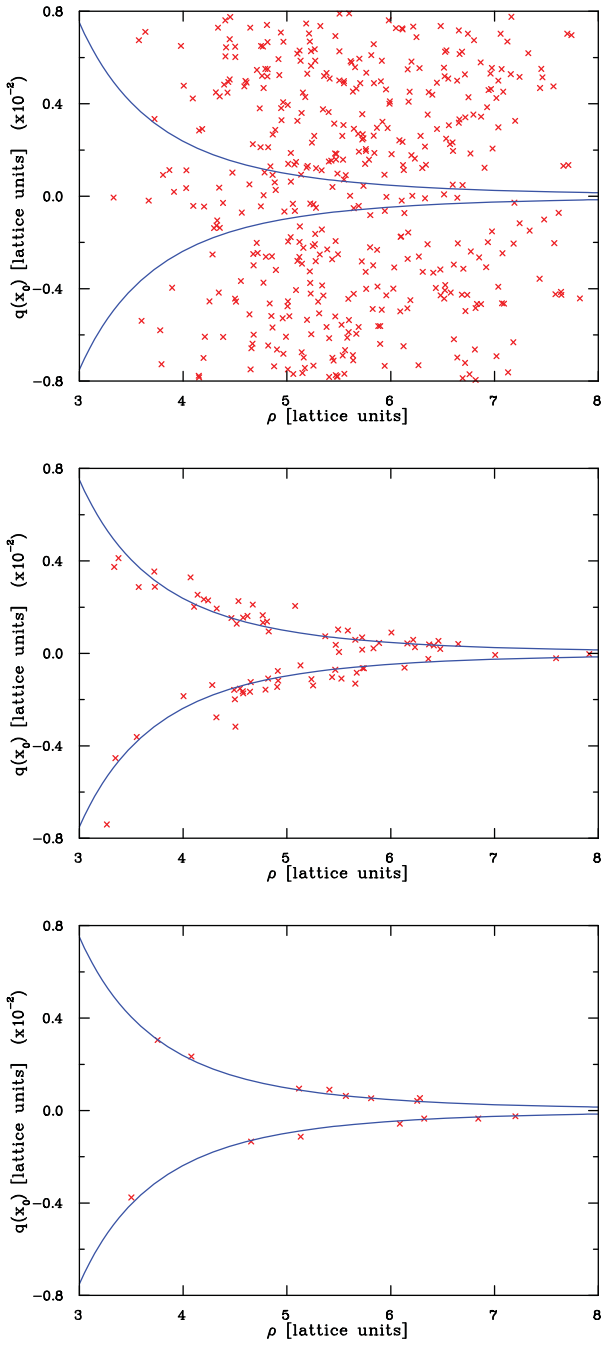

Figure 3.8: Three scatter plots showing the increasing instanton-like correlation between the gluonic topological charge density in the maxima x_0 of its modulus $|q_{sm}(x)|$ and the "instanton radii" ρ_{inst} (see text). The solid lines represent the (anti)instanton-like relation between the two cluster parameters. The upper plot shows a huge number of maxima after 5 smearing steps, without any relation between density and size. The middle and bottom plots show a decreasing number of maxima and an increasing accuracy of the instanton-like relation after 40 and 200 smearing steps, respectively.

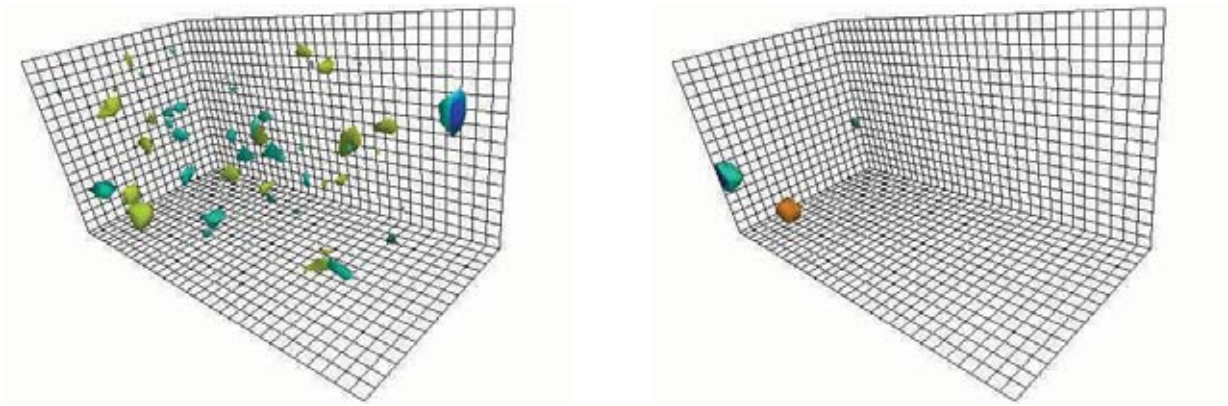

Figure 3.9: The gluonic topological charge density very close to the maxima in some timeslice of the same configuration as analysed in Fig. 3.8 after 5 (left) and 40 stout-link smearing iterations (right). In colour: negative density blue/green, positive density red/yellow. In grey-scale: negative density dark, positive density light.

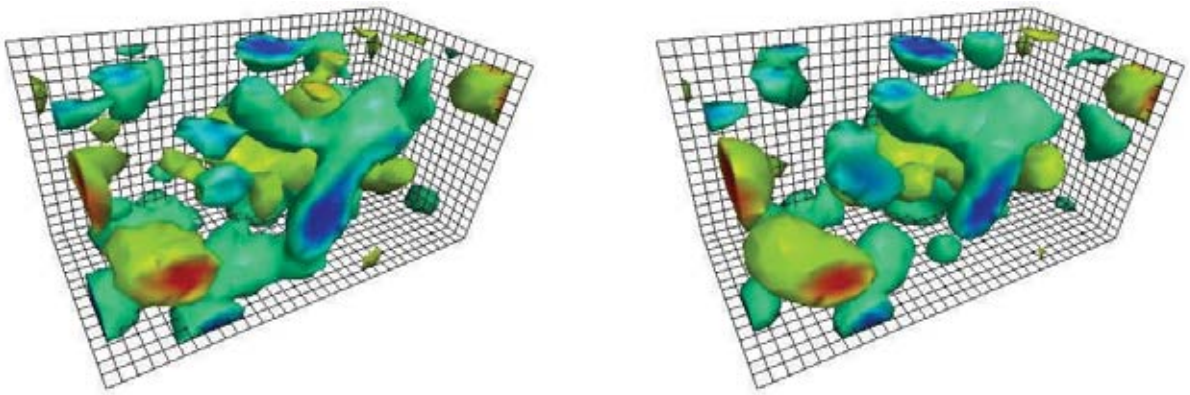

Figure 3.10: The fermionic topological charge density of a $Q = 0$ configuration with $\lambda_{cut} = 634$ MeV (left) compared with 48 sweeps of over-improved stout-link smearing (right). In colour: negative density blue/green, positive density red/yellow. In grey-scale: negative density dark, positive density light.

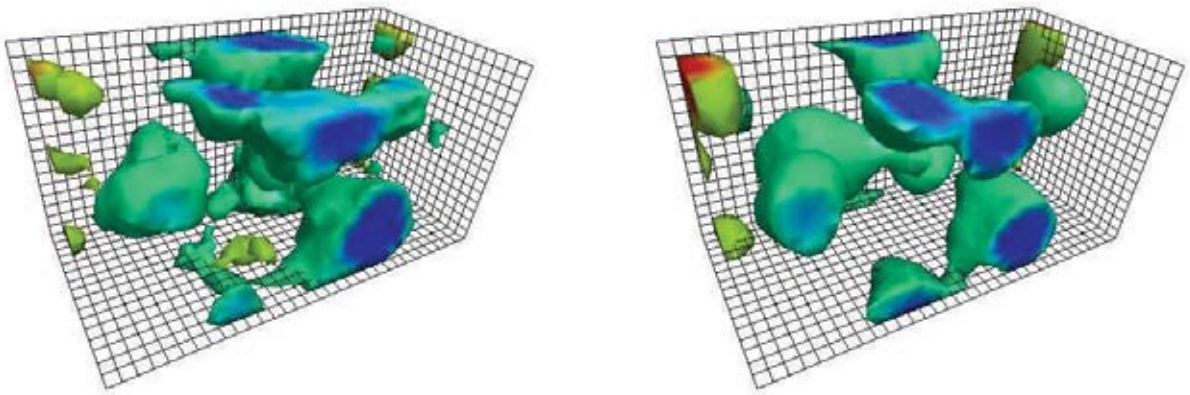

Figure 3.11: The fermionic topological charge density of a $Q = -8$ configuration with $\lambda_{cut} = 400$ MeV (left) compared with 103 sweeps of over-improved stout-link smearing (right). In colour: negative density blue/green, positive density red/yellow. In grey-scale: negative density dark, positive density light.

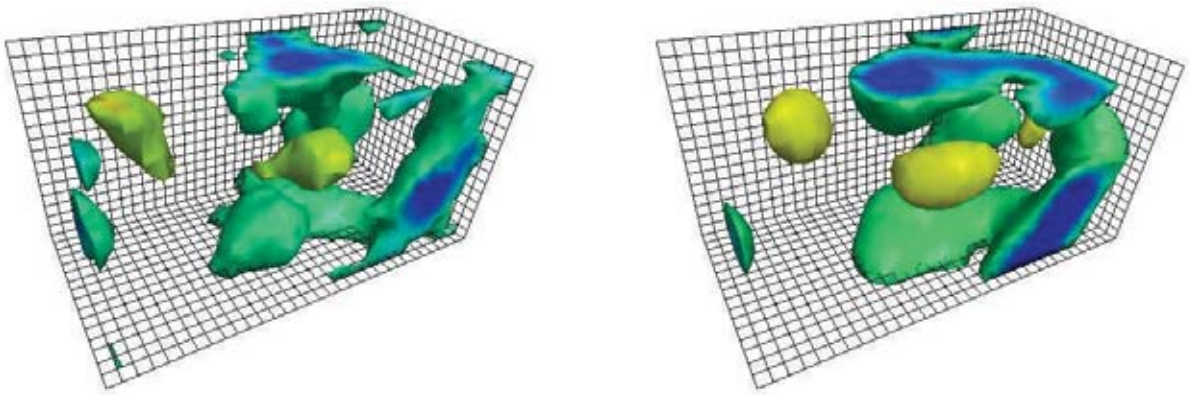

Figure 3.12: The fermionic topological charge density of a $Q = -7$ configuration with $\lambda_{cut} = 200$ MeV (left) compared with 192 sweeps of over-improved stout-link smearing (right). In colour: negative density blue/green, positive density red/yellow. In grey-scale: negative density dark, positive density light.

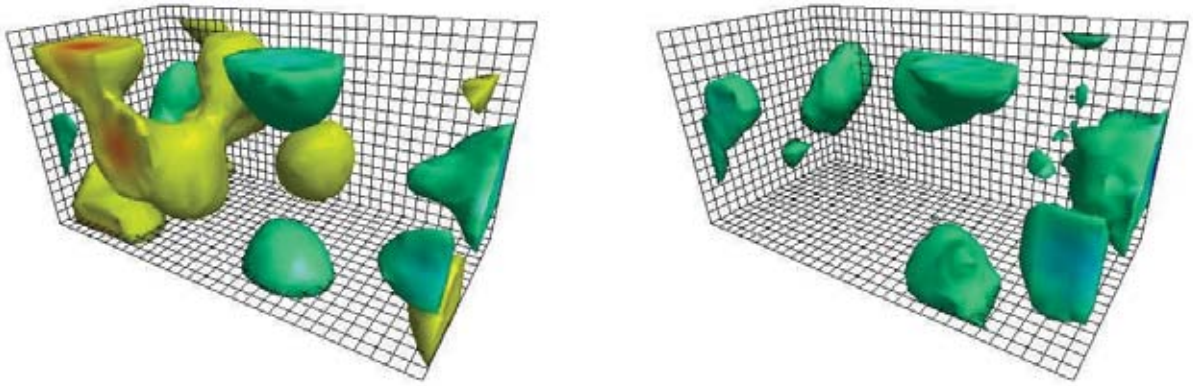

Figure 3.13: The gluonic topological charge density after 200 smearing sweeps (left) and the scalar density of the zero mode (right) for a $Q = -1$ configuration. One can see how the zero mode extends over only regions of negative charge. All extended sign-coherent objects seen are good local approximations to instantons or anti-instantons in the centre. In colour: negative density is blue/green, positive density is red/yellow (left), and scalar density is blue/green (right). In grey-scale: negative density dark, positive density light (left).

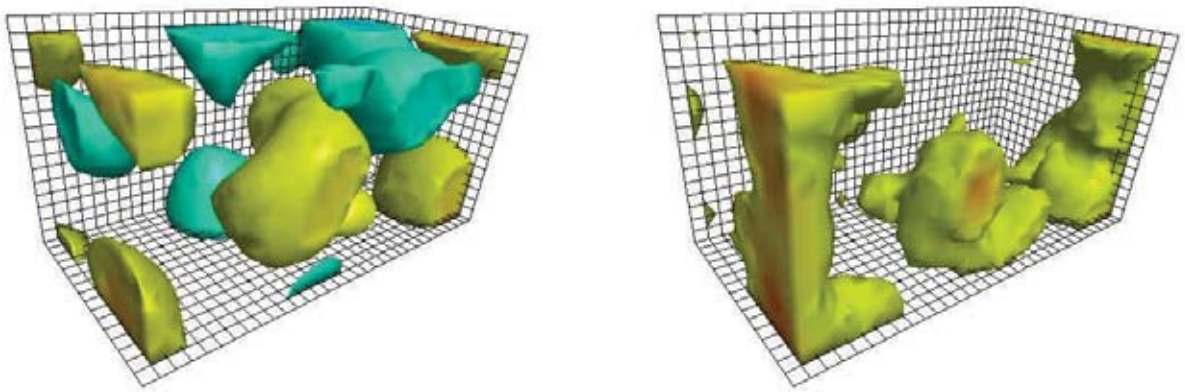

Figure 3.14: The gluonic topological charge density after 200 smearing sweeps (left) and the scalar density of the zero mode (right) for a $Q = 1$ configuration. In this case the high density regions of the zero mode are centred on lumps of positive charge. Again all objects are good approximations to classical instantons. In colour: negative density is blue/green, positive density is red/yellow (left), and scalar density is red/yellow (right). In grey-scale: negative density dark, positive density light (left).

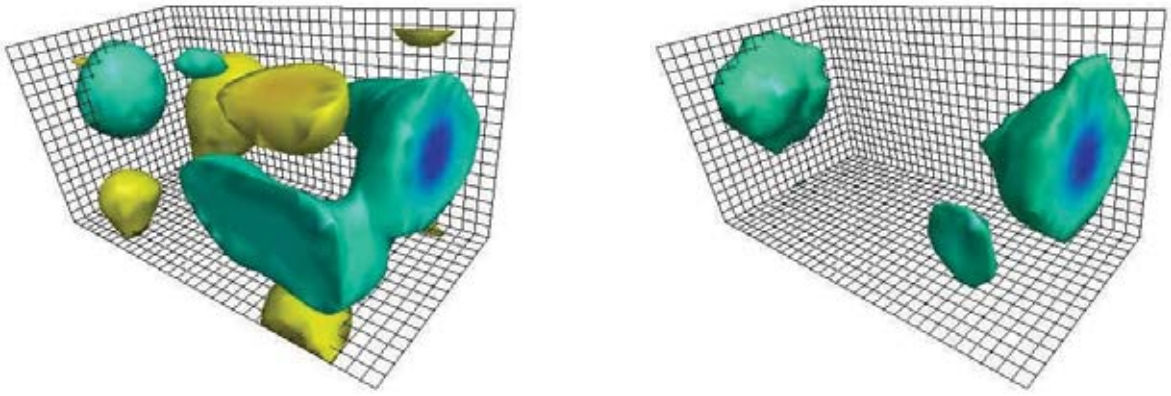

Figure 3.15: The gluonic topological charge density after 200 smearing sweeps (left) and the scalar density of the zero mode (right) for another $Q = -1$ configuration. The high density regions of the zero mode are again centred on lumps of negative charge. All topological objects are good approximations to classical instantons. In colour: negative density is blue/green, positive density is red/yellow (left), and scalar density is blue/green (right). In grey-scale: negative density dark, positive density light (left).

topological charge density for some clusters - even in a late stadium of smearing - may be built by non-zero modes. This leads us to revise the naive expectations according to which each zero mode would be residing on one lump of excess topological charge, for which a cluster charge of $Q_{cl} = \pm 1$ would be suggested by the instanton model. In fact, in Ref. [95] it has been demonstrated that the zero modes typically are simultaneously carried by a moderate number of centres below the peak density, before they start percolating throughout the whole lattice at an even lower level of the scalar density. Here we additionally learn that all theses centres are marked by lumps of topological charge of appropriate sign, however not necessarily all lumps are covered.

For these same three configurations we now consider the distribution of the lowest non-zero modes. Starting with the first $Q = -1$ configuration, we present the scalar and pseudoscalar densities of the first non-zero mode in Fig. 3.16. One sees that the pseudoscalar density, according to its local chirality, highlights certain parts of the topological lumps with appropriate sign of charge, and leaves others (for other low-lying modes).

The densities for the next two $Q = 1$ and $Q = -1$ configurations are shown in Figs. 3.17 and 3.18. In the instanton model, a whole band of almost-zero modes is generated by diagonalising the Dirac operator in the field of a superposition of n_+ instantons and n_- anti-instantons in the basis of linear combinations of the $n_+ + n_-$ zero modes corresponding to the case of infinite diluteness. Apart from the remaining $|Q|$ zero modes, the almost-zero modes are expected to bridge at least one pair of instanton and anti-instanton with the scalar density peaking on top of the topological charge lumps and the pseudoscalar density peaking with the appropriate sign there. Qualitatively, this is visible in Figs. 3.16, 3.17 and 3.18.

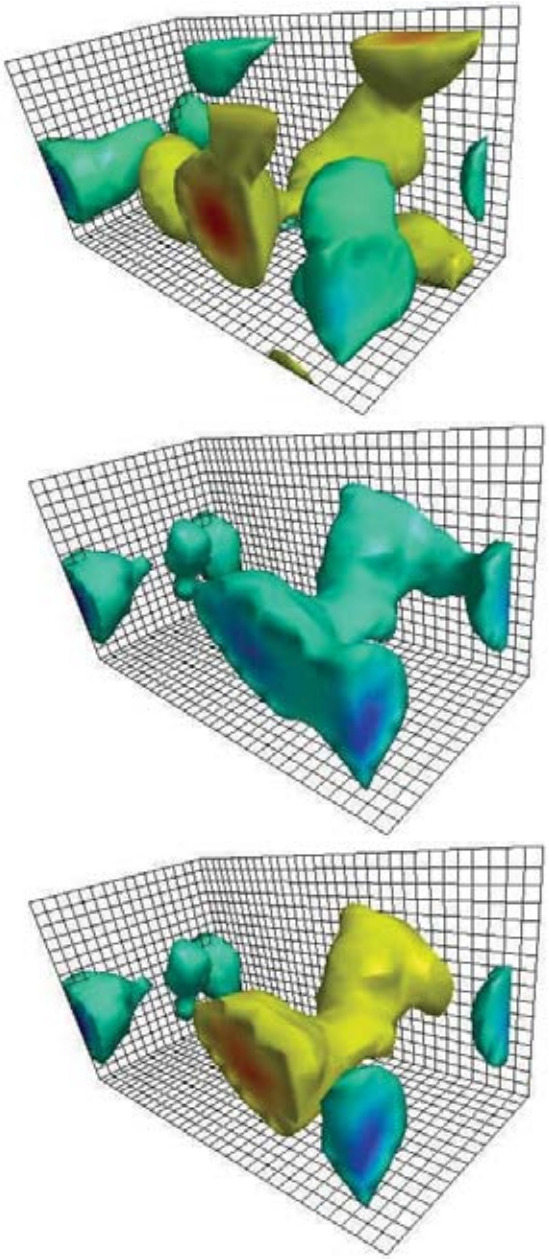

Figure 3.16: The scalar (middle) and pseudoscalar (bottom) density of the first non-zero mode for the $Q = -1$ configuration shown previously in Fig. 3.13, along with the gluonic topological charge density after 200 sweeps of smearing (top). One sees how the scalar density extends over objects of differing charge, but that the regions of alternate charge are realised by the local chirality of the pseudoscalar density. In colour: negative density is blue/green, positive density is red/yellow (top), positive chirality is blue/green and negative chirality is red/yellow (bottom). In grey-scale: negative density dark, positive density light (top), and positive chirality dark, negative chirality light (bottom).

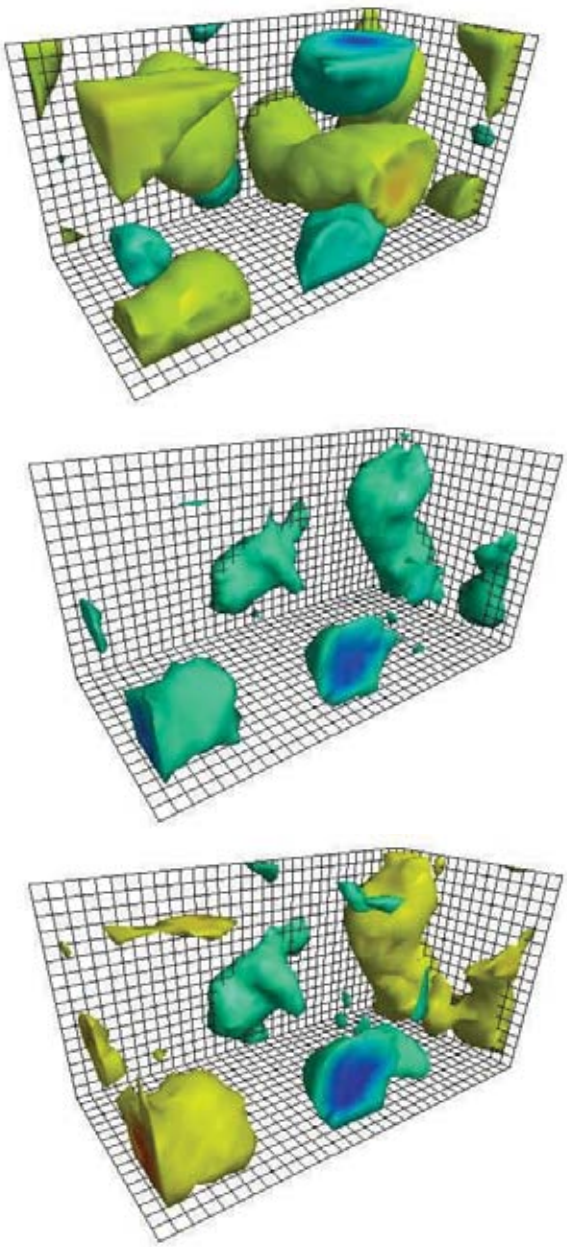

Figure 3.17: The scalar (middle) and pseudoscalar (bottom) density of the first non-zero mode for the $Q = 1$ configuration shown previously in Fig. 3.14, along with the gluonic topological charge density after 200 sweeps of smearing (top). Again, the scalar density extends over objects of differing charge, and the regions of alternate charge are revealed by the local chirality of the pseudoscalar density. In colour: negative density is blue/green, positive density is red/yellow (top), positive chirality is blue/green and negative chirality is red/yellow (bottom). In grey-scale: negative density dark, positive density light (top), and positive chirality dark, negative chirality light (bottom).

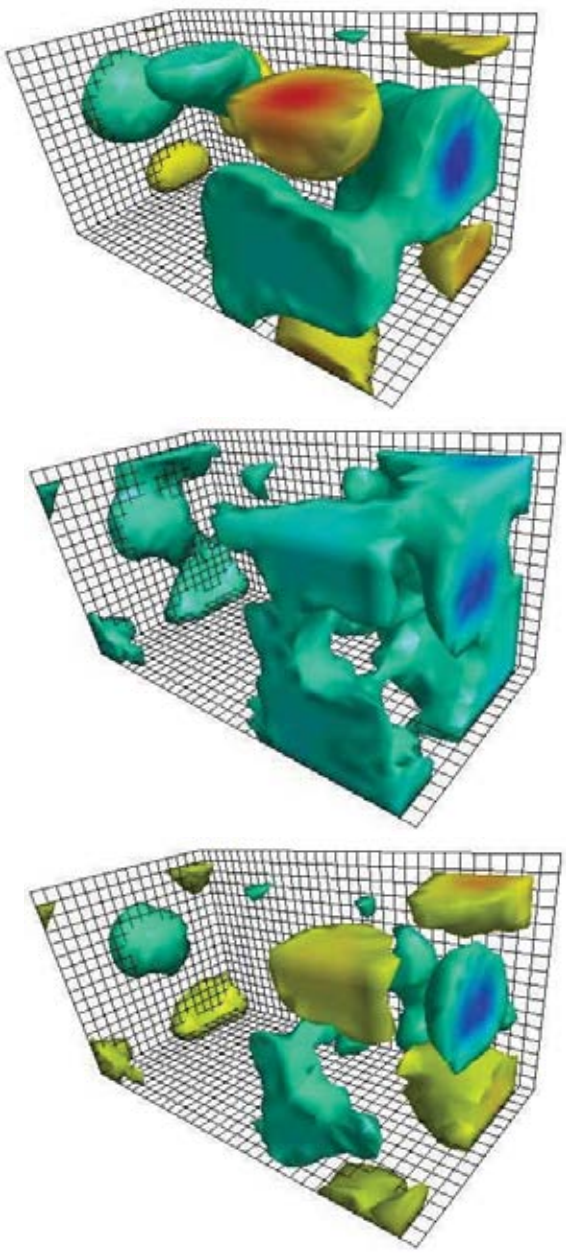

Figure 3.18: The scalar (middle) and pseudoscalar (bottom) density of the first non-zero mode for the $Q = -1$ configuration shown previously in Fig. 3.15, along with the gluonic topological charge density after 200 sweeps of smearing (top). Again, the scalar density extends over objects of differing charge, and the regions of alternate charge are revealed by the local chirality of the pseudoscalar density. In colour: negative density is blue/green, positive density is red/yellow (top), positive chirality is blue/green and negative chirality is red/yellow (bottom). In grey-scale: negative density dark, positive density light (top), and positive chirality dark, negative chirality light (bottom).

3.5 Summary

In this chapter we have confronted the overlap-fermionic topological charge density and the improved gluonic topological charge at different levels of ultraviolet smoothing, realised in one case by a truncation of the mode expansion at λ_{cut} and in the other case by a certain number of smearing steps applied to the gauge field in order to wipe out ultraviolet fluctuations. These two views of getting the infrared topological structure of the gauge field correspond to each other. A similar result, however for APE smearing and a different improved Dirac operator, was found in Refs. [100, 101]. In the present work this has been confirmed for two other specific realisations of both methods, using the massless overlap Dirac operator [85] on one hand and stout-link smearing with respect to an over-improved Symanzik type action [104] on the other. These two methods have their respective advantages compared to the approximate solution [98, 99] of the Ginsparg-Wilson relation and APE smearing [105].

We have made the comparison more complete and detailed, based first on the density-density two-point function and second on a point-by-point matching of the respective topological densities. The correspondence between the ultraviolet cutoff λ_{cut} of the overlap analysis and the number of smearing steps justifies the use of over-improved stout-link smearing, which is computationally less demanding, in the analysis of topological vacuum structure. This is particularly relevant for our investigation into the differences between the vacuum structure of quenched and non-quenched QCD in Chapter 5.

Chapter 4

Role of the Wilson-mass parameter on the overlap topological charge density

The content of this chapter is based on the paper: P. J. Moran, D. B. Leinweber and J. B. Zhang, in preparation*, (2010).*

In Chapter 2 we defined a new over-improved stout-link smearing algorithm. This was followed up with a detailed comparison between the topological charge densities from the overlap operator and the new smearing algorithm in Chapter 3. The results of that chapter demonstrated a strong correlation between the two approaches when the number of smearing sweeps was varied, however the negative Wilson-mass in the overlap Dirac operator was held fixed.

In this chapter the dependence of the overlap Dirac operator on the Wilson-mass regulator parameter is studied through calculations of the overlap topological charge densities at a variety of Wilson-mass values. In this formulation, the Wilson-mass is used in the negative mass region and acts as a regulator governing the scale at which the Dirac operator is sensitive to topological aspects of the gauge field. We observe a clear dependence on the value of the Wilson-mass and demonstrate how these values can be calibrated against a finite number of stout-link smearing sweeps.

The overlap topological charge density is also computed using a pre-smeared gauge field for the input kernel. Of interest here is whether applying the overlap operator will lead to further filtering of the gauge field. We demonstrate that this is indeed the case and calibrate the output against the over-improved stout-link smearing algorithm. The results suggest that the freedom typically associated with smearing algorithms, through the variable number of sweeps, also exists in the overlap operator, through the variable Wilson-mass parameter.

4.1 Introduction

Physical hadronic interactions observe an approximate chiral symmetry that is described by the theory of QCD, where in the massless limit, an exact chiral symmetry is realised.

Lattice QCD enables non-perturbative studies of the strong interaction from first principles, and ideally, should also observe this symmetry. Unfortunately, naive transcriptions of the continuum theory explicitly break chiral symmetry at finite lattice spacing a.

The Wilson Dirac operator [1],

$$D_W = \sum_\mu \left(\gamma_\mu \nabla_\mu - \frac{1}{2} r\, a\, \Delta_\mu + m \right) , \tag{4.1}$$

contains the irrelevant Wilson term, $r\,\Delta_\mu/2$, that explicitly breaks chiral symmetry at $\mathcal{O}(a)$ in order to remove fermion doublers. This lattice discretisation is often improved through the introduction of a clover term [15], however issues with chiral symmetry breaking still exist.

One technique that has recently been used to successfully reproduce the light hadron spectrum [106], is to filter the gauge links prior to applying the Dirac operator. These types of fermion actions are typically referred to UV-filtered or fat-link actions. The term "fat-link" comes from the smeared, *i.e.* fat, links that are used to construct the Dirac operator. One can smear either all links [26, 107–110], only the irrelevant terms [27, 28, 111, 112], or even just the relevant terms [113]. Incorporating at least some amount of UV-filtering has been shown to reduce the effects of chiral symmetry breaking [23, 26, 107, 111, 112, 114]. Unfortunately, there is no firm prescription for determining the correct amount of smearing to apply to the gauge background. One must find a balance between speeding up convergence of the Dirac operator, reducing chiral symmetry breaking effects, and removing short-distance physics from the gauge field. Of course, when using a fixed number of smearing sweeps n_{sw}, with a constant smearing parameter α, the smearing procedure only introduces irrelevant terms to the action. The fat-link action therefore remains in the same universality class of QCD. Nevertheless, this *freedom*, in the number of smearing sweeps that can be applied to the gauge field, can sometimes be regarded as a drawback to fat-link fermion actions.

The difficulties with implementing exact chiral symmetry on the lattice are summarised by the well known Nielsen-Ninomiya no-go theorem [115]. The no-go theorem forbids the existence of a local lattice Dirac operator, with exact chiral symmetry, and is free of doublers. A path around this block was provided in 1982 by Ginsparg and Wilson [29], who argued that the physical effects of chiral symmetry will be preserved if one can find a lattice Dirac operator, D, satisfying the Ginsparg-Wilson relation,

$$D\gamma_5 + \gamma_5 D = aDR\gamma_5 D\,, \tag{4.2}$$

where R is a local operator. Lüscher later showed [116] that any D, which is a solution of (4.2), obeys an exact chiral symmetry. A popular solution to the Ginsparg-Wilson relation is the Neuberger Dirac operator [30, 31],

$$D = \frac{m}{a}\left(1 + \frac{D_W(-m)}{\sqrt{D_W^\dagger(-m)\, D_W(-m)}} \right) , \tag{4.3}$$

which satisfies (4.2) with $R = 1/m$. Here we consider the standard choice of input kernel, $D_w(-m)$, the Wilson Dirac operator with a negative Wilson-mass term. To produce an

acceptable Dirac operator m must lie in the range $0 < m < 2$. For $m < 0$ there are no massless fermions, while for $m > 2$ doublers appear [87]. Varying the choice of m within the allowed range results in a flow of D-eigenvalues, and facilitates a scale-dependent fermionic probe of the gauge field [31]. Any value of m in the range $(0, 2)$ should yield the same continuum behaviour. However, simulations are performed at a finite lattice spacing a, and empirical studies prefer $m \gtrsim 0.9$ [117].

The overlap Dirac operator is extremely useful for studies of QCD vacuum structure because it satisfies the Atiyah-Singer index theorem, and will always give an exact integer topological charge. However, the value is not always unique and depends on the value of the Wilson-mass parameter [30, 117–119]. Studies of the topological susceptibility $\chi = \langle Q^2 \rangle / V$, have also observed this dependence [117, 120]. In particular, the study of Ref. [120] found that χ varied with m for small values of β, but that this dependence decreased as the continuum limit was approached.

In the following, we extend these previous studies to include an analysis of the topological charge density $q(x)$, $Q = \int d^4x \; q(x)$, as m is varied. A calculation of the topological charge density is a useful probe of the gauge field, due to its strong correlation with low-lying modes of the Dirac operator, as seen in Chapter 3. In recent years, the available compute resources and algorithm enhancements have reached a point where calculations of $q(x)$ using the overlap operator have become feasible [88, 89, 121].

4.2 Simulation details

Due to the high computational effort involved in a full calculation of the overlap topological charge density, we consider a single slice of representative $16^3 \times 32$ lattice configurations. The configurations were generated using a tadpole improved, plaquette plus rectangle (Lüscher-Weisz [80]) gauge action through the pseudo-heat-bath algorithm, with $\beta = 4.60$ giving a lattice spacing of $a = 0.093$ fm.

Five values of the Wilson-mass in the range $(1, 2)$ are used to calculate the overlap topological charge density,

$$q_{ov}(x) = -\mathrm{tr}\left(\gamma_5 \left(1 - \frac{a}{2\,m} D\right)\right) . \tag{4.4}$$

Results are reported in terms of the input parameter κ, which at tree level is related to m by

$$\kappa = \frac{1}{2\,(-m)\,a + 8\,r} , \tag{4.5}$$

with the standard choice $r = 1$. Note that the allowed range for κ is $1/8 < \kappa < 1/4$, and in the interacting theory renormalisation leads one to consider $1/6 \lesssim \kappa < 1/4$. A single calculation of $q_{ov}(x)$ for one time-slice will contain $16^2 \times 32 = 8192$ sites of information that must be analysed, and this most easily achieved through direct visualisations. In all figures, we represent regions of positive topological charge density by the colour red fading to yellow, for large to small $q_{ov}(x)$ respectively. Similarly, regions of negative topological charge are coloured blue fading to green. A cutoff is applied to the topological charge density, below which no charge is rendered. This allows one to observe the underlying structure of the field.

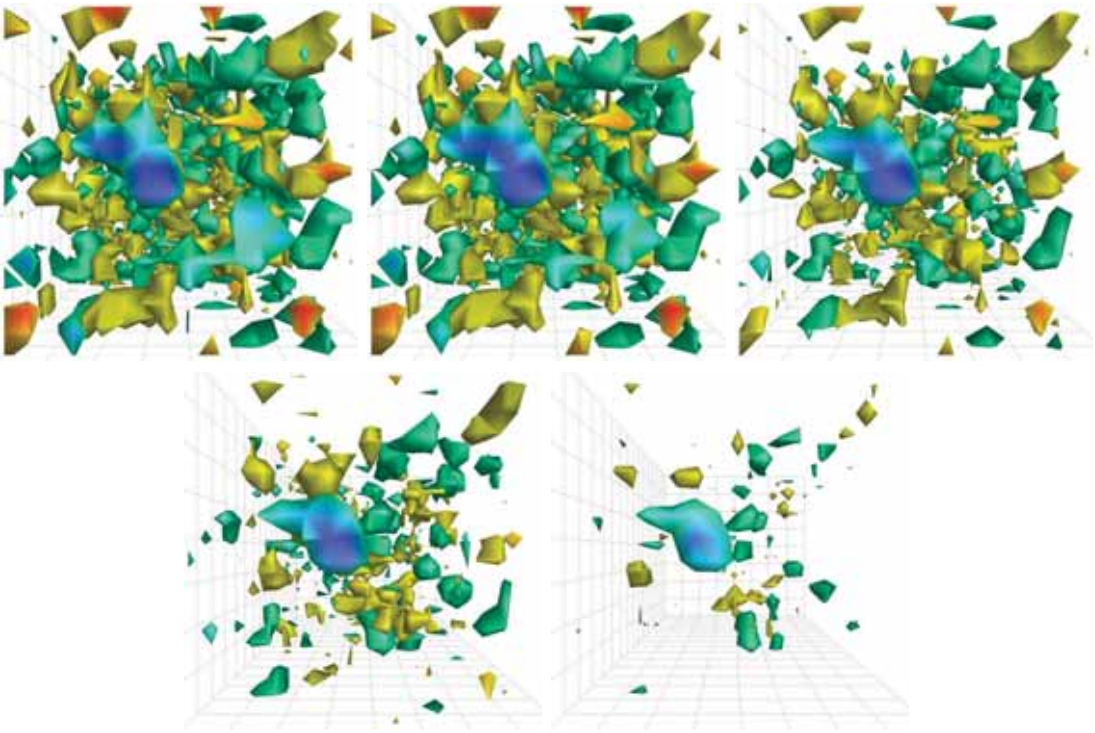

Figure 4.1: The overlap topological charge density $q_{ov}(x)$ calculated with five choices for the Wilson hopping parameter, κ. From left to right, we have $\kappa = 0.23$, 0.21, and 0.19 on the first row, with 0.18, and 0.17 on the second. There is a clear dependence on the value of κ used, with larger values revealing a greater amount of topological charge density.

4.3 Dependence on the Wilson-mass parameter

The topological charge densities, for the five choices of κ, are presented in Fig. 4.1. A clear dependence on κ is apparent from the figures, with larger values of κ revealing greater amounts of topological charge. This is consistent with expectations since as κ is increased the Dirac operator becomes more sensitive to smaller topological objects. When using smaller values of κ these objects will not be felt by the Dirac operator.

The removal of nontrivial topological objects as κ is decreased, bears a striking resemblance to the well tested cooling [64–66, 74, 119, 122] and smearing [67–71] algorithms introduced in Chapter 2. In these procedures, the links on the lattice are systematically updated such that the gauge field is driven towards a more classical state. This results in a removal of topological charge density, as the action is decreased. We now extend the work of Chapter 3 in which a strong correlation was observed between the UV-filtered overlap topological charge density, and the gluonic definition resolved with an over-improved stout-link smearing algorithm.

For the over-improvement parameter we continue to use a value of $\epsilon = -0.25$, however for the smearing parameter of Eq. (2.25) we select a relatively weak value of $\rho = 0.01$. This should be compared with the maximum value possible for this combination of plaquettes and rectangles, $\rho \approx 0.06$ and the standard stout-link smearing value of 0.1. After smearing, the gluonic topological charge density can be calculated by recalling that,

$$q_{sm}(x) = \frac{g^2}{32\,\pi^2}\epsilon_{\mu\nu\rho\sigma}F^{ab}_{\mu\nu}(x)\,F^{ba}_{\rho\sigma}(x)\,. \tag{4.6}$$

In comparing the two definitions for the topological charge density we apply a multiplicative renormalisation to the gluonic $q_{sm}(x)$,

$$q_{sm}(x) \to Z\,q_{sm}(x)\,. \tag{4.7}$$

The renormalisation factor is chosen such that the *structure* of the two field densities can be best compared. The best match to the overlap $q_{ov}(x)$ is then found by calculating,

$$\min\ \sum_x \left(q_{ov}(x) - Z\,q_{sm}(x)\right)^2\ , \tag{4.8}$$

as the number of smearing sweeps is varied. For this work, two methods for calculating Z are considered;

- $Z_{\rm calc} \equiv \sum_x |q_{ov}(x)|\ /\ \sum_x |q_{sm}(x)|\,,$
- $Z_{\rm fit}$, where the renormalisation factor is calculated such that (4.8) is minimised.

We also compare with an alternative matching procedure [100, 123] in which one calculates,

$$\Xi_{AB} = \frac{\chi^2_{AB}}{\chi_{AA}\,\chi_{BB}}\,, \tag{4.9}$$

with

$$\chi_{AB} = (1/V)\sum_x \left(q_A(x) - \bar{q}_A\right)\left(q_B(x) - \bar{q}_B\right)\ , \tag{4.10}$$

κ	n_{sw}	Z_{calc}	n_{sw}	Z_{fit}	n_{sw}	Ξ_{AB}
0.17	28	0.56	29	0.47	29	0.76
0.18	26	0.70	27	0.61	27	0.78
0.19	25	0.82	25	0.68	25	0.77
0.21	23	0.91	23	0.76	23	0.75
0.23	22	0.89	23	0.76	23	0.73

Table 4.1: The number of smearing sweeps, n_{sw}, needed to match the overlap topological charge density calculated with the listed value of κ. The three methods used to find the best match are detailed in the text.

where $\bar{q}$ denotes the mean value of $q(x)$, and in our case $q_A(x) \equiv q_{ov(x)}$, $q_B(x) \equiv q_{sm}(x)$. Here the best match is found when Ξ_{AB} is nearest 1. In this case, the ratio eliminates any dependence on the renormalisation factor, Z.

We first consider Z_{calc}. The overlap topological charge densities, along with the corresponding best matches, for three choices of κ are shown in Fig. 4.2. We see that as κ is decreased, and non-trivial topological charge fluctuations are removed, a greater number of smearing sweeps are needed in order to recreate the topological charge density. Again this agrees with expectations since the overlap operator becomes less sensitive to small objects as κ is decreased, and it is these objects that are removed by the smearing algorithm. Comparing the different definitions in Fig. 4.2 shows good agreement in the topological structures revealed.

The three different methods for calculating the renormalisation constant are compared in Table 4.1. As we move down the table there is a monotonically increasing trend in the number of sweeps required to match the value of κ. We note that despite some minor variation in n_{sw}, it is possible to correlate the number of sweeps to the value of the Wilson hopping parameter. We note that the average renormalisation factor $\bar{Z} \sim 0.7$, reflecting the fact that with $\rho = 0.01$ the gauge fields remain rough after ~ 25 sweeps of smearing.

4.4 UV-filtered overlap

Let us now consider the effect of evaluating the overlap operator on a pre-smeared gauge field. This is of some relevance to UV-filtered overlap actions [24, 114, 124, 125], in which all links of a gauge field are smeared prior to applying the overlap operator. As already seen in Fig. 4.2, applying the overlap operator is in some respects similar to smearing the gauge field. Of interest here is whether the overlap operator, acting on a smeared gauge field, will reveal a topological charge density close to the input smeared gauge field, or whether further smearing will be needed to match the calculated $q_{ov}(x)$.

To make comparisons clear, we denote the overlap topological charge density, calculated using a smeared configuration as input, by $q_{ov}^{\text{UV}}(x)$. We consider the third Wilson-mass, where $\kappa = 0.19$ and the best smeared match was provided by $n_{sw} = 25$. Figure 4.3 shows the original $q_{ov}(x)$ along with the new UV-filtered $q_{ov}^{\text{UV}}(x)$. Far less topological charge density is observed in the pre-filtered case. Given the previous results, it is clear

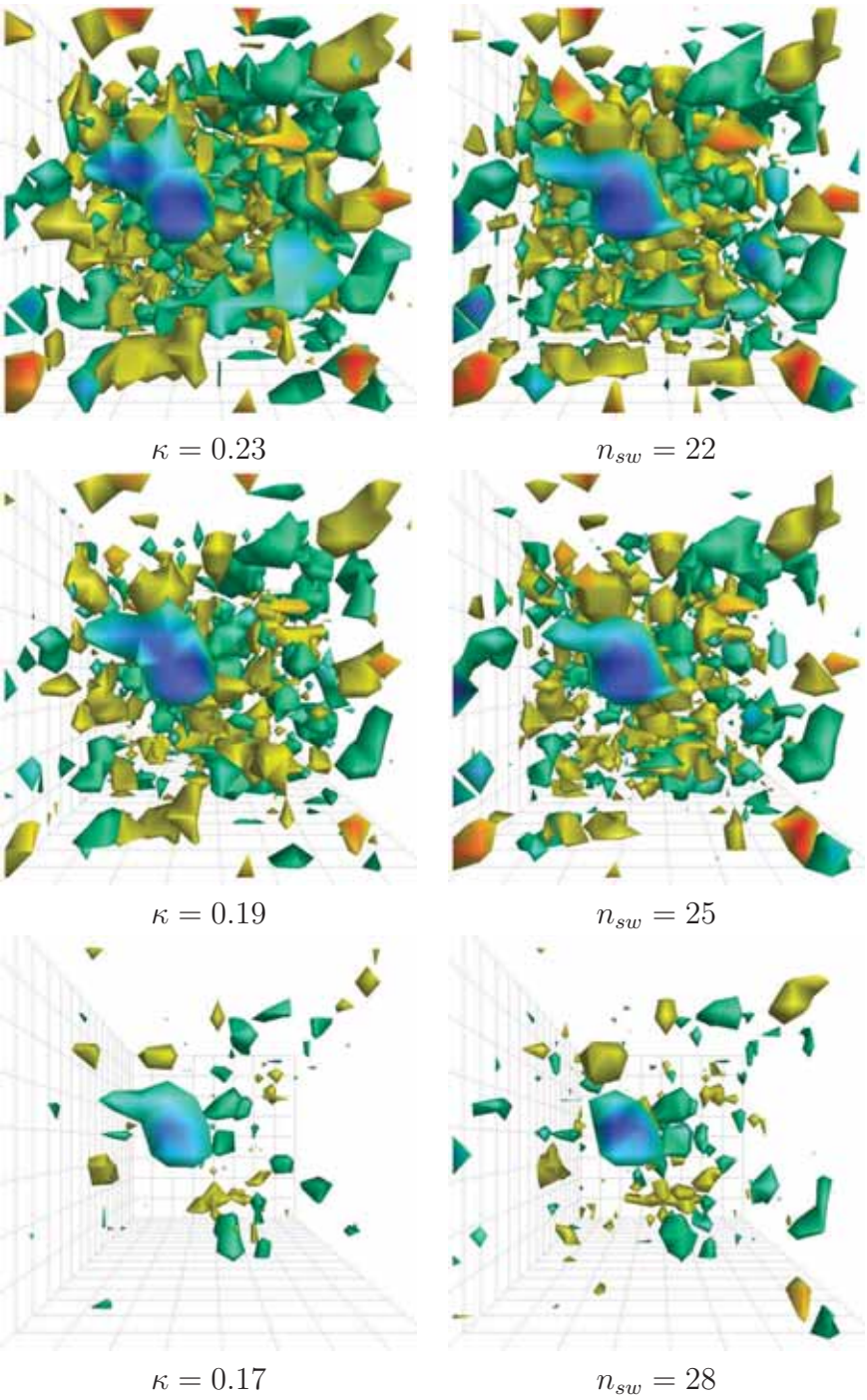

Figure 4.2: The best smeared matches (right) compared with the overlap topological charge densities (left) in order of decreasing κ, where $q_{sm}(x)$ is renormalised using Z_{calc}. There is a clear relationship between κ and n_{sw}, with smaller κ values requiring a greater number of smearing sweeps to reproduce the topological charge density.

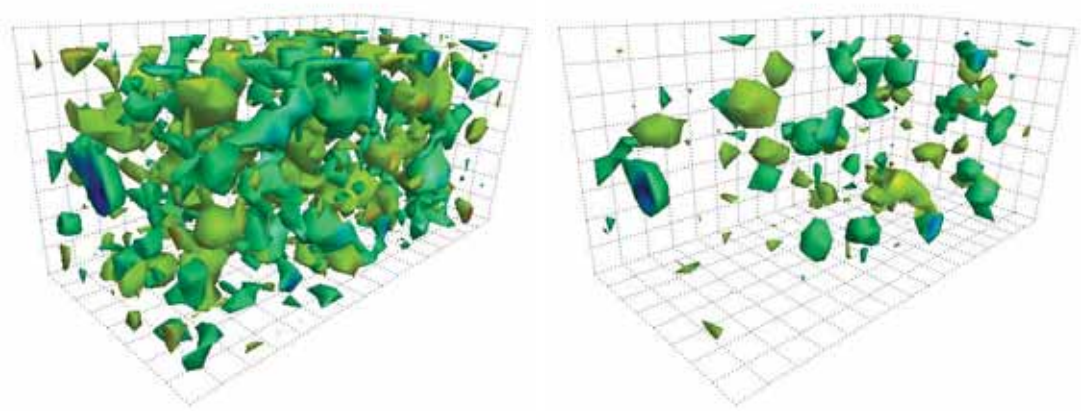

Figure 4.3: A comparison of the overlap topological charge density $q_{ov}(x)$ computed using $\kappa = 0.19$, with $q_{ov}^{\mathrm{UV}}(x)$ calculated using the same κ, on the same configuration, after first applying 25 sweeps of smearing.

that a far greater number of smearing sweeps will be required to reproduce $q(x)$ using the gluonic definitions.

Repeating the same calculation as before we find that 45 sweeps of over-improved stout-link smearing provides the best match to the overlap topological charge density. A comparison between $q_{ov}^{\mathrm{UV}}(x)$ and the smeared $q_{sm}(x)$ is shown in Fig. 4.4, where $Z_{\mathrm{calc}} = 0.85$. This is approximately double the original 25 sweeps required to match the overlap topological charge density, once again revealing the smoothing aspect of the overlap operator. These results indicate that the filtering that occurs in the overlap operator is independent of the input gauge field.

4.5 Summary

Using direct visualisations of the topological charge density, we have analysed the dependence of the overlap Dirac operator on the Wilson-mass regulator parameter m. Systematic differences appear in the topological structure of the gauge field as m is varied. By comparing $q_{ov}(x)$ with the gluonic definition of the topological charge density, resolved with a topologically stable smearing algorithm, a direct correlation between m and the number of sweeps is revealed. Smaller values of κ reveals topological charge densities that are similar to using a greater number of smearing sweeps.

From these observations, one can conclude that the "smoothness" of the gauge field, as seen by the overlap operator depends, on the value of the Wilson-mass. This is similar to fat-link fermion actions in which the smoothness is directly dependent upon the number of applied smearing sweeps. These results indicate that the freedom typically associated with fat-link fermion actions, through the number of smearing sweeps, is also present in the overlap formalism, through the freedom in the Wilson-mass parameter.

We also considered the application of the overlap operator to a smeared gauge field, which is of relevance to UV-filtered overlap actions. We demonstrated that, regardless

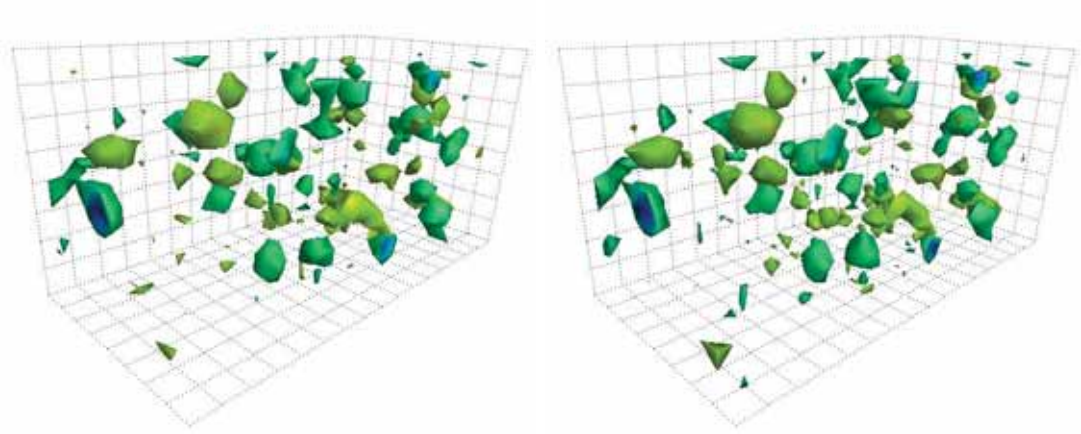

Figure 4.4: The overlap charge density calculated on a configuration filtered by 25 of stout-link smearing sweeps, compared with $q_{sm}(x)$ after 45 sweeps of smearing. There is a strong correlation between the objects observed. It appears as though the overlap operator has again "smoothed" the configuration.

of the input gauge field to the overlap operator, UV-filtering still occurs via the overlap operator. The strength of the filtering is of a comparable strength to that of the overlap acting on a hot, unfiltered configuration. When creating a UV-filtered overlap action, one must therefore take care to preserve the short-distance physics of the gauge field.

Chapter 5

QCD vacuum structure and the impact of dynamical quarks

The content of this chapter is based on the publications: P. J. Moran and D. B. Leinweber, Phys. Rev. *D 78, 054506 (2008) [arXiv:0801.2016 [hep-lat]].* and *P. J. Moran and D. B. Leinweber, To appear in the proceedings of QCD Downunder II, Massey University, Albany, New Zealand 17 - 19 January 2008 [arXiv:0805.4246 [hep-lat]].*

Following the extensive investigations into lattice topology in the previous chapters, we are now in a position to perform an accurate study of QCD vacuum structure. We begin in Sec. 5.1 with a discussion of the dominant features of QCD vacuum structure at different scales. At short distances the vacuum is dominated by a sign-alternating sheet-like structure, whilst at larger distances an instanton-like picture dominates. With the introduction of a new Gaussian smoothing operator we demonstrate how the different views of the QCD vacuum at short and long distance scales are compatible. Both should be considered in studies of QCD topology.

In Sec. 5.2 we proceed to study the effects of dynamical quarks on QCD vacuum structure using the over-improved stout-link smearing of Chapter 2. The work presented in previous chapters justifies this choice of algorithm. At short distances we find that the magnitudes of the negative dip in the $\langle q(x)q(0)\rangle$ correlator and the positive $\langle q(0)^2\rangle$ contact term are both increased with the introduction of dynamical fermion degrees of freedom. At large scales we examine the extent to which instanton-like objects are found on the lattice, and how their distributions vary between quenched and dynamical gauge fields. We show that dynamical gauge fields contain more instanton-like objects with an average size greater than in the quenched vacuum and explain the physics generating these phenomena. Finally, we directly visualise the topological charge density in order to investigate the effects of dynamical sea-quark degrees of freedom on topology.

5.1 QCD vacuum structure at different scales

5.1.1 Short distance structure

It is argued [94, 126] that the predominant feature of the QCD vacuum at short-distance scales is described in the Euclidean two-point function for the topological charge density

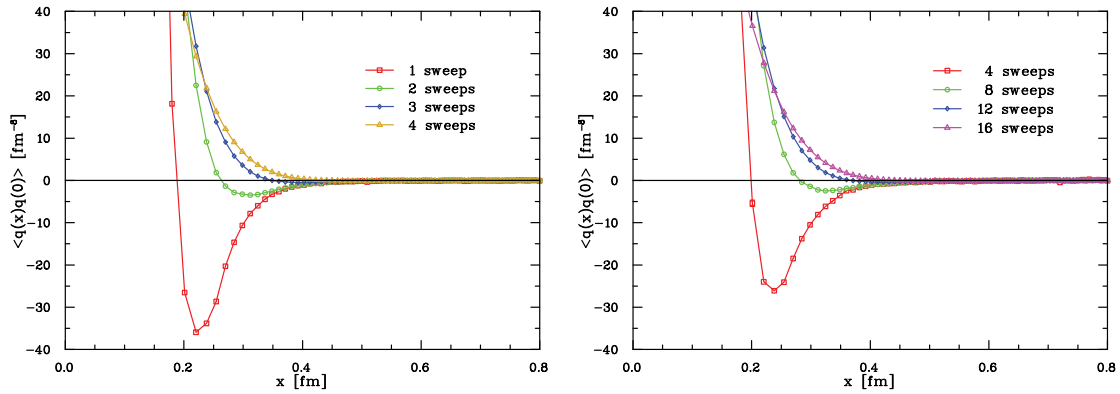

Figure 5.1: The topological charge density correlator $\langle q(x)q(0)\rangle$ as computed on the quenched MILC gauge configurations for both 3-loop improved cooling (left) and over-improved stout-link smearing (right). We see that for a small number of sweeps it is possible to obtain a negative $\langle q(x)q(0)\rangle$ correlator, similar to the overlap results [129]. Note that errors were calculated using a first-order jackknife procedure but are too small to see.

$q(x)$,

$$\langle qq\rangle \equiv \langle q(x)q(0)\rangle\,, \tag{5.1}$$

also referred to as the topological charge density correlator. Seiler and Stamatescu [127, 128] were the first to show that this two-point function should be negative, in the Euclidean gauge, for any $x > 0$. This property arises from reflection positivity and Ref. [129] provides a recent discussion.

Despite the long history of cooling and smearing algorithms, this negative behaviour was first observed using the overlap operator [129]. Due to the filtering of short distance fluctuations, it wasn't known whether a similar correlator could be realised using either cooling or smearing. Unfortunately, the overlap operator is very computationally intensive, and prohibits high statistics studies of QCD vacuum structure.

As we have already seen in Chapter 3, by using a variable number of smearing sweeps it is possible to realise the negative behaviour of the $\langle qq\rangle$ correlator using traditional approaches. We first observed this in Ref. [104] using both cooling and over-improved smearing. For reference the results are provided here in Fig. 5.1, where we analyse the dependence of the two-point function on the number of applied cooling and smearing sweeps.

This negative behaviour of the $\langle qq\rangle$ correlator suggests a sign-alternating sheet-like topological structure exists in the QCD vacuum [94, 126]. Using five-sweeps of over-improved smearing we can directly observe this structure using visualisations of the topological charge density. In Fig. 5.2 we present two such visualisations. In the left graphic we have plotted the full range of topological charge density, including values approaching zero, with negative charge coloured green to blue and positive charge yellow to red. This approach reveals the proposed sheet-like structure of the vacuum [94]. In the right graphic we render only the negative charge, colouring from light to dark the regions of weakest to strongest charge. This approach serves to illustrates the structure

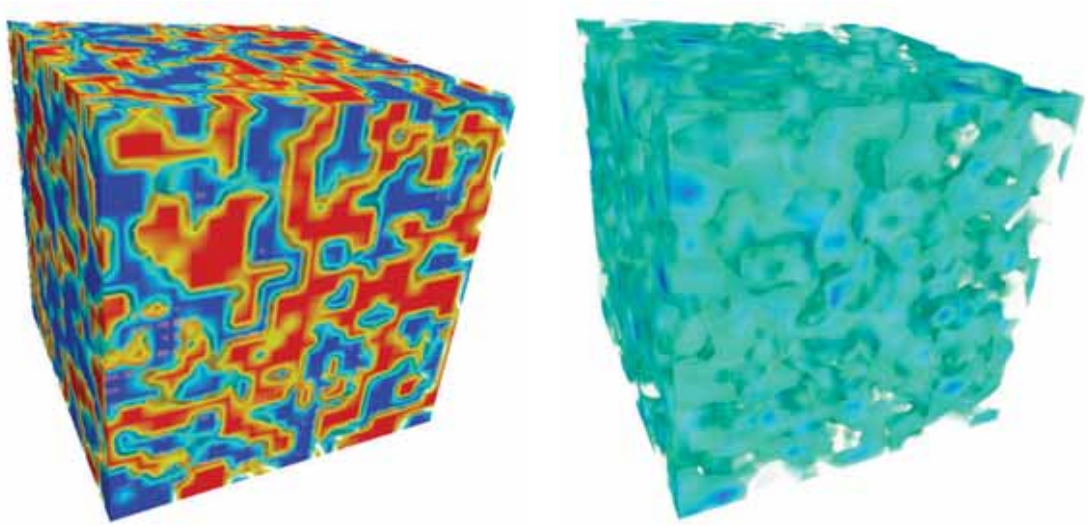

Figure 5.2: [left] The short-distance sheet structure of the vacuum is clearly apparent after five sweeps of over-improved stout-link smearing. Negative charge density is green to blue, and positive charge density is yellow to red. [right] The same data, this time with the positive charge removed and the magnitude of the negative charge shown through the strength of the blue colouring.

that still exists within the sheets. Raising the cutoff threshold for $q(x)$ so that only the most intense regions of charge are shown presents a different view of the vacuum, as seen in the left graphic of Fig. 5.3. Here the vacuum appears to have a granular, sand-like structure. Ilgenfritz has investigated this idea of clustering deeply [89].

5.1.2 Long distance structure

The right plot of Fig. 5.3 shows the topological charge density after 45 sweeps of over-improved stout-link smearing, where we see the familiar lava lamp structure appear. This long-distance, infrared structure is believed to be dominated by instanton-like objects and has been the focus of vacuum structure studies over the past few decades.

The presence of possible instanton-like objects in the vacuum can be measured using the classical instanton solution. By using over-improved stout-link smearing we are able to extract both the action and charge densities of our gauge fields. Starting with the action density we locate the positions of all local maxima in the field. The local maxima are identified by finding a point at the centre of a 3^4 hypercube whose action density exceeds that of the neighbouring 80 points of the hypercube.

Taking each maxima to be the approximate centre of a possible instanton-like object we fit the classical instanton action density

$$S_0(x) = \xi \frac{6}{\pi^2} \frac{\rho_{\text{inst}}^4}{\left((x - x_0)^2 + \rho_{\text{inst}}^2\right)^4}, \tag{5.2}$$

to the measured action density. An arbitrary scale factor, ξ, is included to allow the *shape* of the action density to determine the size, ρ_{inst}. We fit the six parameters ξ,

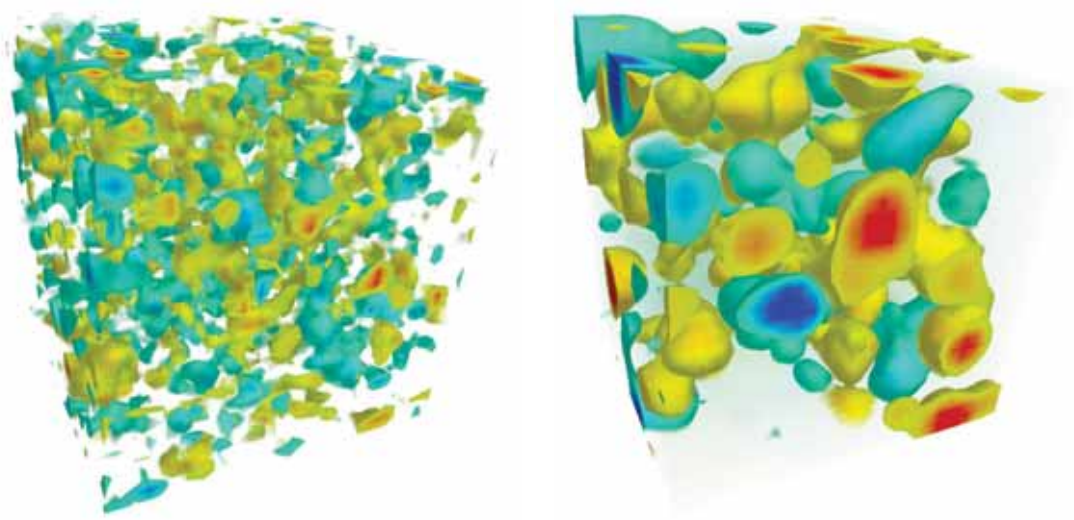

Figure 5.3: [left] Placing a high cutoff on $q(x)$ such that only the most intense regions of charge are seen presents a picture of the QCD vacuum which resembles the sand of one of Australia's many fine beaches. The grains of sand will diminish in size as the continuum limit is approached. [right] The topological charge after 45 sweeps of over-improved stout-link smearing.

ρ_{inst}, and the four components of x_0 by fitting Eq. (5.2) to the action density of the aforementioned 3^4 hypercube.

From ρ_{inst} one can infer the topological charge to be observed at the centre of the distribution $q(x_0)$ if it truly is an instanton

$$q(x_0) = Q\frac{6}{\pi^2\rho_{\text{inst}}^4}\,. \tag{5.3}$$

Here $Q = \pm 1$ for an instanton/anti-instanton. This can then be compared with the topological charge measured directly from the charge density observed on the lattice.

A calculation of $q(x_0)$ on the sample MILC gauge configuration is provided in Fig. 5.4. With the exception of only two outliers, the maxima are good local approximations to the classical instanton solution. These results are strongly in favour of an instanton dominated model of the QCD vacuum.

5.1.3 Bridging the gap

It is not is obvious how, or to what extent, the instanton-like representation of the vacuum should coexist with the sheet-like structure. In order to make some comparisons between the two different sheet and lava pictures of the QCD vacuum we require some method of averaging the short-distance structure of Fig. 5.2, independent of the smearing procedure. For this, we define a Gaussian smoothing operation to act on the topological charge density itself. Given $q(x)$ for some gauge field, each point on the lattice is simultaneously updated according to,

$$q(x_0) = \frac{1}{2\pi\sigma^2}\sum_x e^{-r^2/2\sigma^2} q(x)\,, \tag{5.4}$$

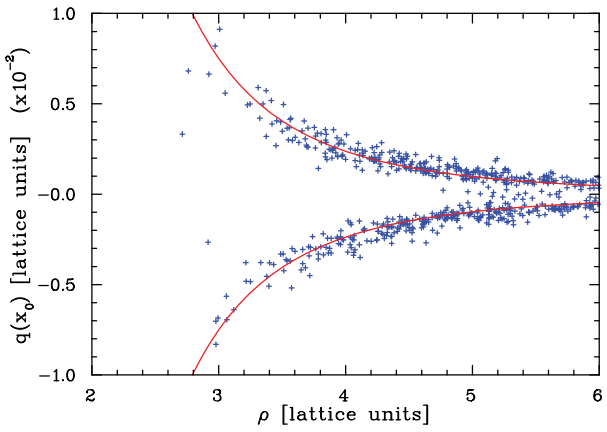

Figure 5.4: Comparison of the calculated $q(x_0)$ after 45 sweeps of smearing with the exact instanton solution. After 45 sweeps of smearing the majority of topological objects are relatively good approximations to instantons at their cores.

where r is the Euclidean distance between x and x_0, and σ is the standard deviation of the Gaussian distribution in lattice units.

The evolution of the topological charge density of Fig. 5.2 under Gaussian smoothing with increasing σ is shown in Fig. 5.5. The resulting effect appears to be quite similar to that seen in the well known cooling and smearing animations. In Fig. 5.6 we provide a side by side comparison of the Gaussian smoothed charge density with $\sigma = 1.75$ and the topological charge density obtained after 45 sweeps of smearing. Recall that the Gaussian smoothed charge density was generated from the topological charge density after only five smearing sweeps. Although the resulting densities are certainly not identical, they still share many common features.

These results suggest that the QCD vacuum consists of a sandwich of high-energy fluctuations, with a long-distance structure hidden beneath. This kind of idea has been discussed previously by P. de Forcrand [130], and is represented graphically in Fig. 5.7. We argue that the two representations are complementary and should both we considered in studies of QCD vacuum structure.

5.2 The impact of dynamical quarks on QCD vacuum structure

We now investigate the structure of the dynamical QCD vacuum on both short and long distance scales using over-improved stout-link smearing. The stability of instanton-like objects under over-improved stout-link smearing, as we saw in Chapter 2, allows us to achieve the most accurate determination of instanton size distributions to date.

In addition, the work presented in Chapter 3 has demonstrated the strong correlation between over-improved stout-link smearing and the truncated overlap Dirac operator. To good accuracy, the UV-cutoff in the Dirac operator is directly related to the number of over-improved stout-link smearing sweeps. However, the overlap Dirac operator is computationally expensive and not suited for high-statistics studies on large dynamical

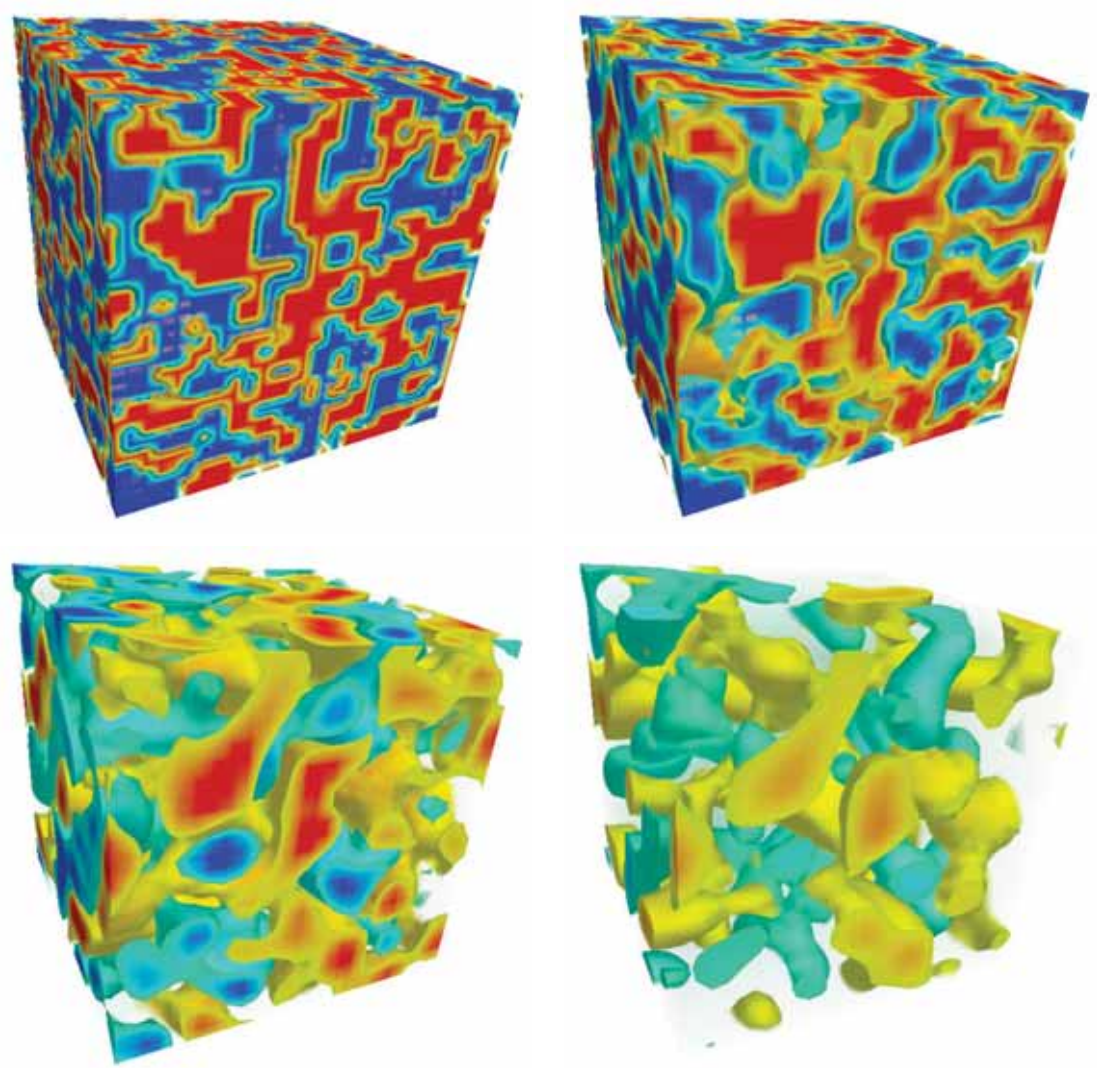

Figure 5.5: The evolution of $q(x)$ obtained from five sweeps of over-improved stout-link smearing under Gaussian smoothing. The values of σ used were 0.25 [top-left], 0.75 [top-right], 1.25 [bottom-left], and 1.75 [bottom-right].

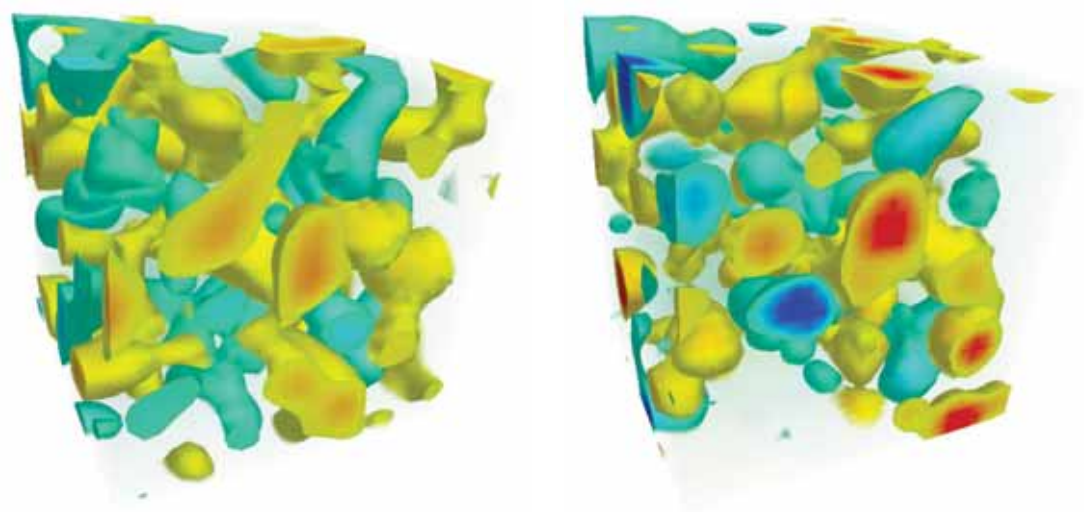

Figure 5.6: [left] The Gaussian smoothed topological charge density after five smearing sweeps, using $\sigma = 1.75$. [right] The topological charge density after 45 smearing sweeps. While the two pictures are not identical, it is remarkable that several common features are present.

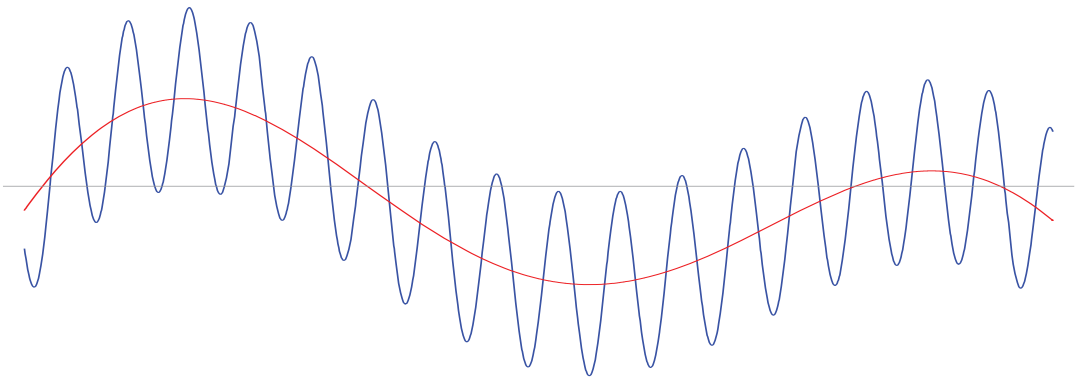

Figure 5.7: An example of how UV fluctuations could be superimposed on a deeper long-range structure, as suggested by P. de Forcrand [130].

gauge fields. Over-improved stout-link smearing therefore provides the most accurate technique for studying both quenched and dynamical gauge fields with statistics sufficient to reveal differences in the vacuum structure.

As discussed in Sect. 5.1, at short distance scales one studies the topological charge density correlator, the integrand of the topological susceptibility,

$$\chi \equiv \frac{\langle Q^2 \rangle}{V} = \int d^4x \, \langle q(x) q(0) \rangle \, , \tag{5.5}$$

where V is the 4-volume. Recent overlap results [89, 129] have detailed the strong negative behaviour of the 2-point function in quenched gauge fields. In Chapter 3 we demonstrated how it is also possible to generate a strong negative correlator using five sweeps of over-improved stout-link smearing.

However, these studies have so far all been on quenched gauge fields. There have been no studies of the differences between quenched and dynamical fields in the short-distance correlator[1]. This work will address this issue with a high-statistics study on several accurately matched large volume lattices from MILC [76, 77] using the accurate over-improved stout-link smearing algorithm.

After examining the short-distance structure of the correlator and the role of dynamical fermion degrees of freedom, we probe the infrared structure of the full dynamical QCD vacuum. In Sec. 5.2.3 the effect of the extra degrees of freedom on instanton distributions is studied. Finally, in Sec. 5.2.4 we directly visualise the topological charge density in order to investigate the effects of dynamical sea-quark degrees of freedom on topology. Results are summarised in Sec. 5.3.

5.2.1 Simulation details

This work uses the suggested over-improvement parameter $\epsilon = -0.25$, and the standard smearing parameter $\rho_{\rm sm} = 0.06$. Please refer to Chapter 2 for details of the over-improved stout-link smearing algorithm.

The gauge fields for this study were generated by the MILC collaboration [76, 77] using a Tadpole and Symanzik improved gauge action with $1 \times 1 + 1 \times 2 + 1 \times 1 \times 1$ terms in the quenched case and an Asqtad staggered dynamical fermion action for the $2+1$ flavors of dynamical quarks. The lattice spacing for all three types of gauge fields is $a = 0.086$ fm. For the specifics of how the gauge fields were generated see Refs. [76, 77]. Simulation parameters are summarised in Table 5.1.

5.2.2 Topological charge density correlator

As has been discussed extensively, the $\langle qq \rangle$ correlator is negative for any $x > 0$ [127, 128]. Given that the correlator must have a positive contact term $\langle q^2(0) \rangle_x$, the correlator

[1] We note the early investigation of the dynamical 2-point function by Hasenfratz [105] on small lattices where 30 sweeps of unimproved APE smearing [69] was applied. This level of smoothing is sufficient to remove most of the short-distance fluctuations which give rise to the negative dip in the correlator. And while a comparison was made between the highly-smoothed quenched and dynamical fields it is impossible to draw any strong conclusions, as the lattice spacings were not matched accurately. It is now well established that the shape of the topological charge density correlator depends significantly on the lattice spacing [89, 129].

Table 5.1: The gauge fields used in this study. The lattices were generated by the MILC collaboration [76, 77]. In the following we refer to these ensembles as "quenched," "heavy" and "light."

Size	β	a	Bare Quark Masses
$28^3 \times 96$	8.40	0.086 fm	∞
$28^3 \times 96$	7.11	0.086 fm	27.1 MeV, 67.8 MeV
$28^3 \times 96$	7.09	0.086 fm	14.0 MeV, 67.8 MeV

necessarily has the form

$$\langle q(x)q(0)\rangle = A\delta(x) - f(x)\,, \tag{5.6}$$

where $f(x)$ is positive for all x away from the origin. The negative behaviour of the $\langle qq\rangle$ correlator suggests a sign-alternating layered structure to the topological charge density of the topological charge density correlator.

We begin our study by investigating the effects of dynamical sea-quark degrees of freedom on the topological charge density. In quenched QCD the Witten-Veneziano [131, 132] formula gives a relation between the topological susceptibility and the mass of the η' meson [128]

$$\chi^{qu} = \frac{m_{\eta'}^2 F_\pi^2}{2N_f}\,. \tag{5.7}$$

However, in the full dynamical case the topological susceptibility should vanish in the chiral limit [128, 133]

$$\chi^{dyn} = \frac{f_\pi^2 m_\pi^2}{2N_f} + \mathcal{O}(m_\pi^4)\,. \tag{5.8}$$

Of course, a vanishing topological susceptibility puts no restraints on how the function $\langle q(x)q(0)\rangle$ should change with the addition of dynamical sea-quarks, it only requires that the integral in Eq. (5.5) vanishes.

It is well known that the inclusion of dynamical sea-quarks in the QCD action normalises the coupling constant. In order to maintain the same lattice spacing across quenched and dynamical gauge fields, one finds that the coupling parameter, g, must increase and hence $\beta \sim 1/g^2$ must be smaller for the dynamical fields.

In quenched QCD it is possible to make a prediction on how the amplitude of the delta function, A, of Eq. (5.6) should change as β is altered. In the quenched QCD action formulated in Euclidean space, β appears as a factor governing the width of the probability distribution for gauge-field links. When generating quenched gauge fields, the smaller β values will permit greater fluctuations in the gauge links. The increased fluctuations can give rise to non-trivial field fluctuations, which will be manifest through a greater mean-square topological-charge density $\langle q^2(0)\rangle_x$, and thus a larger A.

However, in full QCD the probability distribution is now proportional to $e^{-S_{\rm Eff}}$, where $S_{\rm Eff} = S_G + \ln \mathrm{Det}[M]$ and M denotes the fermion interaction matrix. Since M depends on both the link variables and the quark masses, it is no longer evident that smaller β values will allow larger fluctuations in the gauge links relative to quenched QCD. Although one can not predict a change in the mean-square density, we can make the following observation. As one approaches the chiral limit $\chi^{dyn} \to 0$, it follows

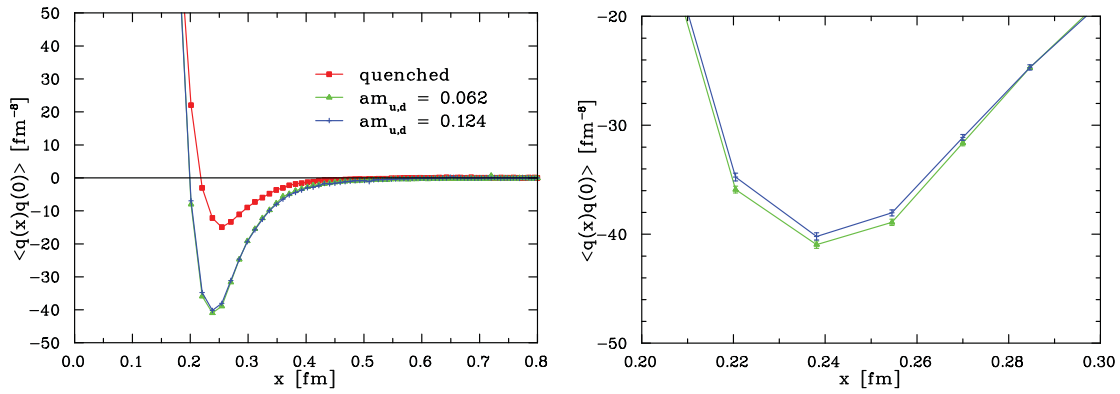

Figure 5.8: A comparison of the $\langle qq \rangle$ correlator for quenched and dynamical gauge fields. The greater field fluctuations present in the dynamical fields are visible through an increase in the magnitude of the negative dip. Although not shown, the contact term $\langle q^2(0) \rangle_x$ has also increased and values are given in the text. The right graph displays the same data focusing on the negative dip for the dynamical fields. The magnitude of the dip is greater for the lighter quark mass.

from Eq. (5.8) that an increasing (decreasing) mean-square density $\langle q^2(0) \rangle_x$ must be compensated for by a stronger (shallower) negative dip in the $\langle qq \rangle$ correlator.

Figure 5.8 examines the extent to which the local field fluctuations differ through a comparison of the $\langle qq \rangle$ correlator for the quenched and two dynamical ensembles. These correlators were generated after using five sweeps of over-improved stout-link smearing to suppress otherwise large renormalisations. We see that the contact term $\langle q^2(0) \rangle_x$ is in fact larger, and the magnitude of the negative dip has also increased. These effects are also stronger for lighter quark masses. This is consistent with our reasoning from considerations of quenched QCD. Smaller quark masses require smaller β values. The exact values of the positive contact term are; quenched $= 1836 \pm 3\,\mathrm{fm}^{-8}$, heavy $= 3344 \pm 5\,\mathrm{fm}^{-8}$, light $= 3443 \pm 4\,\mathrm{fm}^{-8}$.

5.2.3 Instanton-like objects

Understanding the nature of instanton-like objects in the QCD vacuum continues to be an active of area of investigation. Considerable UV filtering reveals the presence of long-distance topological structures in the QCD vacuum. While these topological objects are only approximations to the classical instanton solution, they are commonly referred to as (anti-)instantons.

We now proceed to quantitatively analyse the similarity of the topological objects in the QCD vacuum to the classical instanton solution, using the method for fitting instantons described previously. For this part of the investigation we use 45 sweeps of over-improved stout-link smearing. This corresponds to a λ_{cut} of 634 MeV in the truncated overlap operator as we saw in Chapter 3. A calculation of $q(x_0)$ on the "light" ensemble of dynamical gauge fields (with $\beta = 7.09$) is provided in Fig. 5.9. With the exception of only two outliers, the maxima are good local approximations to the classical instanton solution.

While the centres of the instanton-like objects resemble instantons, it is interesting to

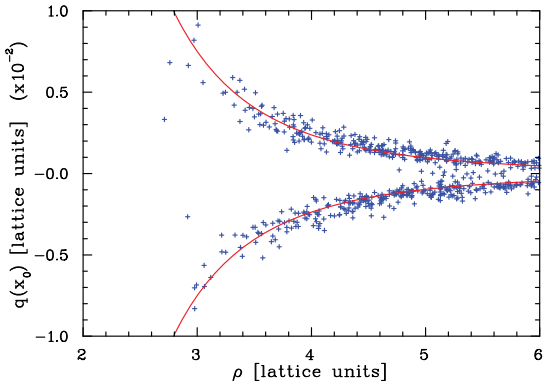

Figure 5.9: Comparison of the calculated $q(x_0)$ after 45 sweeps of smearing with the exact instanton solution. After 45 sweeps of smearing the majority of topological objects are relatively good approximations to instantons at their cores.

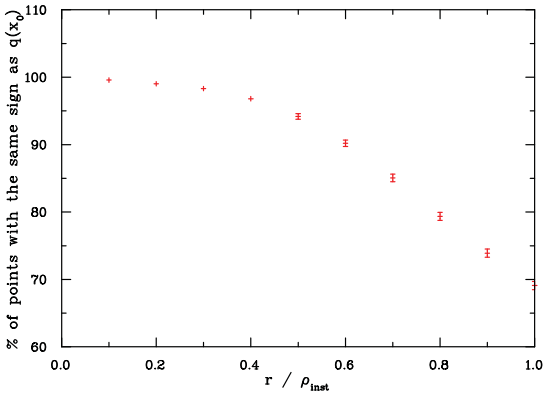

Figure 5.10: The percentage of points that are sign coherent within a relative distance r/ρ_{inst} of each instanton-like objects' centre x_0 with size ρ_{inst}. For small r/ρ_{inst} the percentage of sign-coherent points is close to 100, however the sign-coherence falls off rapidly as r approaches the characteristic size ρ_{inst}.

assess how similar the remainder of the instanton-like objects are to a classical instanton. To do so, we consider all points within a distance r from the centre x_0, measured relative to the instanton size ρ_{inst}, and examine the extent to which the points within this distance have the same sign topological-charge density as observed at the centre, $q(x_0)$. If the detected object is a good approximation to a classical instanton then all these points should have the same charge as $q(x_0)$.

In Fig. 5.10 we show the percentage of points that are within a relative distance r/ρ_{inst} of x_0 that have the same sign as x_0. For small r/ρ_{inst} the percentage of sign-coherent points is close to 100, however it falls off rapidly as r approaches the characteristic size ρ_{inst}. This suggests that although the object is representative of an instanton at its centre, the tails of the objects are distorted by vacuum fluctuations. What is remarkable is that at the characteristic size of the "instanton," merely 2/3 of the points are sign coherent, suggesting that the objects revealed after 45 sweeps of smearing are good approximations of classical instantons only at the core.

Given the strong correlation between $q(x_0)$ extracted from the action density after

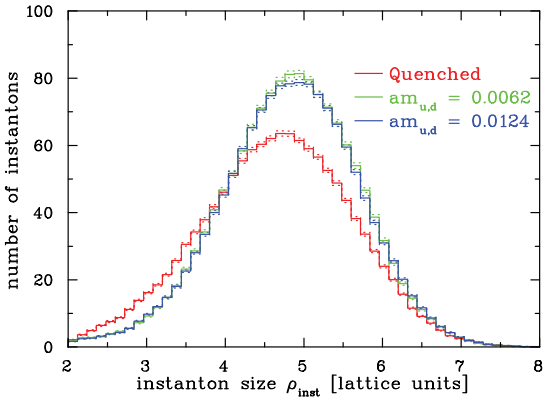

Figure 5.11: Histogram of the instanton size ρ_{inst} in dynamical and quenched gauge fields. The dynamical fields show both an increase in the number of instantons and in the average instanton size.

45 sweeps of smearing and that given by the classical solution (5.3) we can now compare "instanton" distributions between quenched and dynamical QCD.

Early attempts [134] to reveal differences in the distributions were limited by statistical fluctuations, concluding that the differences must be subtle. However, this high-statistics study exploiting the accuracy of over-improved stout link smearing is able to resolve differences for the first time.

To examine the variation in instanton size between the different gauge fields, a histogram of ρ_{inst} is presented in Fig. 5.11. Compared to the quenched ensemble, the dynamical gauge fields show a substantial increase in the total number of instantons and a subtle but important increase in average instanton size. Our sample size of $73,000$ instantons from quenched QCD and $140,000$ from full QCD enables a precise determination of the means of the distributions. We find $\rho_{\text{inst}}(\text{Quenched}) = 4.646(4)$, $\rho_{\text{inst}}(\text{am}_{\text{u,d}} = 0.0062) = 4.822(4)$, and $\rho_{\text{inst}}(\text{am}_{\text{u,d}} = 0.0124) = 4.825(3)$, and the standard deviations of the distributions to be $\sigma(\text{Quenched}) = 0.96$, $\sigma(\text{am}_{\text{u,d}} = 0.0062) = 0.87$, $\sigma(\text{am}_{\text{u,d}} = 0.0124) = 0.87$. These results are similar in spirit to our observations of the short-distance $\langle qq \rangle$ correlator in that the introduction of dynamical fermion degrees of freedom leads to more non-trivial topological charge fluctuations, at both short and long distances.

It has been argued that an increased density of instanton-like objects on the lattice could be explained through an instanton/anti-instanton attraction occurring due to the presence of the fermion determinant in the QCD weight factor [133]. The idea is that an isolated instanton or anti-instanton would give rise to a near zero mode of the Dirac operator. When generating dynamical gauge fields the selection of typical configurations is weighted by $\det(\not{D}+m)e^{-S_g}$. If a near zero-mode of $\not{D}$ were to exist on the lattice then the determinant would approach 0 in the chiral limit and it would be highly improbable that the configuration would be selected. Thus, isolated instantons are unlikely to exist in the light dynamical-fermion gauge fields and hence all instanton-like objects will be closer in these fields. Combined with our earlier results displaying increased fluctuations in the gauge-field links, these considerations lead one to anticipate a greater number of instanton-like objects in the dynamical gauge fields and an increase in their size to aid

in suppressing isolation.

5.2.4 Topological charge density

The effects of dynamical fermion degrees of freedom are realised significantly at short distances in the calculation of the $\langle qq \rangle$ correlator. The increased magnitude of the non-trivial topological charge field fluctuations that are permitted due to the inclusion of fermion loops should also be visible in direct visualisations of the topological charge density.

Using five sweeps of over-improved stout-link smearing, we consider the short-range structure of the topological charge density. In Fig 5.12 we present the topological charge density for the quenched and two dynamical ensembles. The extra field fluctuations are clearly visible in the visualisations of the dynamical QCD vacuum structure.

In Fig 5.13, we compare the structure of the vacuum after 45 sweeps of over-improved smearing as discussed in Sec 5.2.3. It is difficult to observe the increased density of instantons upon the introduction of dynamical fermions in these figures. This is because the charge density fluctuates over a long times scale and a single time-slice is insufficient to portray an complete representation of the vacuum. We also note that despite the apparent separation of these topological lumps in the vacuum, all regions of like charge are connected throughout the gauge field; i.e. one can travel from one lump to any other lump of the same charge along a sign-coherent path of small-magnitude topological-charge density. This has been examined in detail elsewhere [94, 129].

5.3 Summary

Using the new over-improved stout-link smearing algorithm from Chapter 2 we are able to perform the most accurate studies of QCD vacuum structure to date. The use of this smearing algorithm allows one to accurately expose the differences between quenched and dynamical fields on both long and short distance scales.

By suppressing large renormalisations of the lattice operators through five sweeps of over-improved stout-link smearing on the gauge fields, which corresponds to the unfiltered overlap operator [121], we are able to demonstrate how dynamical fermions affect the vacuum through a calculation of the topological charge density correlator. The addition of fermions into the QCD action at constant lattice spacing renormalises the coupling constant such that the coupling parameter β becomes smaller. In the quenched approximation such a change permits greater field fluctuations, and this is realised in full QCD. We find an increase in the mean-square topological charge density upon including dynamical fermions, as is illustrated in Fig. 5.8. The larger contact term, reflecting the greater mean-square topological charge density of dynamical configurations, also induces an increase in the negative dip of the topological charge density correlators. The strength of these compensating effects is expected to increase as one approaches the chiral limit.

The results also reflect the suppression of zero-modes due to the inclusion of the $\det(\not{D}+m)$ weight factor in the selection of typical gauge fields, resulting in a decrease in the number of isolated instanton-like objects. This causes instantons and anti-instantons

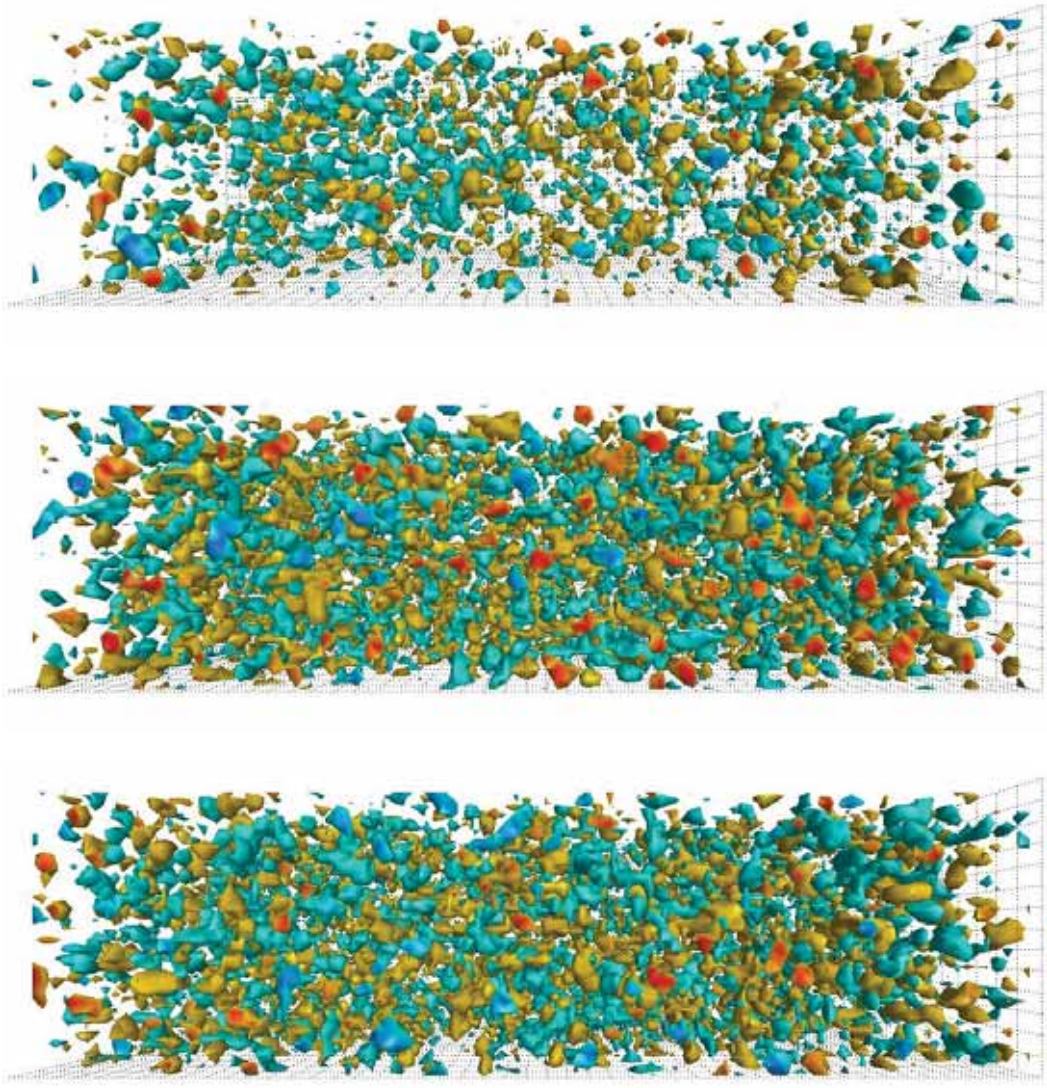

Figure 5.12: The topological charge density for the quenched and dynamical ensembles, obtained after five sweeps of over-improved stout-link smearing. From top to bottom we plot a quenched field, the heavy dynamical $am_{u,d} = 0.0124$, $am_s = 0.031$ field and the light dynamical $am_{u,d} = 0.0062$, $am_s = 0.031$ field. The greater non-trivial field excitations that are permitted upon the introduction of light dynamical fermions are directly visible in the dynamical illustrations.

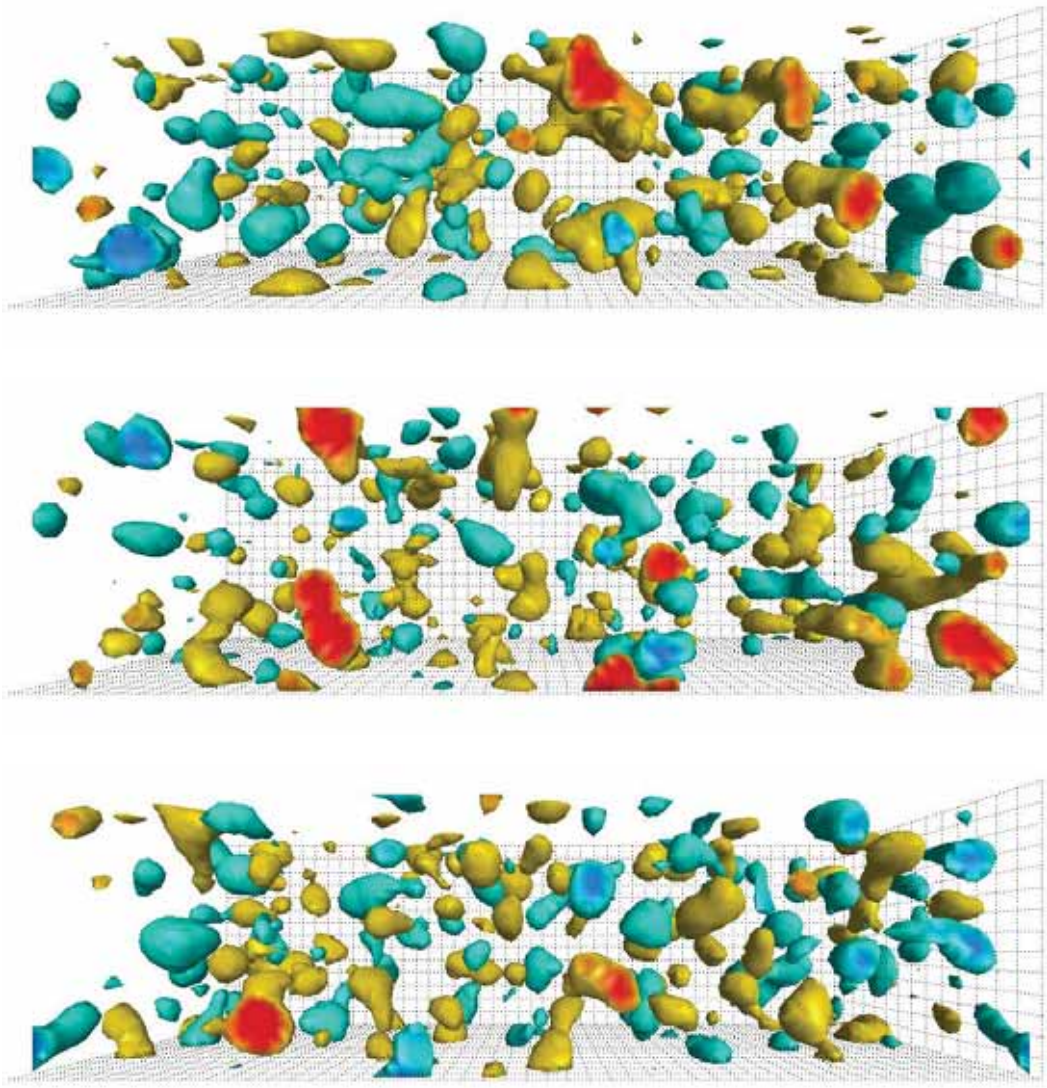

Figure 5.13: The topological charge density for the quenched and dynamical ensembles, obtained after 45 sweeps of over-improved stout-link smearing. From top to bottom we plot a quenched field, the heavy dynamical $am_{u,d} = 0.0124$, $am_s = 0.031$ field and the light dynamical $am_{u,d} = 0.0062$, $am_s = 0.031$ field. The longer correlation length makes it difficult to observe a noticeable difference in the size-distribution of the gauge field fluctuations when observing a single time-slice.

to be "attracted" [133] and leads to an increase in both the density and size of instanton-like objects in the dynamical gauge fields as illustrated in Figs. 5.11 and 5.12.

These results support the emerging picture of the vacuum as an alternating "sandwich" of opposite topological charge density [129]. Beneath this oscillating short-range structure there exists a long-distance foundation of instanton-like objects [89, 130, 135] that can be revealed through smoothing or Dirac eigenmodes [121]. The addition of dynamical fermions allows stronger field fluctuations and a higher frequency of sign-oscillations in the topological charge density. The density of instanton-like objects beneath these short-distance oscillations also increases, as does their average size.

Chapter 6

Preconditioning maximal centre gauge with stout-link smearing

The content of this chapter is based on the paper: A. O. Cais, W. Kamleh, K. Langfeld, B. Lasscock, D. Leinweber, P. Moran, A. Sternbeck and L. Smekal, arXiv:0807.0264 [hep-lat].

In Chapter 5 we used over-improved stout-link smearing in order to investigate the effects of dynamical quarks on QCD vacuum structure. We intend to extend our investigations into the effects of dynamical sea quarks in Chapter 8 with calculations of the proton and Δ^+ electromagnetic form factors. However, for the moment we continue our topological studies into the structure of the QCD vacuum and present an application of how smearing smearing algorithms can also be used to precondition Maximal Centre Gauge (MCG) fixers.

To this end, centre vortices are studied in the SU(3) gauge theory using MCG fixing. Stout link smearing and over-improved stout link smearing are used to construct a preconditioning gauge field transformation, applied to the original gauge field before fixing to MCG. We find that preconditioning successfully achieves higher gauge fixing maxima. We observe a reduction in the number of identified vortices when preconditioning is used, and also a reduction in the vortex-only string tension.

6.1 Introduction

Despite more than 30 years of intense study, quark colour confinement in hadron physics remains unexplained (for a recent overview see Ref. [136]). Within the framework of lattice gauge theory, the prevailing view is that quark confinement is the result of a particular class of gauge field configurations which dominate the QCD vacuum on large distance scales. Two potential candidates have been most commonly investigated: confinement by means of Z_N centre vortices and confinement due to Abelian monopoles (for a critical discussion of both see Ref. [137]). To enhance these particular features, gauge fields can be first fixed to a suitable gauge, such as Maximal Abelian Gauge (MAG) [138] or Maximal Centre Gauge (MCG) [139]. Monopoles and centre vortices are then defined by the projection of these gauge-fixed fields onto $U(1)^{N-1}$ or Z_N, respectively.

Significant progress to date has occurred in $SU(2)$ using MAG and MCG, with original findings reproducing about 90% [140] and about 100% [141], respectively, of the non-Abelian string tension. Removing monopole [142–144] or centre-vortex [144–149] degrees of freedom from $SU(2)$ lattice gauge fields appears to leave topologically trivial, non-confining gauge fields that do not spontaneously break chiral symmetry.

The significance of the centre of the gauge group is what connects possible candidates for this special class of configurations. As outlined for the case of Laplacian Centre Gauge (LCG) in Ref. [150], *all* monopole world lines are embedded in 2-dimensional vortex surfaces. These topological objects naturally occur together as local gauge defects. In MCG it has been observed computationally that over 90% of monopole currents are localised on centre vortices [151, 152]. Strongly correlated effects between the two have also been observed by means of studying monopoles after vortex removal and vice-versa [153], as well as through the effect of their removal on the spectra of the overlap Dirac operator [144].

Again, all these advancements have been in $SU(2)$ and work in $SU(3)$ has not progressed to this level. While initial investigations were hopeful [154, 155], subsequent results for MCG [156, 157] had difficulty in reproducing the full non-Abelian string tension. Investigations using MAG were also discouraging [158] , however subsequent analysis has observed good Abelian dominance [159] in the unquenched case. Earlier studies in $SU(2)$ using MCG reported that the centre-projected configurations recovered the full string-tension, however further study into the ambiguities of the gauge-fixing procedure showed that this result is plagued by Gribov copy effects [160–162]: methods which give higher values of the gauge fixing functional produce smaller values for the vortex-induced string tension. We point out that when the Laplacian Centre Gauge of Refs. [150, 163] (which is free of Gribov ambiguities on the lattice) is used as the fixing method, the full $SU(3)$ (and $SU(2)$) string tension is recovered for the centre-projected gauge fields but *only* in the continuum limit. However, unlike MCG vortices [164], the interpretation of LCG vortex matter is cumbersome in the same continuum limit [156, 165].

In the current work we focus on the Gribov problem of the $SU(3)$ centre-vortex picture of confinement using the MCG fixing method. We apply the "smeared gauge fixing" method of Ref. [166] to MCG to ameliorate this Gribov problem. This creates a pre-conditioning gauge transformation for the configuration that should bring it closer to the global maximum. We investigate the effect of this method on the features of the long-distance behaviour of the static quark potential as evaluated on configurations where the P-vortices derived from MCG have been removed and configurations composed purely of these P-vortices. In $SU(2)$, it has been shown that centre-vortex removal specifically targets topological properties [144, 147], so as well as using stout-link smearing we also employ over-improved stout-link smearing to attempt to exploit the link to topological structure.

6.2 Methodology

6.2.1 The static quark potential

The spectrum of the static quark potential is determined from Wilson loops $W(r,t)$ of area $r \times t$,

$$W(r,t) = \sum_i C_i(r)\, \exp(-V_i(r)\, t)\,. \tag{6.1}$$

In order to enhance $C_1(r)$, which measures the overlap of the loop with the ground state potential, the spatial links are smeared.

Efficient methods exist for the unimproved Wilson action for fine tuning the smearing parameters to provide optimal overlap with the ground state potential. For $t = 0$, $W(r, t = 0) = 1$ providing the constraint $\sum_i C_i(r) = 1$ for a given r. For unimproved actions, where the transfer matrix is positive definite, each $C_i(r) \geq 0$. This means $C_1(r)$ can be monitored at large r but small t as the number of smearing sweeps are varied, with the optimal amount of smearing occurring when $C_1(r) \approx 1$. The proximity of $C_1(r)$ to 1 for small t may be easily estimated from the ratio

$$W^{t+1}(r,t)/W^t(r,t+1) \tag{6.2}$$

which equals $C_1(r)$ in the limit $C_1(r) \to 1$. This provides a quantitative measure of ground-state-dominance for unimproved Wilson actions. We note that it is sufficient [167] to fix the smearing fraction, α, and explore the parameter space via the number of smearing sweeps, n.

This procedure can be repeated for a number of alternate paths of links for a given separation r. By using variational techniques as described in Ref.[168], the combination of paths that gives the greatest overlap with the ground state can be found.

Wilson loops, $W(r,t)$, or more precisely $W(x,y,z,t)$ where $r^2 = x^2 + y^2 + z^2$, are calculated both on-axis, along the Cartesian directions, and off-axis. On-axis Wilson loops are those that lie, e.g., in the $x - t$ plane only; off-axis loops begin, for example, by first stepping into the y or z (or both) directions before proceeding through the $x - t$ plane.. This provides an alternative to the usual method of calculating the off axis potential by building paths in three different directions using small elemental squares, rectangles or cubes and multiplying them together to form larger paths (see, for example, Ref. [169]). These standard techniques for calculating the off-axis potential may be combined with the approach described here using the variational method described extensively in Ref. [168].

Due to the periodicity of the lattice, the size of our Wilson loops are limited from 1 to a little over half the smallest lattice dimension in the on-axis directions and between 0 and 3 in the transverse directions. For example, for a $16^3 \times 32$ lattice, the sizes of the Wilson Loops, $t \times x \times y \times z$, vary from a $1 \times 1 \times 0 \times 0$ loop, to a $10 \times 10 \times 3 \times 3$ loop. Statistics are improved by transposing the loops over all points on the lattice and by rotating through the three spatial directions

In order to efficiently calculate Wilson loops of various sizes, including off-axis loops, we build products of links in each direction that we are considering for our Wilson loop. Link products extending from every lattice site are calculated in parallel. The loops

are then formed in parallel by multiplying the appropriate sides together. Each side is created by reusing the components of the previous loop and one additional link. The same approach can be extended to loops that travel off-axis.

In an attempt to isolate the ground state potential for off-axis paths, one symmetrises over the path of links connecting the off-axis heavy quark propagators, exploiting the full cubic symmetry of the lattice. For example, two points separated by n_x sites in the x-direction, n_y sites in the y-direction and n_z sites in the z-direction, may be connected by n_x link products in the x-direction, n_y link products in the y-direction and n_z link products in the z-direction which we denote by the triplet xyz. Instead of only calculating off-axis paths in the specific order xyz, we average over spatial paths calculated in the order $xyz, xzy, yxz, yzx, zxy, zyx$. We calculated loops using this path-symmetrised technique as well as loops using a non-path-symmetrised operator where the order xyz alone is considered. The former form of operator is designed to suppress excited states by incorporating the full hyper-cubic symmetry of the lattice, whereas the latter operator is susceptible to excited state contamination. By comparing the static quark potential for these two operators, one can gain qualitative information on the effect of excited states in the static quark potential.

6.2.2 Identifying vortex matter

In the centre-vortex picture of confinement the gauge fields are considered to be decomposed into a long-range, smooth field Z_μ carrying all the confining fluctuations and a short-range field V_μ containing non-confining perturbations as well as other short-range effects

$$U_\mu(x) = Z_\mu(x)V_\mu(x).$$

Here $Z_\mu(x)$ is the centre element which is closest, on the $SU(3)$ group manifold, to $U_\mu(x)$. A vortex is a configuration of the gauge potentials topologically characterised by non-trivial elements of Z_3 and is created by a singular gauge transformation. The non-trivial centre element of the singular gauge-transformation characterising the vortex may be made to be distributed over many links of an encircling loop (due to the short-range effects of $V_\mu(x)$). If we assume that by a gauge transformation the non-trivial centre element can be concentrated on just one link we can compress this *thick* vortex into a *thin* one. If we then project this gauge transformed configuration onto its centre elements, the projected vortices (P-vortices) linking with the loop should then correspond to the thin vortex. It is for this reason that we adopt the use of gauge-fixing to obtain the necessary gauge transformation. It is the choice of gauge that determines our method for finding the centre vortices and, therefore, the connection between the P-vortices and the thick centre vortices present in the original configuration. The particular choice of gauge, the properties of the P-vortices associated with each choice and the Gribov problem that it creates is what has polarised opinions in this area [150, 156, 160, 170, 171].

Here, we employ the MCG gauge-fixing algorithm as outlined in Ref. [156]. The gauge condition we chose to maximise (with respect to the gauge transformations $\Omega(x)$) in this algorithm is

$$V_U[\Omega] = \frac{1}{N_l}\sum_{x,\mu}\big[\frac{1}{3}\mathrm{tr}U^\Omega_\mu(x)\big]\big[\frac{1}{3}\mathrm{tr}U^\Omega_\mu(x)\big]^\dagger,$$

where N_l is the number of links on the lattice and U^Ω is the gauge-transformed field.

After fixing the gauge, each link should be close to a centre element of $SU(3)$, $Z^m = e^{i\phi^m}$, $\phi^m = \frac{2\pi}{3}m$ with $m \in \{-1, 0, 1\}$. Since, for every link,

$$\frac{1}{3}\mathrm{tr}U^\Omega_\mu(x) = u_{x,\mu}e^{i\phi_{x,\mu}} \quad \text{and} \quad \phi_{x,\mu} = \tan^{-1}\frac{\mathrm{Im}(\mathrm{tr}U^\Omega_\mu(x))}{\mathrm{Re}(\mathrm{tr}U^\Omega_\mu(x))}$$

then $\phi_{x,\mu}$ should be near to some ϕ^m, by construction of the gauge-fixing condition. We then perform the centre projection by mapping

$$SU(N) \mapsto Z_N : \; U^\Omega_\mu(x) \mapsto Z_\mu(x) \quad \text{with} \quad Z_\mu(x) = e^{i\phi^m_{x,\mu}},$$

with the appropriate choice of $\phi^m_{x,\mu}$, $m \in \{-1, 0, 1\}$.

To reveal the vortex matter we simply take a product of links around an elementary plaquette. We say a vortex pierces the plaquette if this product is a non-trivial centre element and the plaquette is then a *P-vortex*. We can remove these P-vortices by hand from the configuration using $U'_\mu(x) = Z^\dagger_\mu(x)U^\Omega_\mu(x)$.

6.2.3 Smearing as a preconditioner

In the centre-vortex picture of confinement, the centre elements correspond to the long-range physics. It would seem reasonable then to employ the use of smearing to smooth out the short-range fluctuations and allow the gauge transformation to see more of the underlying long-range physics. To this end we construct a preconditioning gauge transformation for each gauge field to obtain higher maxima in the gauge-fixing procedure and thereby directly address the Gribov-copy issue [166].

Firstly, we smear the gauge field using any smearing algorithm (stout-link smearing [71] has been applied here as well as over-improved stout-link smearing which has been shown to better preserve the topological structure underlying the original configuration [172]). We then fix the smeared field using the MCG gauge-fixing method. At each iteration we keep track of the total gauge transformation that has been applied to the smeared gauge field. Once the algorithm has converged we use the stored total transformation as a preconditioning gauge transformation for the unsmeared gauge field. We emphasise that the (unsmeared) preconditioned gauge field remains on the same gauge orbit since the preconditioning is merely a (specific) gauge transformation on the original links. Gauge-fixing the preconditioned field simply gives us a Gribov-copy of the result from gauge-fixing the original gauge field.

6.3 Results

Calculations are performed using 200 quenched configurations with the Lüscher-Weisz plaquette plus rectangle gauge action [80] on a $20^3 \times 40$ lattice with $\beta = 4.52$. Similar preliminary results have being found on 100 $16^3 \times 32$ lattices (with $\beta = 4.6$) and have been reported elsewhere [173].

Stout-link smearing with a smearing parameter of 0.1 is used to construct the preconditioning transformation with the number of sweeps ranging from 0 to 20 in steps of

Sweeps	Iteration Blocks	Smear Max	Max	Vortices
0	80 ± 20	–	0.7350(7)	3.21(12)%
4	118 ± 22	0.9150(11)	0.7400(6)	1.93(10)%
8	126 ± 26	0.9369(54)	0.7407(6)	1.71(10)%
12	126 ± 21	0.9459(12)	0.7411(6)	1.58(10)%
16	128 ± 23	0.9506(12)	0.7412(6)	1.53(10)%
20	135 ± 26	0.9541(12)	0.7414(5)	1.45(11)%
OI 80	148 ± 29	0.9625(14)	0.7417(6)	1.28(13)%

Table 6.1: Results for the average maximum gauge condition $V_U[\Omega]$ as a function of preconditioning stout-link smearing sweeps (OI signifies over-improved stout-link smearing). For each of the sweeps used in the preconditioning: the average total (smeared gauge field fixing plus preconditioned gauge field fixing) number of blocks of 50 iterations used, the average smeared gauge condition maximum reached, the average preconditioned gauge condition maximum reached and the percentage of plaquettes that are P-vortices.

4 sweeps. We also employ over-improved stout-link smearing with a smearing parameter of 0.06 and an ϵ parameter of -0.25. Here, each preconditioning was conducted independently.

Given that the original goal was to increase the gauge-fixing maxima achieved in MCG fixing, we can see from Table 6.1 that we are successful, in this regard, in every case. With each level of preconditioning a higher gauge condition maximum is achieved both for the smeared gauge field and the preconditioned original field. If we compare 0 and 4 sweeps of preconditioning, we can see that the magnitude of this increase is initially large but the increase is slower as we precondition to higher levels. However this increase does not come without a cost, the number of gauge-fixing iteration blocks (a block is 50 iterations) required almost doubles between the unpreconditioned fixing and the maximum amount of preconditioning. Typically, two-thirds of the iterations are spent fixing the smeared field and one-third fixing the preconditioned field.

What is most significant about this table however is that with each level of preconditioning the percentage of projected plaquettes which are P-vortices drops significantly. Without preconditioning 3.21% of plaquettes are vortices and this drops to as low as 1.28% for the highest level of preconditioning.

In Table 6.2 we investigate further by looking at this particular effect between all the different levels of preconditioning. In the upper triangle of this table (from preconditioning level row to preconditioning level column) we report the percentage of configurations that experience a reduction in the measured number of P-vortices. As we can see, this percentage is always high but the effect is lessened as we move to transitions, particularly small transitions, between higher levels of preconditioning. It should be noted however that the relative difference between, for example, 20 sweeps of stout-link and 80 sweeps of over-improved stout-link preconditioning is difficult to quantify but the effect is still significant for this transition.

The magnitude of this effect is also reported in Table 6.2. When reading from the lower triangle (preconditioning level column to preconditioning level row) of this table

Sweeps	0	4	8	12	16	20	OI 80
0	$\ddots$	100	100	100	100	100	100
4	$39^{\pm 4}$	$\ddots$	96.5	100	100	100	100
8	$46^{\pm 4}$	$11^{\pm 6}$	$\ddots$	81.5	91.5	97.5	99.5
12	$50^{\pm 4}$	$17^{\pm 6}$	$9^{\pm 6}$	$\ddots$	69	81	97.5
16	$52^{\pm 3}$	$20^{\pm 6}$	$12^{\pm 6}$	$7^{\pm 5}$	$\ddots$	69.5	95.5
20	$54^{\pm 4}$	$24^{\pm 7}$	$15^{\pm 7}$	$10^{\pm 7}$	$8^{\pm 6}$	$\ddots$	85.5
OI 80	$59^{\pm 4}$	$33^{\pm 7}$	$24^{\pm 8}$	$19^{\pm 9}$	$16^{\pm 9}$	$14^{\pm 8}$	$\ddots$

Table 6.2: Comparisons between different preconditioning levels of stout-link smearing (OI signifies over-improved stout-link smearing). The upper triangle of this table (from preconditioning level row to preconditioning level column) we report the percentage of configurations that experience a reduction in the measured number of P-vortices. The lower triangle (preconditioning level column to preconditioning level row) of this table gives the percentage reduction of the number of P-vortices for the configurations that experienced a reduction.

we can see the percentage reduction of the number of P-vortices for the configurations that experienced a reduction. In the transition from no preconditioning to any other level, the order of a 50% reduction is observed. For other transitions it would seem the effect drops to the 10% level reasonably quickly, but again we see an increased effect when we consider over-improved smearing. It should be noted that, regardless of the preconditioning level, the centre phases of the links of the fields always remain evenly distributed across the three possible values, reflecting the fact that the realisation of centre symmetry remains unaffected.

We can look to Table 6.3 when considering whether a higher gauge-fixing maximum translates into a lower number of P-vortices. When reading from preconditioning level row to preconditioning level column, the percentage of configurations that experience an increase in the gauge-fixing maximum is shown. Similar trends to that of Table 6.2 are observed, with large effects initially which become reduced for small transitions between higher levels. Of these configurations with an increased maximum we can see almost exclusively (when reading from preconditioning level column to preconditioning level row) that an increased gauge-fixing maximum does lead to a lower number of P-vortices.

6.3.1 The static quark anti-quark potential

The fact that we can reduce the number of P-vortices through preconditioning is not necessarily a cause for concern. As stated previously, our method for determining the location of centre vortices is only justified by the physical relevance of the P-vortices that we determine. A first step in determining this relevance is the calculation of the static quark anti-quark potential. In the centre-vortex picture, the string tension σ as determined from the infrared behaviour of this potential should be fully accounted for by the centre-vortex component of the gauge fields, Z_μ, with the Coulombic term accounted

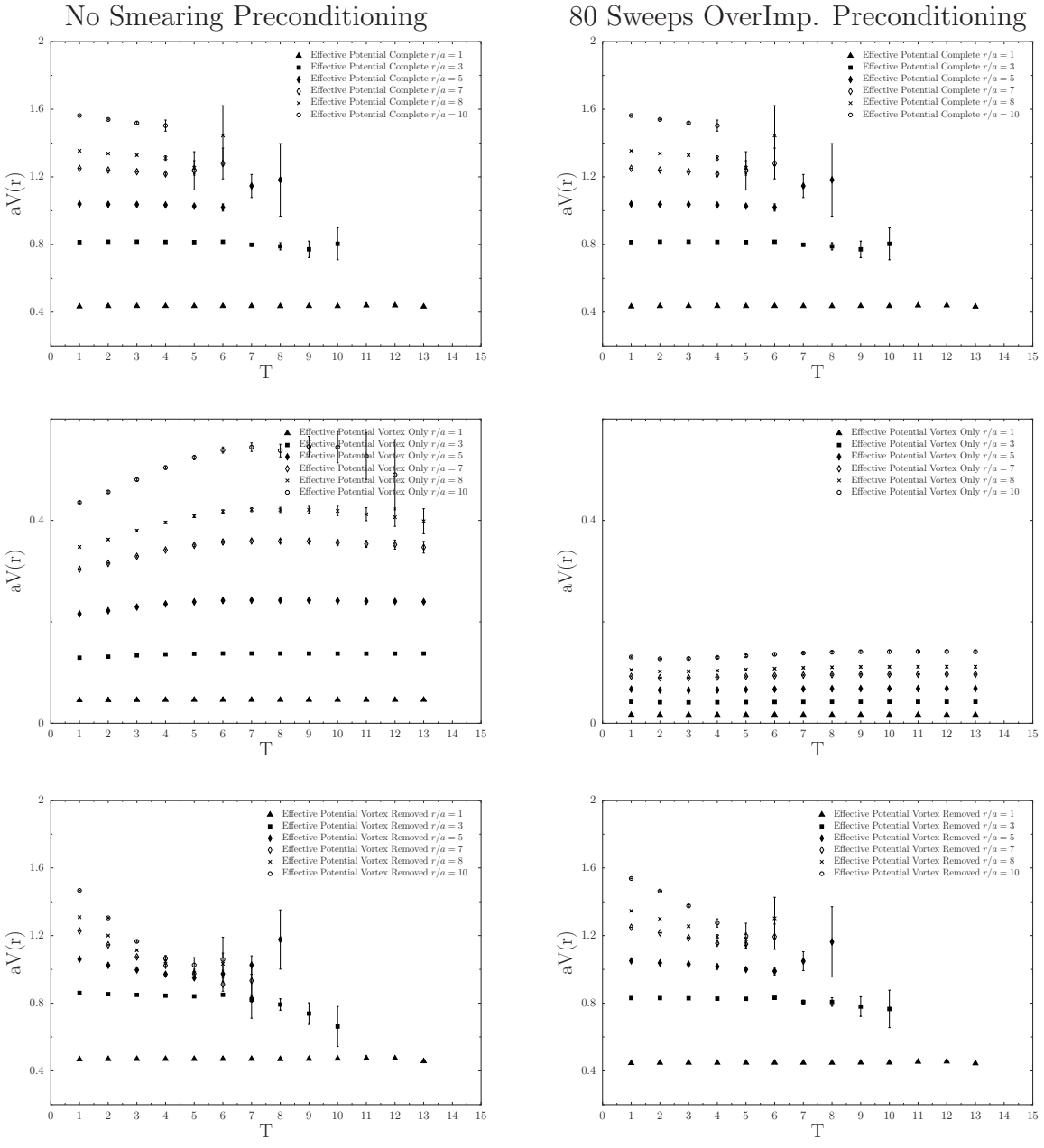

Figure 6.1: The effective potential plots for the lowest (left) and highest (right) levels of preconditioning smearing. The upper plots contain the data for the original gauge-fixed configurations, the middle plots contain the data for the vortex-only configurations and the lower plots contain the data for the vortex-removed configurations. Each plot contains data for a range of quark separations.

Sweeps	0	4	8	12	16	20	OI 80
0	$\ddots$	100	100	100	100	100	100
4	100	$\ddots$	89.5	98	99	100	100
8	100	100	$\ddots$	75	78.5	89.5	93.5
12	100	100	95.33	$\ddots$	59	71.5	87.5
16	100	100	98.09	97.46	$\ddots$	62.5	77.5
20	100	100	100	97.2	93.6	$\ddots$	71
OI 80	100	100	100	100	100	97.18	$\ddots$

Table 6.3: Comparisons between different preconditioning levels of stout-link smearing (OI signifies over-improved stout-link smearing). When reading from sweep row to sweep column (upper triangle) the value shown is the percentage of configurations that achieve a higher gauge fixing maximum. When reading from sweep column to sweep row (lower triangle) the value shown is the percentage of the configurations with higher maximum that achieve a lower number of P-vortices.

for by the vortex removed component, V_μ. Since we can "remove" the determined P-vortices by the operation $U'_\mu(x) = Z^\dagger_\mu(x)U^\Omega_\mu(x)$, we can seek to observe these properties directly. However, since the determined P-vortices are gauge-dependent (and their number Gribov-copy dependent, as we have already seen) then so too are the subsequent measurements of the static quark potential from the vortex-only and vortex-removed components of the configuration.

Computing the static quark anti-quark potential as a function of the quark separation is a two step process. Wilson loops $W(R,T)$ of extension of $R \times T$ have the large T behaviour

$$\langle W(R,T)\rangle \propto \exp\{-V(r)aT\}, \qquad r := Ra,$$

where a is the lattice spacing. The method for extracting the effective potential is thus identical to that of extracting effective masses from two-point functions in hadronic spectroscopy. To obtain the static quark anti-quark potential as a function of the quark separation we simply repeat this process for a range of values of the separation R. By using off-axis spatial paths for the Wilson loops, we can obtain non-integer values of R. We exploit full space-time translation to improve the statistics of our Wilson loops.

Since the final plot is composed of fits performed on a large number of effective potential plots for all the different separations, it is prudent and necessary that the factors determining those fits are given, and taken into account, when analysing the subsequent static quark anti-quark potential as a function of separation. The difficulties associated with such fits can be easily recognised in Fig. 6.1. In these plots we show the static quark potential for a variety of quark separations for each of the original, vortex-only and vortex-removed configurations. On the left we show these plots for the unpreconditioned MCG fixing and on the right we show the same plots for 80 sweeps of over-improved smearing as a preconditioner.

One of the first things to discuss is the difficulty in obtaining a satisfactory fit range for the data, particularly in the case of the vortex-removed configurations. With these

configurations, more so at larger separations, the potential falls rapidly and decays into noise quickly. A visually satisfying plateau region is not evident and we must rely on the fitting routine to determine the goodness of the fit. What the plot can tell us is that the effective potential continues to fall (at separations of 5 lattice spacings and greater) until at least time-slice 5. Since the data decays into noise around this point, we chose to constrain our fit using timeslice 5 and fit from this slice to slice 7 (a straight-line fit to 3 points). This constraint is then applied to all values of the separation. What we find is that while this may lead to reasonable ($\lesssim 1.3$) values of the χ^2 per degree of freedom in the majority of cases, there are certainly significant deviations from this desirable result.

Global fit ranges are chosen in a somewhat similar way for the unpreconditioned and vortex-only configurations. For the unpreconditioned configurations, the global fit-range was chosen to be between timeslice 4 and 6 since these accounted for the systematic drift of the potential at large separations for lower time values and also gave reasonable χ^2 behaviour. In the case of the vortex-only configurations, the errors are far more controlled but the potential rises at small times and plateaus far later so the fit range was chosen to be from timeslice 10 to 12 but again some of the χ^2 per degree of freedom values were unsatisfactory. This is most likely due to the heavy constraints placed on the fit by the accurate potential determinations.

Of significant concern when comparing the potentials of the unpreconditioned and preconditioned results in Fig. 6.1 is the direct comparison of the potentials in each case. The top figures show the potential after gauge-fixing but prior to the centre projection and vortex-removal and, of course, since the static quark potential is gauge invariant these plots are identical. For the lowest plots, which contain the vortex-removed data, we can see that the rate of decay for the preconditioned data has dropped and the quality of the data does not allow us to see whether it is possible that it plateaus at the same level as the unpreconditioned data. Of course the most dramatic effect occurs in the middle plots with the vortex-only data. There is a dramatic reduction in the magnitude of potential for all separations and this is direct manifestation of the Gribov-copy effect for this gauge-fixing method.

This Gribov-copy effect is also manifest in Fig. 6.2. Here we show plots of the effective potential as a function of separation for each of the six levels of preconditioning used as well as the unpreconditioned data. It would appear that the findings are consistent with loss of confinement upon P-vortex removal. Although it would seem that this is perhaps not such a reasonable observation in the over-improved case, if we look exclusively at the on-axis contributions to the potential in this case (Fig. 6.3) and compare it to that of the unpreconditioned case, we observe that a plateau in the potential may exist but at larger values of the separation. This would concur with our previous observation that the potential takes longer to plateau in this case and therefore the fit window may not be adequately account for this effect. Careful examination of the vortex-removed plot also reveals that we obtain an increasingly more accurate fit to the short-range Coulombic portion of the potential.

What is more significant however is that the value of the string-tension determined from the vortex-only configurations drops dramatically, and systematically, from $\sim 60\%$ to as low as $\sim 16\%$ of the full string tension with increased preconditioning providing

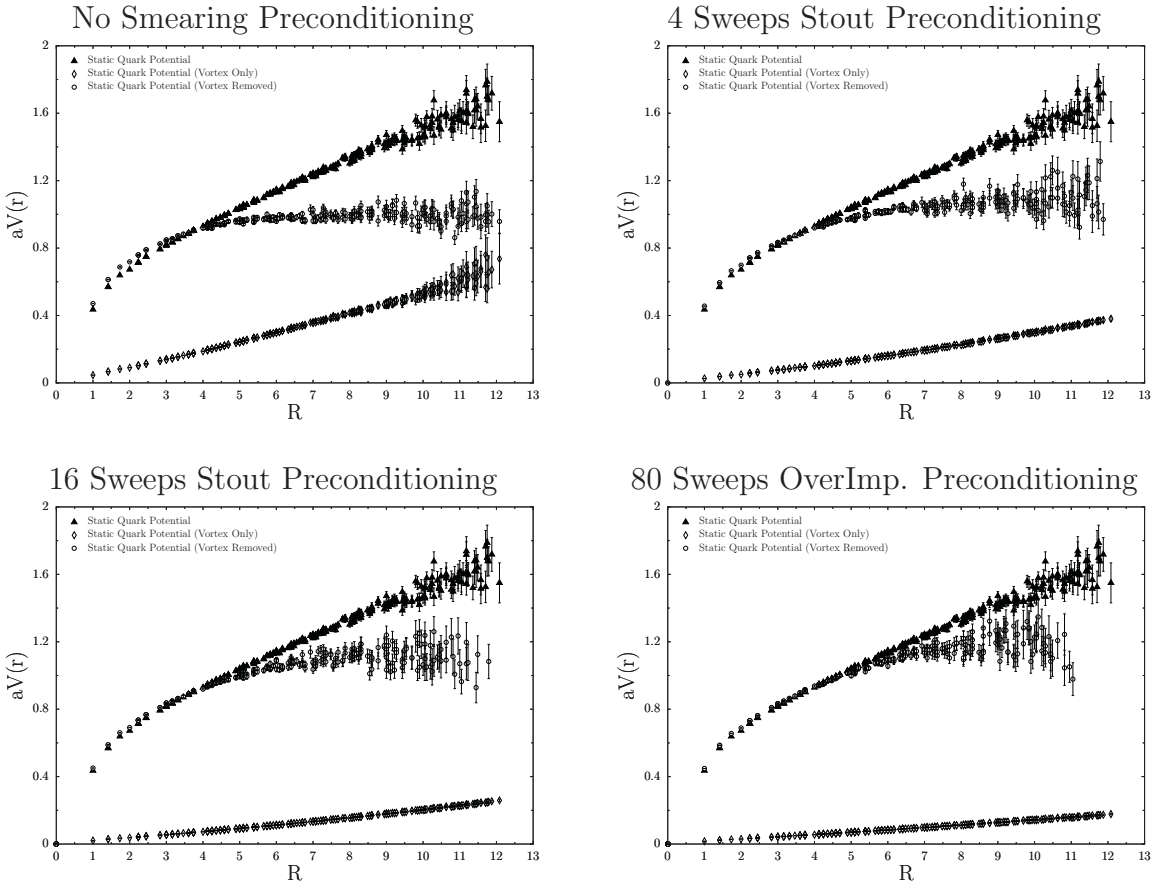

Figure 6.2: Static quark anti-quark potential plots for each of preconditioning smearing sweeps used. Each plot contains data for the full, vortex-removed and vortex-only configurations.The data shown uses a 3 timeslice fit window in each case with the fit window being from timeslice 4 to 6 for the full data, timeslice 5 to 7 for the vortex-removed data and timeslice 10 to 12 for the vortex-only data.

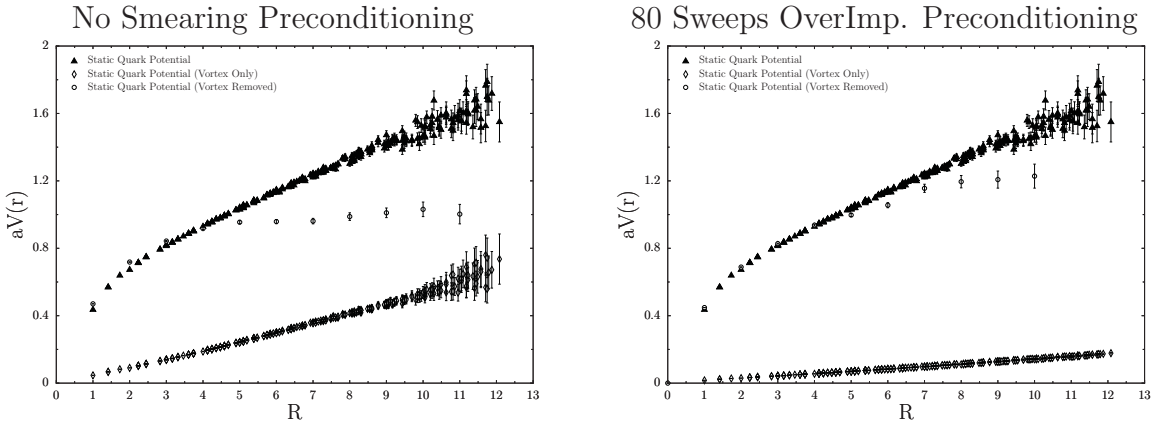

Figure 6.3: The static quark anti-quark potential plots for both the lowest (left) and highest (right) levels of preconditioning. Only the on-axis data is shown for the vortex-removed configurations.

improvement. This is a disturbing manifestation of the Gribov problem since it perhaps questions how accurately we have determined the centre vortices by our projection of the P-vortices with our fixing method.

6.3.2 Discussion

The use of smearing as a preconditioning technique does indeed lead to higher maxima in the MCG gauge-fixing condition $V_U[\Omega]$. These higher maxima in turn lead to lower numbers of P-vortices determined in the centre projection. In $SU(2)$, similar results have been obtained when seeking higher maxima by means of simulated annealing [161] and by pre-fixing to Landau gauge prior to MCG fixing [160]. As observed in $SU(2)$ [161, 162], there appears to be a significant anti-correlation between the value achieved in the gauge fixing functional and the percentage string tension reproduced by centre vortices.

As can be seen in Fig. 6.4, the ratio between the vortex-only string tension and the vortex density (simply the fraction of vortex plaquettes to total number of plaquettes) as a function of preconditioning is not independent of the preconditioning. Had it been independent one might conclude the reduction in the string tension is associated with simply not identifying all the vortices present. Either the mechanism with which vortices produce confinement is not entirely intact or the physical relevance of the vortices is not uniformly distributed.

In $SU(2)$, it was seen that smearing an $SU(2)$ configuration prior to MCG fixing reduced the centre projected string tension considerably [139]. It was argued there that this is because smearing greatly expands the vortex cores making the MCG process of collapsing them to pierce a single plaquette more difficult. A similar point was used to address the issue raised by prefixing to Landau gauge [160]. In principle the same position could be taken here, the generated preconditioning transformation may allow the vortex cores to be distributed across a larger number of lattice sites and again make

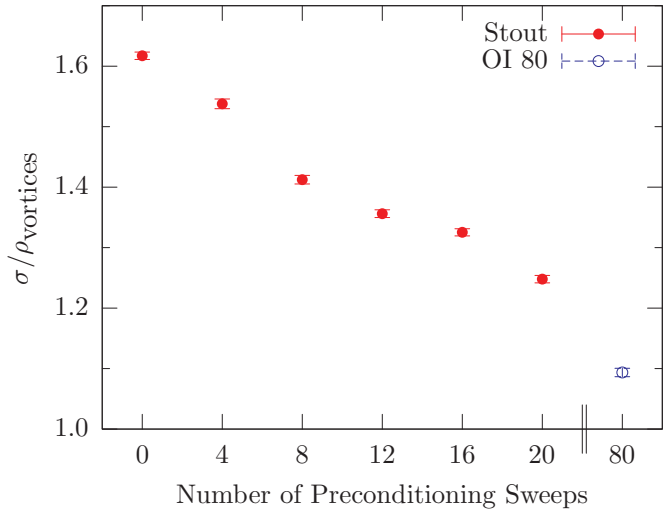

Figure 6.4: Ratio between the vortex-only string tension and the vortex density as a function of preconditioning.

the MCG task of compressing them more difficult. However, the over-improved stout-link smearing parameters are deliberately chosen to maintain the size of instantons and there is a case to say that if the link between centre vortices and topology seen in $SU(2)$ persists in $SU(3)$ then it should be possible to smear configurations without expanding the vortex cores. It is difficult to attribute the same vortex-expanding behaviour to the case of simulated annealing. However, the fact that known higher maxima exist (having these properties) and that simulated annealing is designed to locate them could explain the similar behaviour.

It is significant that much of the discussion in Ref. [150], where there is no Gribov ambiguity, can also be reconciled with the results found here. In this case a number of different Laplacian operators were constructed simply by using smeared links in the definition of the operator. There too it was seen that this caused an analogous effect on the vortex-only string tension. It was argued that the use of smearing caused the Laplacian to be blind to the short-range physics making the decomposition of the gauge field into the confining and non-confining components less effective — disorder in the vortex-only component is absorbed into the vortex-removed component resulting in a loss of string tension. It was contended there that in the continuum limit the smearing radius shrinks to zero, restoring the string tension.

In the same way, the smearing preconditioning may allow this effect to occur for MCG. That the locations of vortices as determined by both methods coincide serves to strengthen this position. Indeed, as discussed in Ref. [150], periodic boundary conditions cause gauge defects to have an opposite partner and, perhaps, the non-locality introduced by the preconditioning procedure may allow these opposites to annihilate producing no net defect after projection and a resultant drop in the vortex-only string tension.

6.4 Summary

The use of smearing as a preconditioning technique leads to higher maxima in the MCG gauge-fixing condition $V_U[\Omega]$. These higher maxima in turn lead to lower numbers of P-vortices determined in the centre projection and, subsequently, lower values of the vortex-only string tension.

Although the fundamental modular region of MCG would be an ideal candidate for a unique definition of vortex texture, it seems that the vortex matter arising from the first Gribov region as a whole has a greater phenomenological relevance. While all forms of preconditioning lead to a loss of string tension, it is the centre-projected physics that is not consistent. An improvement in $V_U[\Omega]$ causes one to miss vortices in the projection and spoil the phenomenology.

While MCG has proved successful to a large extent in $SU(2)$, what is different in $SU(3)$ is that centre-projection has never been shown to find enough vortices to reproduce the full string tension[1]. Indeed improving the gauge-fixing functional leads to fewer vortices and poor phenomenology. We conclude that MCG gauge-fixing does not provide evidence sufficient to explain the essential non-perturbative features of the QCD vacuum. Nevertheless, it would be informative to look for correlations between the locations of the determined P-vortices with each preconditioning since their removal still leads to a loss of string tension. The key discovery of this chapter is one of anticorrelation; the higher the gauge fixing functional, the worse the phenomenology picture.

[1]Apart from possibly vortices as determined via Laplacian gauge [150] in the continuum limit.

Chapter 7

Smeared overlap quark propagator

The content of this chapter is based on the publication: J. B. Zhang, P. J. Moran, P. O. Bowman, D. B. Leinweber, A. G. Williams and Phys. Rev. *D 80, 074503 (2009) [arXiv:0910.2781 [hep-lat]].*

In this chapter we study the properties of the momentum space quark propagator in Landau gauge, for the overlap quark action in quenched lattice QCD. Such an analysis is necessary because in Chapter 8 we intend to study the effect of dynamical quarks on the proton and Δ^+ electromagnetic form factors, and we must first choose an appropriate fermion action. Among the choices are smeared, or fat-link, fermion actions. We have done much work analysing smearing in the context of topology, but have not yet studied the effect of smearing on the propagation of quarks through the vacuum.

Numerical calculations are performed over four ensembles of gauge configurations, where three are smeared using either 1, 3, or 6 sweeps of stout-link smearing. We calculate the non-perturbative wave function renormalisation function $Z(p)$ and the non-perturbative mass function $M(p)$ for a variety of bare quark masses.

We find that the wave-function renormalisation function is slightly sensitive to the number of stout-link smearing sweeps. For the mass function we find the effect of the stout-link smearing algorithm to be small for moderate to light bare quark masses. For a heavy bare quark mass we find a strong dependence on the number of smearing sweeps.

7.1 Introduction

The quark propagator is one of the fundamental components of Quantum Chromodynamics (QCD). Although it is not a physical observable, many physical quantities are related to it. By studying the momentum-dependent quark mass function in the infrared region we can gain valuable insights into the mechanisms of dynamical chiral symmetry breaking and the associated dynamical generation of mass. At high momenta, one can also use the quark propagator to extract the running quark mass [174].

Lattice QCD techniques provide an avenue for the non-perturbative study of the quark propagator. There have been several lattice studies of the momentum space quark propagator [175–187] using different fermion actions. Finite volume effects and discretisation errors have also been extensively explored in lattice Landau gauge [186–189].

The overlap fermion formalism [30, 85] realises an exact chiral symmetry on the lattice and is automatically $\mathcal{O}(a)$ improved. There are many salient features of overlap fermions, which include no additive renormalisations to the quark masses, an index theorem linking the number of zero-modes of the Dirac operator to the topological charge Q, and evading the so called "no-go theorem" etc., however they are rather computationally demanding. There are many suggestions on how to reduce the computational cost. One such proposal is the use of a more elaborate kernel, together with a fattening of the gauge links [114, 124, 190].

The idea of any UV-filtered fermion action [22–26] is that one will carry out the calculation on a smoothed copy of the actual gauge field and evaluate the Dirac operator on that background. This yields a new fermion action which differs from the old one by terms which are both simultaneously *ultralocal* and *irrelevant*. The term "UV-filtered" indicates that such an action is less sensitive to the UV fluctuations of the gauge background. Sometimes, one also speaks of "fat-link" actions.

There is a great amount of freedom available when generating a smoothed copy of some gauge field. One needs to decide on the smoothing recipe (APE [68], HYP [70], stout-link [71], etc.), on the parameter ($\alpha^{\rm APE}, \alpha^{\rm HYP}_{1,2,3}, \alpha^{\rm SL} \equiv \rho$) and on the number of iterations, $n^{\rm iter}$. In any case, with fixed $(\alpha, n^{\rm iter})$ the filtered "fat-link" action is in the *same universality class* as the usual "thin-link" version [25]. Unfortunately, if any smoothing process is over-applied, some important properties of the theory are lost. Therefore, one needs to find a balance between the smoothing procedure, which will accelerate convergence of the quark operator inversion and improve the localisation properties, at the danger of losing important physics. Recently, Stephan Durr and collaborators [24–26] applied 1-3 sweeps stout-link smearing [71] to the lattice gauge configurations and analysed how this affected various physical quantities. They claim that it is safe to use 1-3 sweeps of standard stout-link smearing on the gauge configurations. More recently, 6 sweeps of stout-link smearing was used in the *Science* article exploring the hadron mass spectrum [106].

In this chapter, we investigate the momentum space quark propagator on quenched gauge configurations. We utilise both the original lattice configurations and also the configurations which are produced by one, three, and six sweeps of standard stout-link smearing respectively. We compare results across all four cases, in order to explore the effect of smearing on the quark propagator with different quark masses and different lattice momenta.

7.2 Overlap quark propagator

The massive overlap operator can be written as [191]

$$D(\mu) = \frac{1}{2}\left[1 + \mu + (1-\mu)\gamma_5 \epsilon(H_w)\right] , \tag{7.1}$$

where $H_w(x,y) = \gamma_5 D_w(x,y)$ is the Hermitian Wilson-Dirac operator, $\epsilon(H_w) = H_w/\sqrt{H_w^2}$ is the matrix sign function, and the dimensionless quark mass parameter μ is

$$\mu \equiv \frac{m^0}{2m_w} , \tag{7.2}$$

where m^0 is the bare quark mass and m_w is the Wilson quark mass which, in the free case, must lie in the range $0 < m_w < 2$.

The bare quark propagator in coordinate space is given by

$$S^{\text{bare}}(m^0) \equiv \tilde{D}_c^{-1}(\mu)\,, \tag{7.3}$$

where

$$\tilde{D}_c^{-1}(\mu) \equiv \frac{1}{2m_w}\tilde{D}^{-1}(\mu) \quad \text{and}$$

$$\tilde{D}^{-1}(\mu) \equiv \frac{1}{1-\mu}\left[D^{-1}(\mu) - 1\right]\,. \tag{7.4}$$

When all interactions are turned off, the inverse bare lattice quark propagator reduces to the tree-level version, and in momentum space is given by

$$(S^{(0)})^{-1}(p) \equiv i\left(\sum_\mu C_\mu^{(0)}(p)\gamma_\mu\right) + B^{(0)}(p)\,, \tag{7.5}$$

where p is lattice momentum. One can calculate $S^{(0)}(p)$ directly by setting all links to unity in coordinate space, doing the matrix inversion, and then taking its Fourier transform. It is then possible to identify the appropriate kinematic lattice momentum q directly from the definition

$$q_\mu \equiv C_\mu^{(0)}(p). \tag{7.6}$$

The form of $q_\mu(p_\mu)$ is shown and its analytic form given in Ref. [185]. Having identified the appropriate kinematical lattice momentum q, we can now define the bare lattice propagator as

$$S^{\text{bare}}(p) \equiv \frac{Z(p)}{i\not{q} + M(p)}. \tag{7.7}$$

This ensures that the free lattice propagator is identical to the free continuum propagator. Due to asymptotic freedom the lattice propagator will also take the continuum form at large momenta. In the gauge sector, this type of analysis dramatically improves the gluon propagator [192–195].

The two Lorentz invariants can then be obtained via

$$Z^{-1}(p) = \frac{1}{12iq^2}\text{tr}\{\not{q}S^{-1}(p)\}\,, \tag{7.8}$$

$$M(p) = \frac{Z(p)}{12}\text{tr}\{S^{-1}(p)\}\,. \tag{7.9}$$

Here $Z(p)$ is the wave-function renormalisation function and $M(p)$ is the mass function. The above equations imply that $Z(p)$ is directly dependent on our choice of momentum q, whilst $M(p)$ is not.

7.3 Simulation details

We work on $16^3 \times 32$ lattices, with gauge configurations created using a tadpole improved, plaquette plus rectangle (Lüscher-Weisz [80]) gauge action through the pseudo-heat-bath algorithm. The lattice spacing, $a = 0.093$ fm, is determined from the static quark

potential with a string tension of $\sqrt{\sigma} = 440$ MeV [196]. The number of configurations to be used for each ensemble in this study is 50. The first smeared ensemble is created by applying one sweep of stout-link smearing to the original configurations with a smearing parameter of $\rho = 0.10$. The second smeared ensemble is created using three sweeps of stout-smearing with the same value of α. We work in an $\mathcal{O}(a^2)$-improved Landau gauge, and fix the gauge using a Conjugate Gradient Fourier Acceleration [197] algorithm with an accuracy of $\theta \equiv \sum |\partial_\mu A_\mu(x)|^2 < 10^{-12}$. The improved gauge-fixing scheme was used to minimise gauge-fixing discretisation errors [198].

Our numerical calculation begins with an evaluation of the inverse of $D(\mu)$ on the unfixed gauge configurations, where $D(\mu)$ is defined in Eq. (7.1). We then calculate the quark propagator of Eq. (7.3) for each configuration and rotate it to the Landau gauge by using the corresponding gauge transformation matrices $\{G_i(x)\}$. We then take the ensemble average to obtain $S^{\text{bare}}(x, y)$. The discrete Fourier transformation is then applied to $S^{\text{bare}}(x, y)$ and the momentum-space bare quark propagator, $S^{\text{bare}}(p)$, is finally obtained.

We use the mean-field improved Wilson action in the overlap fermion kernel. The value $\kappa = 0.19163$ is used in the Wilson action, which provides $m_w a = 1.391$ for the Wilson regulator mass in the interacting case [185]. We calculate the overlap quark propagator for 15 bare quark masses on each ensemble by using a shifted Conjugate Gradient solver. The bare quark mass m^0 is defined by Eq. (7.2). In the calculation, we choose the mass parameter $\mu = 0.009$, 0.010, 0.012, 0.014, 0.016, 0.018, 0.021, 0.024, 0.030, 0.036, 0.045, 0.060, 0.075, 0.090, and 0.105. This choice of μ corresponds to bare quark masses, in physical units, of $m^0 = 53$, 59, 71, 82, 94, 106, 124, 142, 177, 212, 266, 354, 442, 531, and 620 MeV respectively.

The partial results for the mass function $M(p)$ and the wave-function renormalisation function $Z^{(\text{R})}(p) \equiv Z(\zeta; p)$ on a $16^3 \times 32$ lattice without any smearing in Landau gauge were reported in Ref. [187]. Here we focus on a comparison of the behaviour of the overlap fermion propagator when using different numbers of stout-link smearing sweeps. All data is cylinder cut [192, 193]. Statistical uncertainties are estimated via a second-order, single-elimination jackknife.

7.4 Results

In a standard lattice simulation, one begins by tuning the value of the input bare quark mass m^0 to give the desired renormalised quark mass, which is usually realised through the calculation of a physical observable. However, smearing a lattice configuration filters out the ultraviolet physics and the renormalisation of the mass will be different. To some extent, the effect is similar to that of an increase in the lattice spacing a. After smearing, the same input m^0 will therefore give a different renormalised quark mass. The input bare quark mass must then be re-tuned in order to reproduce the same physical behaviour as on the unsmeared configuration.

We wish to directly study how the quark propagator $S(p)$ is affected by smearing, through a calculation of the mass $M(p)$ and wave-renormalisation $Z(p)$ functions. In order to replicate the re-tuning procedure described above, we begin by first calculating $M(p)$ and $Z(p)$ for all values of m^0 listed previously, over all four types of configura-

tions. We then select a value of the bare quark mass m^0 to investigate, and force the mass functions $M(p)$ to agree at a given reference momentum, ζ. This is achieved by interpolating $M(p)$, for the smeared configurations, between neighbouring values of the bare quark masses, in order to determine the required effective bare quark mass. Any reasonable choice of ζ should suffice. By reasonable, we mean any point out of the far infrared (IR) or ultraviolet (UV) momentum regions, where lattice artifacts will spoil the results.

In comparing the renormalisation function, we first interpolate $Z(p)$ to the effective bare quark mass, obtaining $Z^{(\mathrm{I})}(p)$. We then multiplicatively renormalise $Z^{(\mathrm{I})}(p)$ to $Z^{(\mathrm{R})}(p) \equiv Z(\zeta, p)$, subject to $Z(\zeta, \zeta) = 1$.

We begin with a comparison of the functions $M(p)$ and $Z^{(\mathrm{R})}(p)$ for a small bare quark mass, with three choices of the reference momentum $\zeta = 2.0$, 3.9 and 6.0 GeV. The interpolated mass functions for the smallest bare quark mass $m^0 = 53$ MeV are given in Fig. 7.1. We note the significant reduction in the statistical error, even after a single sweep of smearing. For all choices of ζ, the mass functions display strong agreement over all four levels of smearing, with the only differences occurring in the most infrared points. For the function $Z^{(\mathrm{R})}(p)$ the effect of smearing is also subtle, however the link smearing does introduce a minor splitting in the UV region. This splitting leads to small differences in the lower momentum regions of $Z^{(\mathrm{R})}(p)$ when we select $\zeta = 6.0$ GeV.

Next we consider a moderate bare quark mass of 177 MeV, for which the functions $M(p)$ and $Z^{(\mathrm{R})}(p)$ are shown in Fig. 7.2. As in the case of a small bare quark mass, we find that the mass function appears independent of the choice of reference momentum, however the discrepancy at the most infrared point is no longer apparent. The renormalisation function displays the same splitting in the UV region. The effect of smearing on the quark propagator still appears to be relatively minor at this value of m^0.

Finally we consider a larger choice of the bare quark mass, $m^0 = 531$ MeV. A consideration of the mass functions $M(p)$ given in Fig. 7.3 reveals a strong dependence on the choice of reference momentum ζ. We see that a choice of either $\zeta = 3.9$, or 6.0 GeV leads to large discrepancies in both the low and moderate momentum regions. With a choice of $\zeta = 2.0$ GeV we are able to obtain agreement in the low momentum region.

The dependence of $M(p)$ on ζ indicates that the suppression of ultraviolet fluctuations by the smearing algorithm has spoilt the physics of the theory above $\sim 2-3$ GeV, for this value of m^0. These effects are clearly visible after just a single sweep of smearing at this heavy bare quark mass. We further note that in the case of 6 sweeps and $\zeta = 6.0$ GeV, the mass function drops to the bare quark mass. This is a clear indication that the Compton wavelength of the quark is small enough to reveal the void of short-distance interactions following 6 stout-link smearing sweeps.

The renormalisation functions $Z^{(\mathrm{R})}(p)$ for a heavy bare quark mass of $m^0 = 531$ MeV are also provided in Fig. 7.3. Apart from the small splitting in the UV region, $Z^{(\mathrm{R})}(p)$ still appears to be mostly unaffected by the smearing algorithm. In Fig. 7.4 we show the differences in $Z^{(\mathrm{R})}(p)$ between the smallest and largest bare quark masses, where in order to examine the UV splitting we choose $\zeta = 2.0$ GeV. Figure 7.4 shows that the magnitude of the splitting in $Z^{(\mathrm{R})}(p)$ introduced by the smearing algorithm is unaffected of the input bare quark mass.

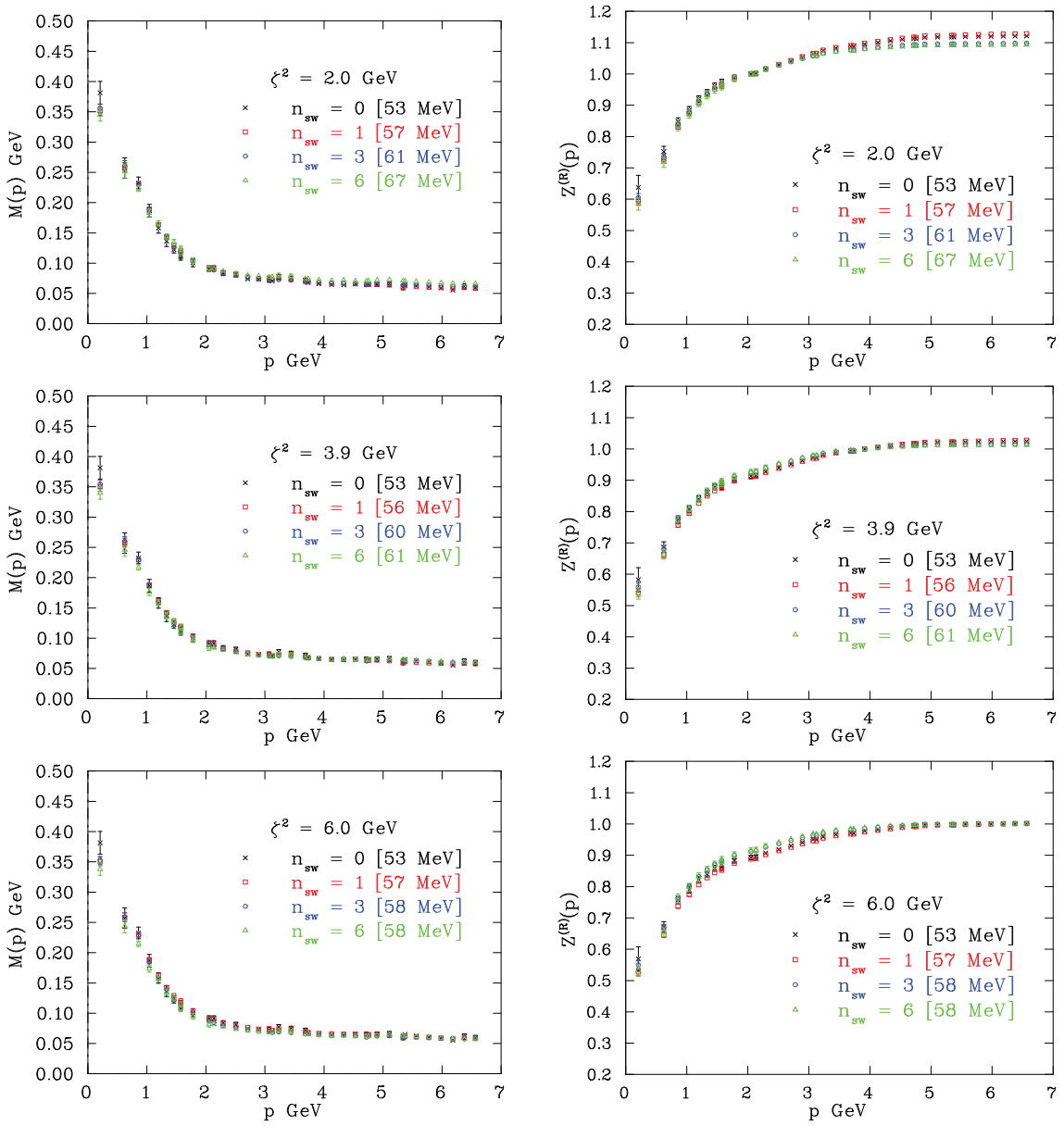

Figure 7.1: The interpolated mass $M(p)$ and renormalisation $Z^{(\mathrm{R})}(p)$ functions for the small bare quark mass, $m^0 = 53$ MeV, with three choices of ζ. The effective bare quark masses are given in square brackets. There is good agreement in $M(p)$ for all choices of ζ with up to six sweeps of stout-link smearing. A small splitting in the UV region of $Z^{(\mathrm{R})}(p)$ is apparent after three sweeps of smearing. This leads to a disagreement in $Z^{(\mathrm{R})}(p)$ for a large choice of $\zeta = 6.0$ GeV.

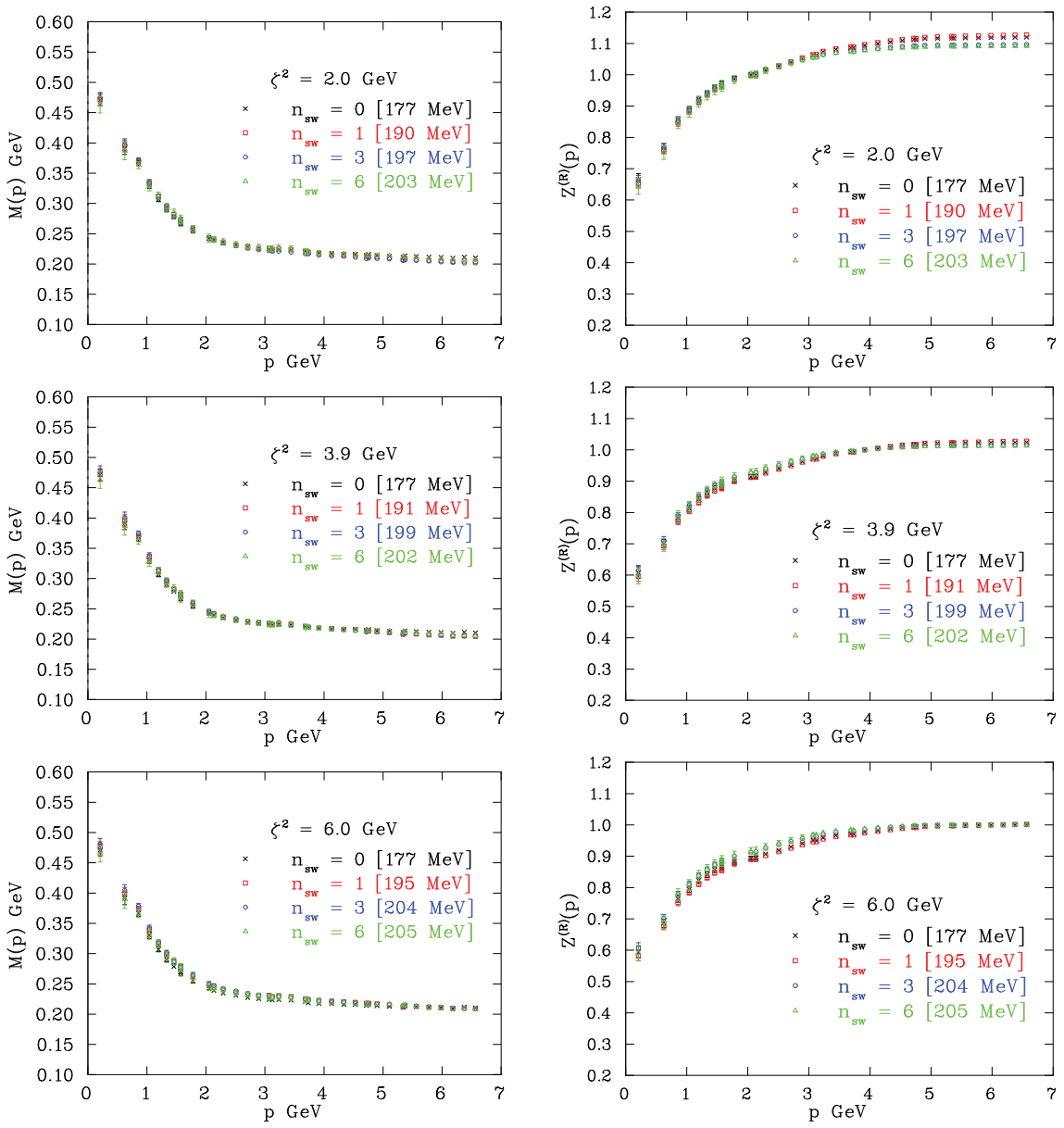

Figure 7.2: The interpolated mass $M(p)$ and renormalisation $Z^{(\mathrm{R})}(p)$ functions for the moderate bare quark mass, $m^0 = 177$ MeV, with the three choices of ζ. The effective bare quark masses are given in square brackets. As with the small bare quark mass, the mass function displays good agreement for all choices of ζ, and there is also a small splitting apparent in the UV region of $Z^{(\mathrm{R})}(p)$. We note that the differences in $Z^{(\mathrm{R})}(p)$ appear to be independent of the bare quark mass.

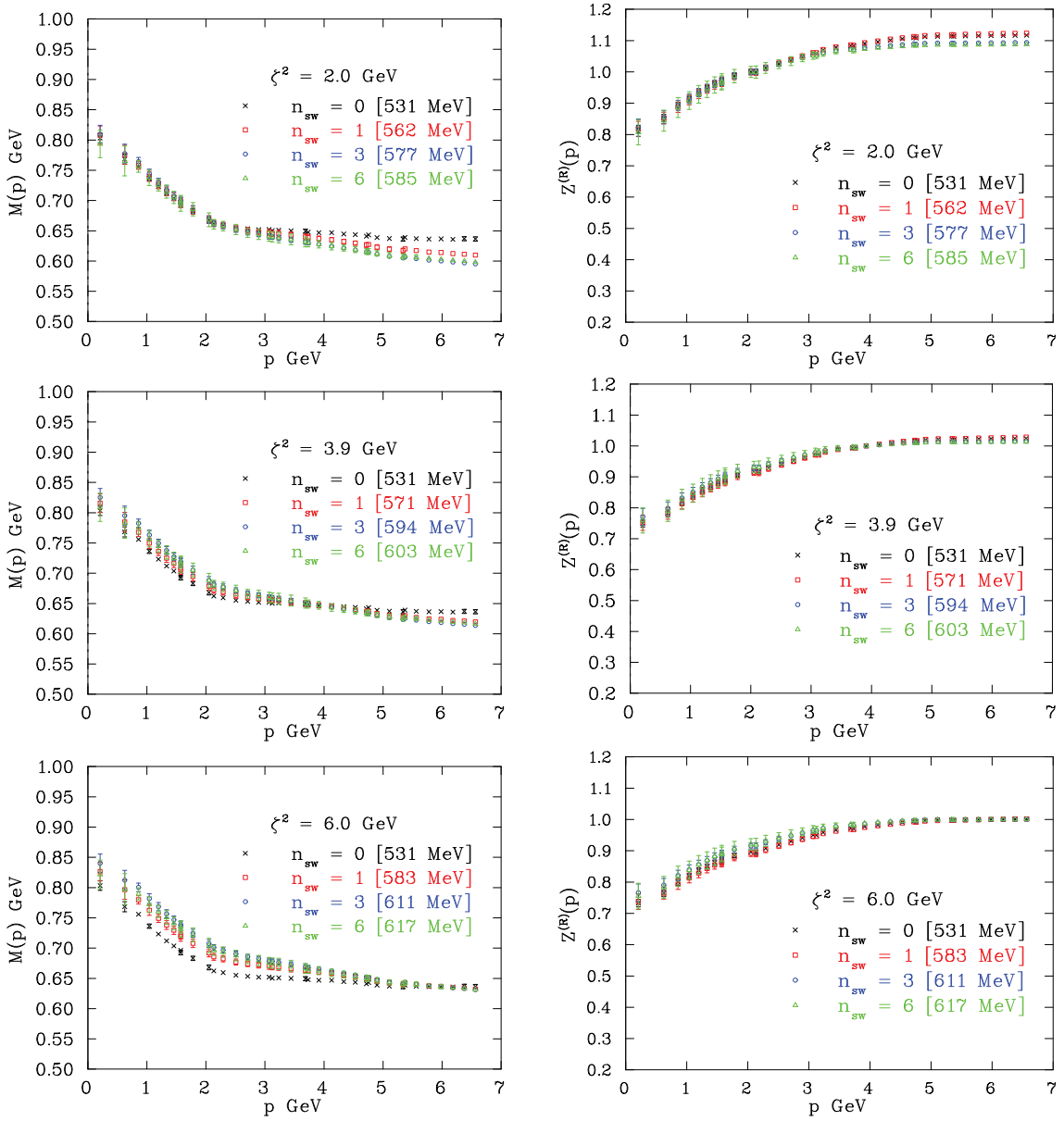

Figure 7.3: The interpolated mass $M(p)$ and renormalisation $Z^{(\mathrm{R})}(p)$ functions for the heavy bare quark mass, $m^0 = 531$ MeV, for the three choices of ζ. The effective bare quark masses are given in square brackets. We see that for this value of m^0, the choices $\zeta = 3.9$, and 6.0 GeV lead to large differences in the moderate and infrared momentum regions of $M(p)$. This indicates that the physics above approximately 3 GeV has been spoilt by the smearing algorithm. In $Z^{(\mathrm{R})}(p)$ we again find that the stout-link smearing algorithm introduces a small splitting in the infrared region.

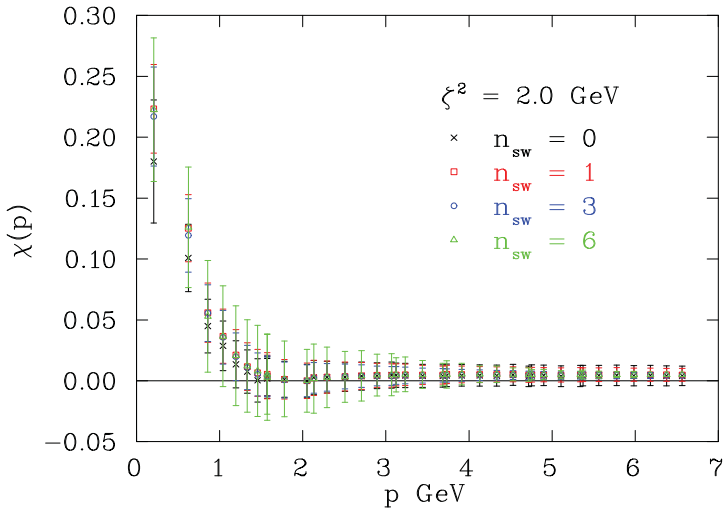

Figure 7.4: The difference $\chi(p) \equiv |Z^{(\mathrm{R})}_{\mathrm{light}}(p) - Z^{(\mathrm{R})}_{\mathrm{heavy}}(p)|$ between the renormalisation functions $Z^{(\mathrm{R})}(p)$ for the heavy and small bare quark masses considered previously, with $\zeta = 2.0$ GeV. We see that the difference rapidly approaches zero, indicating that the magnitude of the splitting introduced by the smearing algorithm is independent of the input bare quark mass. The differences at lower momenta are due to a flattening of $Z(p)$ as m^0 is increased.

7.5 Summary

The stout-link smearing procedure can save a large amount of compute time in the calculation of hadronic physics. Not only is the Dirac operator easier to invert but statistical errors are reduced significantly. The conclusion drawn from this study is that up to six sweeps of stout-link smearing sweeps induces rather small effects on the quark propagator for small and moderate bare quark masses, as claimed by Durr, et al. [24–26]. After an appropriate rescaling of the bare quark mass, the renormalised quark propagator displays the same physics as the untouched configuration. The only notable exceptions are order 2% discrepancies in the renormalisation function for all quark masses and the most infrared point of the lightest quark mass function. There an effect approaching 2σ is revealed.

These effects provide some evidence of a link between small topologically nontrivial gauge field configurations linked to dynamical chiral symmetry breaking through their production of approximate zero-modes in the Dirac operator. Upon smearing this short distance physics is modified. Certainly the effects are subtle. However, they may require further investigation in the event that fermion actions, in which all links of the action are smeared, become the action of choice for calculating the physics beyond the standard model.

Chapter 8

Magnetic moments in quenched and dynamical QCD

The formalism of this chapter follows that presented in the publication: S. Boinepalli, D. B. Leinweber, P. J. Moran, A. G. Williams, J. M. Zanotti and J. B. Zhang, Phys. Rev. D 80, 054505 (2009) [arXiv:0902.4046 [hep-lat]].

In Chapter 5 we directly examined the structure of the QCD vacuum to study the effects of including dynamical quarks. We demonstrated how the extra dynamical degrees of freedom lead to "rougher" gauge fields containing a greater density of instanton-like objects.

We now extend this analysis to examine the effects of dynamical quarks on the electromagnetic properties of baryons through calculations of the nucleon and Δ magnetic moments. The absence of strange valence quarks in these baryons makes them particularly suited for studies of chiral physics, where the effects of dynamical quarks will be greatest. We focus on the magnetic moments of the proton and Δ^+ and compare μ_{Δ^+}/μ_p between quenched and dynamical lattice simulations. In line with expectations, we find that the differences in vacuum structure lead to a significant and important change in the chiral curvature, following the inclusion of dynamical quarks.

8.1 Introduction

The study of the electromagnetic properties of baryons provides valuable insight into the non-perturbative structure of QCD (see Refs. [199–203] for reviews). Baryon charge radii and magnetic moments provide an excellent opportunity to observe the non-analytic quark-mass behaviour predicted by chiral effective field theory (χEFT). Since these are inherently non-perturbative properties of hadrons, first-principles calculations on the lattice are essential for our understanding of hadronic structure, and indeed there has been much progress in this direction, mainly for the nucleon and pseudoscalar states (see [204] for a review).

On the lattice, decuplet baryons are stable as a result of the unphysical large quark masses that are used in present calculations and the finite volume of the lattice. Decay to a pion and an octet baryon is forbidden by energy conservation. However, stability

of decuplet baryons is common to most hadronic models. In this sense, lattice results provide a useful forum in which the strengths and weaknesses of various models may be identified.

In a recent calculation, we examined the decuplet baryon form factors using quenched QCD [205]. The results were compared with experimental measurements where available, and with the predictions of Quenched Chiral Perturbation Theory (QχPT). Of particular interest was an observed turn over in the magnetic moment of the Δ^+ baryon as the chiral regime was approached. As will be explained, this chiral behaviour is due to the presence of the $\Delta \to N\pi$ decay channel. What was not done in Ref. [205] was a comparison of the Δ magnetic moment in the quenched approximation with that in full dynamical QCD.

This chapter is organised as follows. The octet and decuplet baryon interpolating fields used in the correlation functions are discussed in Sec. 8.2.1. The extraction of baryon mass and electromagnetic form factors proceeds through a calculation of two and three-point correlation functions. These are discussed in Sec. 8.2.2. The two and three point functions for the proton and Δ^+ are discussed in Secs. 8.2.3 and 8.2.4. Our methods for extracting quark sector contributions and magnetic moments are detailed in Secs. 8.2.5 and 8.2.6. Throughout this analysis we employ the lattice techniques introduced in Ref. [206], and these are summarised in Sec. 8.3. Our expectations for the calculation are then discussed in Sec. 8.4, before presenting an overview of the quenched results in Sec. 8.5. The dynamical results are presented and discussed in Sec. 8.6, and summarised in Sec. 8.7.

8.2 Theoretical formalism

8.2.1 Interpolating fields

The commonly used interpolating field for exciting the Δ^{++} resonance from the QCD vacuum takes the long established [207, 208] form of

$$\chi_\mu^{\Delta^{++}}(x) = \epsilon^{abc} \left(u^{Ta}(x) C\gamma_\mu u^b(x)\right) u^c(x). \tag{8.1}$$

Unless otherwise noted, we follow the notation of Sakurai[1] [6]. The Dirac gamma matrices are Hermitian and satisfy $\{\gamma_\mu, \gamma_\nu\} = 2\,\delta_{\mu\nu}$, with $\sigma_{\mu\nu} = \frac{1}{2i}\,[\gamma_\mu, \gamma_\nu]$. $C = \gamma_4\gamma_2$ is the charge conjugation matrix, a, b, c are colour indices, $u(x)$ is a u-quark field, and the superscript T denotes transpose. The generalisation of this interpolating field for the Δ^+ composed of two u quarks and one d quark has the form

$$\chi_\mu^{\Delta^+}(x) = \frac{1}{\sqrt{3}}\,\epsilon^{abc}\Big[2\left(u^{Ta}(x) C\gamma_\mu d^b(x)\right) u^c(x) + \left(u^{Ta}(x) C\gamma_\mu u^b(x)\right) d^c(x)\Big]. \tag{8.2}$$

To access the proton we use the interpolating field,

$$\chi^{p+}(x) = \epsilon^{abc} \left(u^{Ta}(x) C\gamma_5 d^b(x)\right) u^c(x)\,. \tag{8.3}$$

[1] Useful properties of the Dirac gamma matrices are provided in App. B.

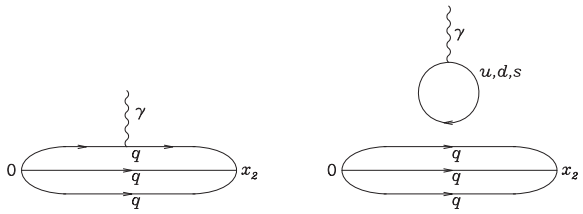

Figure 8.1: Diagrams illustrating the two topologically different insertions of the current within the framework of lattice QCD.

The neutron interpolating field can be obtained via the exchange $u \leftrightarrow d$. Other octet and decuplet baryon interpolating fields can be obtained with the appropriate substitutions of $u(x),\ d(x) \ \rightarrow \ u(x),\ d(x)$ or $s(x)$ in Eqs. (8.2) and (8.3). The general form of a baryon interpolating field is derived in App. C.

8.2.2 Correlation functions

Two-point correlation functions at the quark level are obtained through the standard procedure of contracting pairs of quark fields. Considering the Δ^+ correlation function at the quark level and performing all possible quark field contractions gives the two-point function as

$$\begin{aligned}\left\langle T\left(\chi_\mu^{\Delta^+}(x)\overline{\chi}_\nu^{\Delta^+}(0)\right)\right\rangle = \frac{1}{3}\,\epsilon^{abc}\epsilon^{a'b'c'}\Big\{ & \\ 4S_u^{aa'}\,\gamma_\nu\,C S_u^{Tbb'}C\,\gamma_\mu\,S_d^{cc'} + 2S_u^{aa'}\,\mathrm{tr}\left[\gamma_\nu\,C S_u^{Tbb'}C\,\gamma_\mu\,S_d^{cc'}\right] & \\ + 4S_u^{aa'}\,\gamma_\nu\,C S_d^{Tbb'}C\,\gamma_\mu\,S_u^{cc'} + 2S_u^{aa'}\,\mathrm{tr}\left[\gamma_\nu\,C S_d^{Tbb'}C\,\gamma_\mu\,S_u^{cc'}\right] & \\ + 4S_d^{aa'}\,\gamma_\nu\,C S_u^{Tbb'}C\,\gamma_\mu\,S_u^{cc'} + 2S_d^{aa'}\,\mathrm{tr}\left[\gamma_\nu\,C S_u^{Tbb'}C\,\gamma_\mu\,S_u^{cc'}\right]\Big\}, &\end{aligned} \tag{8.4}$$

where the quark-propagator $S_u^{aa'} = T\left(u^a(x)\overline{u}^{a'}(0)\right)$ and similarly for the other quark flavors. $SU(3)_{\text{flavor}}$ symmetry is clearly displayed in this equation. For the proton one finds,

$$\begin{aligned}\left\langle T\left(\chi^p(x)\overline{\chi}^p(0)\right)\right\rangle = -\epsilon^{abc}\epsilon^{a'b'c'}\Big\{ & \\ S_u^{aa'}\,\gamma_5\,C S_d^{Tbb'}C\,\gamma_5\,S_u^{cc'} + S_u^{aa'}\,\mathrm{tr}\left[\gamma_5\,C S_d^{Tbb'}C\,\gamma_5\,S_u^{cc'}\right]\Big\}. &\end{aligned} \tag{8.5}$$

In determining the three point function, one encounters two topologically different ways of performing the current insertion. Figure 8.1 displays skeleton diagrams for these two insertions. These diagrams may be dressed with an arbitrary number of gluons. Diagram (a) illustrates the connected insertion of the current to one of the valence quarks of the baryon. Diagram (b) accounts for the alternative time ordering where the current first produces a disconnected $q\,\overline{q}$ pair which in turn interacts with the valence quarks of the baryon via gluons.

The number of terms in the three-point function is four times that in Eq. (8.4). The

correlation function relevant for a Δ^+ three-point function is

$$
\begin{aligned}
T\left(\chi_\mu^{\Delta^+}(x_2)\, j^\alpha(x_1)\, \overline{\chi}_\nu^{\Delta^+}(0)\right) = \frac{1}{3}\,\epsilon^{abc}\epsilon^{a'b'c'}\Big\{ \\
&4\widehat{S}_u^{aa'}\,\gamma_\nu\, C S_u^{Tbb'} C\,\gamma_\mu\, S_d^{cc'} + 4\widehat{S}_u^{aa'}\,\gamma_\nu\, C S_d^{Tbb'} C\,\gamma_\mu\, S_u^{cc'} + 4\widehat{S}_d^{aa'}\,\gamma_\nu\, C S_u^{Tbb'} C\,\gamma_\mu\, S_u^{cc'} \\
+\,&4S_u^{aa'}\,\gamma_\nu\, C \widehat{S}_u^{Tbb'} C\,\gamma_\mu\, S_d^{cc'} + 4S_d^{aa'}\,\gamma_\nu\, C \widehat{S}_u^{Tbb'} C\,\gamma_\mu\, S_u^{cc'} + 4S_u^{aa'}\,\gamma_\nu\, C \widehat{S}_d^{Tbb'} C\,\gamma_\mu\, S_u^{cc'} \\
+\,&4S_u^{aa'}\,\gamma_\nu\, C S_d^{Tbb'} C\,\gamma_\mu\, \widehat{S}_u^{cc'} + 4S_d^{aa'}\,\gamma_\nu\, C S_u^{Tbb'} C\,\gamma_\mu\, \widehat{S}_u^{cc'} + 4S_u^{aa'}\,\gamma_\nu\, C S_u^{Tbb'} C\,\gamma_\mu\, \widehat{S}_d^{cc'} \\
+\,&2\widehat{S}_u^{aa'}\,\mathrm{tr}\left[\gamma_\nu\, C S_u^{Tbb'} C\,\gamma_\mu\, S_d^{cc'}\right] + 2\widehat{S}_u^{aa'}\,\mathrm{tr}\left[\gamma_\nu\, C S_d^{Tbb'} C\,\gamma_\mu\, S_u^{cc'}\right] + 2\widehat{S}_d^{aa'}\,\mathrm{tr}\left[\gamma_\nu\, C S_u^{Tbb'} C\,\gamma_\mu\, S_u^{cc'}\right] \\
+\,&2S_u^{aa'}\,\mathrm{tr}\left[\gamma_\nu\, C \widehat{S}_u^{Tbb'} C\,\gamma_\mu\, S_d^{cc'}\right] + 2S_d^{aa'}\,\mathrm{tr}\left[\gamma_\nu\, C \widehat{S}_u^{Tbb'} C\,\gamma_\mu\, S_u^{cc'}\right] + 2S_u^{aa'}\,\mathrm{tr}\left[\gamma_\nu\, C \widehat{S}_d^{Tbb'} C\,\gamma_\mu\, S_u^{cc'}\right] \\
+\,&2S_u^{aa'}\,\mathrm{tr}\left[\gamma_\nu\, C S_d^{Tbb'} C\,\gamma_\mu\, \widehat{S}_u^{cc'}\right] + 2S_d^{aa'}\,\mathrm{tr}\left[\gamma_\nu\, C S_u^{Tbb'} C\,\gamma_\mu\, \widehat{S}_u^{cc'}\right] + 2S_u^{aa'}\,\mathrm{tr}\left[\gamma_\nu\, C S_u^{Tbb'} C\,\gamma_\mu\, \widehat{S}_d^{cc'}\right]\Big\} \\
+\,&\sum_{q=u,\,d,\,s} e_q \sum_i \mathrm{tr}\left[S_q^{ii}(x_1,x_1)\,\gamma_\mu\right]\frac{1}{3}\,\epsilon^{abc}\epsilon^{a'b'c'}\Big\{ \\
&4S_u^{aa'}\,\gamma_\nu\, C S_u^{Tbb'} C\,\gamma_\mu\, S_d^{cc'} + 4S_u^{aa'}\,\gamma_\nu\, C S_d^{Tbb'} C\,\gamma_\mu\, S_u^{cc'} + 4S_d^{aa'}\,\gamma_\nu\, C S_u^{Tbb'} C\,\gamma_\mu\, v S_u^{cc'} \\
+\,&2S_u^{aa'}\,\mathrm{tr}\left[\gamma_\nu\, C S_u^{Tbb'} C\,\gamma_\mu\, S_d^{cc'}\right] + 2S_u^{aa'}\,\mathrm{tr}\left[\gamma_\nu\, C S_d^{Tbb'} C\,\gamma_\mu\, S_u^{cc'}\right] + 2S_d^{aa'}\,\mathrm{tr}\left[\gamma_\nu\, C S_u^{Tbb'} C\,\gamma_\mu\, S_u^{cc'}\right]\Big\},
\end{aligned}
\tag{8.6}
$$

where

$$
\widehat{S}_q^{aa'}(x_2,x_1,0) = e_q \sum_i S_q^{ai}(x_2,x_1)\,\gamma_\alpha\, S_q^{ia'}(x_1,0)\,, \tag{8.7}
$$

denotes the connected insertion of the probing current to a quark of charge e_q. Note that here we have explicitly selected the electromagnetic current. However, the present discussion may be generalised to any quark-field-based current operator bilinear in the quark fields.

The latter term of Eq. (8.6) accounts for the disconnected quark loop contribution depicted in Fig. 8.1b. The sum over the quarks running around the loop has been restricted to the flavors relevant to the ground state baryon octet and decuplet. In the $SU(3)_{\text{flavor}}$ limit the sum vanishes for the electromagnetic current. However, the heavier strange quark mass allows for a nontrivial result. Due to the technical difficulties of numerically estimating M^{-1} for the squared lattice volume of diagonal spatial indices, these contributions have been omitted from lattice QCD calculations of electromagnetic structure in the spirit of QχPT, and we will also do so here. For other observables such as the scalar density or forward matrix elements of the axial vector current relevant to the spin of the baryon, the "charges" running around the loop do not sum to zero. In this case the second term of Eq. (8.6) can be just as significant as the connected term [209, 210].

An examination of Eq. (8.6) reveals complete symmetry among the quark flavors in the correlation function. For example, wherever a d quark appears in the correlator, a u quark also appears in the same position in another term. An interesting consequence of this is that the connected insertion of the electromagnetic current for Δ^0 vanishes. All electromagnetic properties of the Δ^0 have their origin strictly in the disconnected loop contribution. Physically, what this means is that the valence wave function for each of the quarks in the Δ resonances are identical under charge symmetry. This is in contrast

to the proton for which one finds (neglecting the disconnected quark loop insertion),

$$\begin{aligned}\left\langle T\left(\chi^p(x)\overline{\chi}^p(0)\right)\right\rangle = -\epsilon^{abc}\epsilon^{a'b'c'}\Big\{ & \\ & \widehat{S}_u^{aa'}\,\gamma_5\,C S_d^{Tbb'} C\,\gamma_5\,S_u^{cc'} + \widehat{S}_u^{aa'}\,\mathrm{tr}\left[\gamma_5\,C S_d^{Tbb'} C\,\gamma_5\,S_u^{cc'}\right]\Big\} \\ & S_u^{aa'}\,\gamma_5\,C \widehat{S}_d^{Tbb'} C\,\gamma_5\,S_u^{cc'} + S_u^{aa'}\,\mathrm{tr}\left[\gamma_5\,C \widehat{S}_d^{Tbb'} C\,\gamma_5\,S_u^{cc'}\right]\Big\} \\ & S_u^{aa'}\,\gamma_5\,C S_d^{Tbb'} C\,\gamma_5\,\widehat{S}_u^{cc'} + S_u^{aa'}\,\mathrm{tr}\left[\gamma_5\,C S_d^{Tbb'} C\,\gamma_5\,\widehat{S}_u^{cc'}\right]\Big\}.\end{aligned} \tag{8.8}$$

Here we see that there the symmetry between different quark flavours appearing in the correlation function is no longer present. Thus, the contribution from the u-quark, to the connected insertion of the electromagnetic current, will differ to that of the d-quark contribution.

8.2.3 Two-point Green functions

In this and the following subsection discussing correlation functions at the hadronic level, the Dirac representation of the γ-matrices is used to facilitate calculations of the γ-matrix algebra. It is then a simple task to account for the differences in γ-matrix and metric definitions in reporting the final results using Sakurai's notation.

The extraction of baryon masses and electromagnetic form factors proceeds through the calculation of the ensemble average (denoted $\langle\, \cdots \,\rangle$) of two and three-point Green functions. The two-point function for octet baryons is defined as

$$\left\langle\, G^{BB}(t;\vec{p};\Gamma)\,\right\rangle = \sum_{\vec{x}} e^{-i\vec{p}\cdot\vec{x}}\Gamma^{\beta\alpha}\left\langle\, \Omega \,\middle|\, T\left(\chi^\alpha(x)\overline{\chi}^\beta(0)\right) \,\middle|\, \Omega\,\right\rangle\,. \tag{8.9}$$

Here Ω represents the QCD vacuum, Γ is a 4×4 matrix in Dirac space and α, β are Dirac indices. At the hadronic level one proceeds by inserting a complete set of states $\left|\, B,p,s\,\right\rangle$ and defining

$$\left\langle\, \Omega \,\middle|\, \chi(0) \,\middle|\, B,p,s\,\right\rangle = Z_B(p)\sqrt{\frac{M}{E_p}}\,u(p,s)\,, \tag{8.10}$$

where Z_B represents the coupling strength of $\chi(0)$ to the baryon B. Our use of smeared interpolators makes this momentum dependent. Momentum is denoted by p, spin by s, and $u(p,s)$ is a Dirac spinor. $E_p = \sqrt{\vec{p}^2 + M^2}$ and Dirac indices have been suppressed. Using the Dirac spin-sum,

$$\sum_s u(p,s)\overline{u}(p,s) = \frac{(\gamma\cdot p + M)}{2M}\,, \tag{8.11}$$

and $\vec{p} = (p,0,0)$, the large Euclidean time limit of the two point function takes the form

$$\left\langle\, G^{BB}(t;\vec{p},\Gamma)\,\right\rangle = \frac{Z_B(p)\overline{Z}_B(p)}{2E_p}e^{-E_p t}\,\mathrm{tr}\left[\Gamma(-i\gamma\cdot p + M)\right]\,. \tag{8.12}$$

Here $\overline{Z_B}(p)$ denotes the overlap associated with our smeared source. $Z_B(p)$ is associated with the sink which need not have the same smearing. With the usual definitions for Γ,

$$\Gamma_j = \frac{1}{2}\begin{pmatrix} \sigma_j & 0 \\ 0 & 0 \end{pmatrix} \quad , \quad \Gamma_4 = \frac{1}{2}\begin{pmatrix} I & 0 \\ 0 & 0 \end{pmatrix}, \tag{8.13}$$

selecting $\Gamma \equiv \Gamma_4$ in Eq. (8.12) allows one to extract the mass of an even parity octet baryon.

For decuplet baryons the two-point function is defined as

$$\left\langle\, G^{BB}_{\sigma\tau}(t;\vec{p};\Gamma)\,\right\rangle = \sum_{\vec{x}} e^{-i\vec{p}\cdot\vec{x}}\Gamma^{\beta\alpha}\left\langle\, \Omega \,\middle|\, T\left(\chi^{\alpha}_{\sigma}(x)\overline{\chi}^{\beta}_{\tau}(0)\right) \,\middle|\, \Omega\,\right\rangle, \tag{8.14}$$

where the subscripts σ, τ are the Lorentz indices of the spin-3/2 interpolating fields. Once again we proceed by inserting a complete set of states,

$$\left\langle\, \Omega \,\middle|\, \chi_{\sigma}(0) \,\middle|\, B,p,s\,\right\rangle = Z_B(p)\sqrt{\frac{M}{E_p}}\,u_{\sigma}(p,s)\,, \tag{8.15}$$

where we now define $u_{\alpha}(p,s)$ to be a spin-vector in the Rarita-Schwinger formalism. So, this time using the Rarita-Schwinger spin sum,

$$\begin{aligned}\sum_s u_{\sigma}(p,s)\overline{u}_{\tau}(p,s) = & -\frac{\gamma\cdot p + M}{2M}\left\{g_{\sigma\tau} - \frac{1}{3}\gamma_{\sigma}\gamma_{\tau} - \frac{2p_{\sigma}p_{\tau}}{3M^2} + \frac{p_{\sigma}\gamma_{\tau} - p_{\tau}\gamma_{\sigma}}{3M}\right\}, \\ & \equiv \Lambda_{\sigma\tau}\,,\end{aligned} \tag{8.16}$$

the large Euclidean time limit of the two point function takes the form

$$\left\langle\, G^{BB}_{\sigma\tau}(t;\vec{p},\Gamma_4)\,\right\rangle = Z_B(p)\overline{Z}_B(p)\frac{M}{E_p}e^{-E_p t}\,\mathrm{tr}\left[\,\Gamma_4\,\Lambda_{\sigma\tau}\,\right], \tag{8.17}$$

where

$$\left\langle\, G^{BB}_{00}(t;\vec{p},\Gamma_4)\,\right\rangle = Z_B(p)\overline{Z_B}(p)\,\frac{2}{3}\,\frac{|\vec{p}|^2}{M_B^2}\left(\frac{E_p + M_B}{2E_p}\right)e^{-E_p t}, \tag{8.18}$$

$$\left\langle\, G^{BB}_{11}(t;\vec{p},\Gamma_4)\,\right\rangle = Z_B(p)\overline{Z_B}(p)\,\frac{2}{3}\,\frac{E_p^2}{M_B^2}\left(\frac{E_p + M_B}{2E_p}\right)e^{-E_p t}, \tag{8.19}$$

$$\left\langle\, G^{BB}_{22}(t;\vec{p},\Gamma_4)\,\right\rangle = Z_B(p)\overline{Z_B}(p)\,\frac{2}{3}\left(\frac{E_p + M_B}{2E_p}\right)e^{-E_p t}, \tag{8.20}$$

$$\left\langle\, G^{BB}_{33}(t;\vec{p},\Gamma_4)\,\right\rangle = Z_B(p)\overline{Z_B}(p)\,\frac{2}{3}\left(\frac{E_p + M_B}{2E_p}\right)e^{-E_p t}. \tag{8.21}$$

Equations (8.18) through (8.21) provide four correlation functions from which a decuplet baryon mass may be extracted. All masses extracted from the different selections of Lorentz indices agree within statistical uncertainties, and different indices may be added together to reduce statistical fluctuations.

It should be noted that the spin-3/2 interpolating field also has overlap with spin-1/2 baryons, however for the Δ baryons this poses no problem as these baryons are the lowest lying baryons in the mass spectrum having the appropriate isospin and strangeness quantum numbers.

8.2.4 Three-point functions and multipole form factors

Here we begin with a brief overview of the results of Refs. [211] and [212], for octet and decuplet baryons respectively, where the multipole form factors are defined in terms of the current matrix elements. In a manner similar to that for the two-point function, the three-point Green function for the spin-1/2 octet baryons is defined as

$$\begin{aligned} \left\langle\, G^{Bj^\mu B}(t_2,t_1;\vec{p}\,',\vec{p};\Gamma)\,\right\rangle = & \sum_{\vec{x_2},\vec{x_1}} e^{-i\vec{p}\,'\cdot\vec{x_2}} e^{+i(\vec{p}\,'-\vec{p})\cdot\vec{x_1}} \Gamma^{\beta\alpha} \\ & \times \left\langle\, \Omega \,\middle|\, T\left(\chi^\alpha(x_2) j^\mu(x_1) \overline{\chi}^\beta(0)\right) \,\middle|\, \Omega \,\right\rangle . \end{aligned} \tag{8.22}$$

For large Euclidean time separations, $t_2 - t_1 >> 1$ and $t_1 >> 1$, the three-point function is dominated by the contribution from the ground state and becomes

$$\begin{aligned} \left\langle\, G^{Bj^\mu B}(t_2,t_1;\vec{p}\,',\vec{p};\Gamma)\,\right\rangle = & \sum_{s,s'} e^{-E_{p'}(t_2-t_1)} e^{-E_p t_1} \Gamma^{\beta\alpha} \\ & \times \left\langle\, \Omega \,\middle|\, \chi^\alpha \,\middle|\, p',s' \,\right\rangle \left\langle\, p',s' \,\middle|\, j^\mu \,\middle|\, p,s \,\right\rangle \left\langle\, p,s \,\middle|\, \overline{\chi}^\beta \,\middle|\, \Omega \,\right\rangle , \end{aligned} \tag{8.23}$$

The matrix element of the electromagnetic current has the general form,

$$\left\langle\, p',s' \,\middle|\, j^\mu \,\middle|\, p,s \,\right\rangle = \sqrt{\frac{M^2}{E_p E_{p'}}}\, \overline{u}(p',s') \left(F_1(q^2)\gamma^\mu - F_2(q^2)\sigma^{\mu\nu}\frac{q^\nu}{2M} \right) u(p,s) , \tag{8.24}$$

where p and p' (s and s') denote the momentum (spin) of the initial and final states respectively, $q = p' - p$ and $u(p,s)$ denotes a Dirac spinor.

The time dependence of the three-point function may be eliminated through the use of the two-point functions. Maintaining the lattice Ward identity, which guarantees the lattice electric form factor reproduces the total charge of the baryon at $q^2 = 0$, provides an indispensable guide to the optimum ratio of Green functions. The preferred ratio of two- and three-point Green functions is [206]

$$R^\mu(t_2,t_1;\vec{p}\,',\vec{p};\Gamma) = \left(\frac{\left\langle\, G^{Bj^\mu B}(t_2,t_1;\vec{p}\,',\vec{p};\Gamma)\,\right\rangle \left\langle\, G^{Bj^\mu B}(t_2,t_1;\vec{p},\vec{p}\,';\Gamma)\,\right\rangle}{\left\langle\, G^{BB}(t_2;\vec{p}\,';\Gamma_4)\,\right\rangle \left\langle\, G^{BB}(t_2;\vec{p};\Gamma_4)\,\right\rangle} \right)^{1/2} \tag{8.25}$$

$$\simeq \left(\frac{E_p + M}{2E_p} \right)^{1/2} \left(\frac{E_{p'} + M}{2E_{p'}} \right)^{1/2} \overline{R}^\mu(\vec{p}\,',\vec{p};\Gamma) , \tag{8.26}$$

where we have defined the reduced ratio $\overline{R}^\mu(\vec{p}\,',\vec{p};\Gamma)$. Note that in contrast to Refs. [205, 206, 213] which used,

$$R^\mu(t_2,t_1;\vec{p}\,',\vec{p};\Gamma) = \left(\frac{\left\langle\, G^{Bj^\mu B}(t_2,t_1;\vec{p}\,',\vec{p};\Gamma)\,\right\rangle \left\langle\, G^{Bj^\mu B}(t_2,t_1;-\vec{p},-\vec{p}\,';\Gamma)\,\right\rangle}{\left\langle\, G^{BB}(t_2;\vec{p}\,';\Gamma_4)\,\right\rangle \left\langle\, G^{BB}(t_2;-\vec{p};\Gamma_4)\,\right\rangle} \right)^{1/2} , \tag{8.27}$$

we prefer a symmetric momentum combination when forming the ratio of correlation functions. The symmetric combination in Eq. (8.25) provides an exact cancellation of the momentum-dependent $Z_B(p)$ factors, and results in smaller statistical errors[2].

[2]However we note that after including the U^* trick (discussed later), the statistical errors from both approaches are exactly equal (see App. E).

With the reduced ratio defined, the Sachs forms for the electromagnetic form factors,

$$\begin{aligned} \mathcal{G}_E(q^2) &= F_1(q^2) - \frac{q^2}{(2M)^2} F_2(q^2)\,, \\ \mathcal{G}_M(q^2) &= F_1(q^2) + F_2(q^2)\,, \end{aligned} \tag{8.28}$$

can be extracted by making appropriate choices for Γ. A straightforward calculation reveals,

$$\begin{aligned} \mathcal{G}_E(q^2) &= \overline{R}^4(\vec{q}\,', \vec{0}; \Gamma_4)\,, \\ |\epsilon_{ijk} q^i|\, \mathcal{G}_M(q^2) &= (E_q + M)\, \overline{R}^k(\vec{q}\,', \vec{0}; \Gamma_j)\,, \\ |q^k|\, \mathcal{G}_E(q^2) &= (E_q + M)\, \overline{R}^k(\vec{q}\,', \vec{0}; \Gamma_4)\,. \end{aligned} \tag{8.29}$$

For the decuplet baryons we proceed in much the same way. For large Euclidean time separations the relevant three-point correlation function takes the form,

$$\begin{aligned} \left\langle\, G^{Bj^\mu B}_{\sigma\tau}(t_2, t_1; \vec{p}\,', \vec{p}; \Gamma)\, \right\rangle = & \sum_{s,s'} e^{-E_{p'}(t_2 - t_1)} e^{-E_p t_1} \Gamma^{\beta\alpha} \\ & \times \left\langle\, \Omega \,\middle|\, \chi^\alpha_\sigma \,\middle|\, p', s' \,\right\rangle \left\langle\, p', s' \,\middle|\, j^\mu \,\middle|\, p, s \,\right\rangle \left\langle\, p, s \,\middle|\, \overline{\chi}^\beta_\tau \,\middle|\, \Omega \,\right\rangle, \end{aligned} \tag{8.30}$$

where σ and τ label the Lorentz indices. The electromagnetic current matrix element for spin-3/2 particles may be written as

$$\left\langle\, p', s' \,\middle|\, j^\mu(0) \,\middle|\, p, s \,\right\rangle = \sqrt{\frac{M_B^2}{E_p E_{p'}}}\, \overline{u}_\alpha(p', s') \mathcal{O}^{\alpha\mu\beta} u_\beta(p, s) \tag{8.31}$$

where $u_\alpha(p, s)$ is a Rarita-Schwinger spin-vector. The following Lorentz covariant form for the tensor

$$\mathcal{O}^{\alpha\mu\beta} = -g^{\alpha\beta} \left\{ a_1 \gamma^\mu + \frac{a_2}{2M_B} P^\mu \right\} - \frac{q^\alpha q^\beta}{(2M_B)^2} \left\{ c_1 \gamma^\mu + \frac{c_2}{2M_B} P^\mu \right\}, \tag{8.32}$$

where $P = p' + p$, $q = p' - p$ and M_B is the mass of the baryon, satisfies the standard requirements of invariance under time reversal, parity, G-parity and gauge transformations. The parameters a_1, a_2, c_1 and c_2 are independent covariant vertex functions.

The multipole form factors are defined in terms of the covariant vertex functions through the following Lorentz invariant expressions [212],

$$\mathcal{G}_{E0}(q^2) = (1 + \frac{2}{3}\tau) \{a_1 + (1+\tau) a_2\} - \frac{1}{3}\tau(1+\tau) \{c_1 + (1+\tau) c_2\}\,, \tag{8.33}$$

$$\mathcal{G}_{E2}(q^2) = \{a_1 + (1+\tau) a_2\} - \frac{1}{2}(1+\tau) \{c_1 + (1+\tau) c_2\}\,, \tag{8.34}$$

$$\mathcal{G}_{M1}(q^2) = (1 + \frac{4}{5}\tau) a_1 - \frac{2}{5}\tau(1+\tau) c_1\,, \tag{8.35}$$

$$\mathcal{G}_{M3}(q^2) = a_1 - \frac{1}{2}(1+\tau) c_1\,, \tag{8.36}$$

with $\tau = -q^2/(2M_B)^2$ (≥ 0). The multipole form factors $\mathcal{G}_{E0}$, $\mathcal{G}_{E2}$, $\mathcal{G}_{M1}$ and $\mathcal{G}_{M3}$ are referred to as the charge ($E0$), electric-quadrupole ($E2$), magnetic-dipole ($M1$) and magnetic-octupole ($M3$) multipole form factors.

Similar to the octet case, the preferred ratio of two- and three-point Green functions for decuplet baryons is,

$$\begin{aligned} R_\sigma{}^\mu{}_\tau(t_2,t_1;\vec{p}\,',\vec{p};\Gamma) &= \left(\frac{\left\langle\, G^{Bj^\mu B}_{\sigma\tau}(t_2,t_1;\vec{p}\,',\vec{p};\Gamma)\,\right\rangle \left\langle\, G^{Bj^\mu B}_{\sigma\tau}(t_2,t_1;\vec{p},\vec{p}\,';\Gamma)\,\right\rangle}{\left\langle\, G^{BB}_{\sigma\tau}(t_2;\vec{p}\,';\Gamma_4)\,\right\rangle \left\langle\, G^{BB}_{\sigma\tau}(t_2;\vec{p};\Gamma_4)\,\right\rangle} \right)^{1/2} \\ &\simeq \left(\frac{E_p+M}{2E_p} \right)^{1/2} \left(\frac{E_{p'}+M}{2E_{p'}} \right)^{1/2} \overline{R}_\sigma{}^\mu{}_\tau(\vec{p}\,',\vec{p};\Gamma)\,. \end{aligned} \tag{8.37}$$

There is no implied sum over σ and τ in Eq. (8.37). Also, the square root in Eq. (8.37) spoils the covariant/contraviant nature of $R_\sigma{}^\mu{}_\tau$ and no meaning should be attached to the location of the indices. We still prefer this notation due to the close connection with $G^{Bj^\mu B}_{\sigma\tau}$.

After performing a slightly more complex calculation, using the Rarita-Schwinger spin sum of Eq. (8.16), one finds that the multipole form factors may be isolated and extracted from the following combinations of $\overline{R}_\sigma{}^\mu{}_\tau(\vec{p}\,',\vec{p};\Gamma)$[3]

$$\mathcal{G}_{E0}(q^2) = \frac{1}{3}\left(\overline{R}_1{}^4{}_1(\vec{q}_1,0;\Gamma_4) + \overline{R}_2{}^4{}_2(\vec{q}_1,0;\Gamma_4) + \overline{R}_3{}^4{}_3(\vec{q}_1,0;\Gamma_4)\right), \tag{8.38}$$

$$\mathcal{G}_{E2}(q^2) = 2\frac{M(E+M)}{|\vec{q}_1|^2}\left(\overline{R}_1{}^4{}_1(\vec{q}_1,0;\Gamma_4) + \overline{R}_2{}^4{}_2(\vec{q}_1,0;\Gamma_4) - 2\,\overline{R}_3{}^4{}_3(\vec{q}_1,0;\Gamma_4)\right), \tag{8.39}$$

$$\mathcal{G}_{M1}(q^2) = \frac{3}{5}\frac{E+M}{|\vec{q}_1|}\left(\overline{R}_1{}^3{}_1(\vec{q}_1,0;\Gamma_2) + \overline{R}_2{}^3{}_2(\vec{q}_1,0;\Gamma_2) + \overline{R}_3{}^3{}_3(\vec{q}_1,0;\Gamma_2)\right), \tag{8.40}$$

$$\mathcal{G}_{M3}(q^2) = 4\frac{M(E+M)^2}{|\vec{q}_1|^3}\left(\overline{R}_1{}^3{}_1(\vec{q}_1,0;\Gamma_2) + \overline{R}_2{}^3{}_2(\vec{q}_1,0;\Gamma_2) - \frac{3}{2}\,\overline{R}_3{}^3{}_3(\vec{q}_1,0;\Gamma_2)\right), \tag{8.41}$$

where $\vec{q}_1 = (q,0,0)$. We note that smaller statistical uncertainties may be obtained for $\mathcal{G}_{E2}$ by using the symmetry

$$\overline{R}_2{}^4{}_2(\vec{q}_1,0;\Gamma_4) = \overline{R}_3{}^4{}_3(\vec{q}_1,0;\Gamma_4)\,, \tag{8.42}$$

in Eq. (8.39). Hence, one typically defines an average $\overline{R}^4_{\rm avg}$ as

$$\overline{R}^4_{\rm avg}(\vec{q}_1,0;\Gamma_4) = \frac{1}{2}\left[\overline{R}_2{}^4{}_2(\vec{q}_1,0;\Gamma_4) + \overline{R}_3{}^4{}_3(\vec{q}_1,0;\Gamma_4)\right]. \tag{8.43}$$

With this definition the expression for $\mathcal{G}_{E2}(q^2)$ most commonly used in simulations is

$$\mathcal{G}_{E2}(q^2) = 2\frac{M(E+M)}{|\vec{q}_1|^2}\left(\overline{R}_1{}^4{}_1(\vec{q}_1,0;\Gamma_4) - \overline{R}^4_{\rm avg}(\vec{q}_1,0;\Gamma_4)\right). \tag{8.44}$$

[3]Reduce code for performing this calculation is provided in App. F

8.2.5 Quark sector contributions

The baryon form factors are calculated on a quark-sector by quark-sector basis with each sector normalised to the contribution of a single quark with unit charge. For example, the d-quark sector contribution to the Δ^+ three-point correlation function is given by

$$\begin{aligned} T\Big(\chi_\mu^{\Delta^+}(x_2)\, j^\alpha(x_1)\, \overline{\chi}_\nu^{\Delta^+}(0)\Big)_d = \frac{1}{3}\,\epsilon^{abc}\epsilon^{a'b'c'}\Big\{ \\ + 4\widehat{S}_d^{aa'}\,\gamma_\nu\, C S_u^{Tbb'} C\,\gamma_\mu\, S_u^{cc'} + 2\widehat{S}_d^{aa'}\, tr\left[\gamma_\nu\, C S_u^{Tbb'} C\,\gamma_\mu\, S_u^{cc'}\right] \\ + 4S_u^{aa'}\,\gamma_\nu\, C \widehat{S}_d^{Tbb'} C\,\gamma_\mu\, S_u^{cc'} + 2S_u^{aa'}\, tr\left[\gamma_\nu\, C \widehat{S}_d^{Tbb'} C\,\gamma_\mu\, S_u^{cc'}\right] \\ + 4S_u^{aa'}\,\gamma_\nu\, C S_u^{Tbb'} C\,\gamma_\mu\, \widehat{S}_d^{cc'} + 2S_u^{aa'}\, tr\left[\gamma_\nu\, C S_u^{Tbb'} C\,\gamma_\mu\, \widehat{S}_d^{cc'}\right]\Big\}. \end{aligned} \tag{8.45}$$

Hence to calculate the corresponding baryon property, each quark sector contribution should be multiplied by the appropriate charge and quark number. Under such a scheme for a generic form factor f, the Δ^+ form factor, f_{Δ^+}, is obtained from the u- and d-quark sectors normalised for a single quark of unit charge via

$$f_{\Delta^+} = 2 \times \frac{2}{3} \times f_u + 1 \times \left(-\frac{1}{3}\right) \times f_d\,. \tag{8.46}$$

8.2.6 Charge radii and magnetic moments

We now discuss how the charge radii and magnetic moments of the octet and decuplet baryons can be extracted from the calculated form factors. In this section it should be understood that $\mathcal{G}_E$, ($\mathcal{G}_M$) denotes both the octet electric (magnetic) form factor, and the decuplet $\mathcal{G}_{E0}$, ($\mathcal{G}_{M1}$) form factor.

It is well known that the experimental electric (and magnetic) form factor of the proton is well described by a dipole ansatz at small Q^2

$$\mathcal{G}_E(Q^2) = \frac{\mathcal{G}_E(0)}{\left(1 + Q^2/m^2\right)^2}\,; \quad Q^2 \geq 0\,. \tag{8.47}$$

This behaviour has also been observed in recent lattice calculations [214]. Using this observation, together with the standard small Q^2 expansion of the Fourier transform of a spherical charge distribution,

$$\left\langle r_E^2 \right\rangle = -6\frac{d}{dQ^2}\mathcal{G}_E(Q^2)\,\Big|_{Q^2=0}\,, \tag{8.48}$$

we arrive at an expression which allows us to calculate the electric charge radius of a baryon using our two available values of the Sachs electric form factor ($\mathcal{G}_E(Q^2_{\rm min})$, $\mathcal{G}_E(0)$), namely

$$\frac{\left\langle r_E^2 \right\rangle}{\mathcal{G}_E(0)} = \frac{12}{Q^2}\left(\sqrt{\frac{\mathcal{G}_E(0)}{\mathcal{G}_E(Q^2)}} - 1\right)\,. \tag{8.49}$$

However to calculate the charge radii of the neutral baryons, the above equation cannot be used, due to the fact that in those cases $\mathcal{G}_E = 0$. For the neutral baryons it becomes

a simple matter to construct the charge radii by first calculating the charge radii for each quark sector. These quark sectors are then combined using the appropriate charge and quark number factors as described in Sec. 8.2.5 to obtain the total baryon charge radii. Indeed all baryon charge radii, including the charged states, are calculated in this manner.

The magnetic moment is provided by the value of the magnetic form factor at zero momentum transfer, $Q^2 = 0$,

$$\mu = \mathcal{G}_M(0)\frac{e}{2M_B}\,, \tag{8.50}$$

in units of the natural magneton, where M_B is the mass of the baryon. Since the magnetic form factors must be calculated at a finite value of momentum transfer, Q^2, the magnetic moment must be inferred from our results, $\mathcal{G}_M(Q^2)$, obtained at the minimum non-vanishing momentum transfer available on our periodic lattice. We choose to scale our results from $\mathcal{G}_M(Q^2)$ to $\mathcal{G}_M(0)$. We do this by assuming that the Q^2 dependence of the electric and magnetic form factors are similar at the quark masses simulated herein. This is supported by experiment where the proton ratio $\frac{\mathcal{G}_M(Q^2)}{\mu\,\mathcal{G}_E(Q^2)} \simeq 1$ for values of Q^2 similar to that probed here. In this case

$$\mathcal{G}_M(0) = \frac{\mathcal{G}_M(Q^2)}{\mathcal{G}_E(Q^2)}\,\mathcal{G}_E(0)\,. \tag{8.51}$$

We apply Eq. (8.51) to the individual quark sectors for both the proton and Δ^+ baryons. Baryon properties can then be reconstructed using Eq. (8.46).

8.3 Lattice techniques

The three-point functions discussed in Sec. 8.2 are constructed using the sequential source technique outlined in Refs. [206, 211, 215]. For the quenched simulation we report our earlier results of Ref. [205]. The gauge fields were generated with the $\mathcal{O}(a^2)$ mean-field improved Lüscher-Weisz plaquette plus rectangle gauge action [80] using the plaquette measure for the mean link. The simulations were performed on a $20^3 \times 40$ lattice with a lattice spacing of 0.128 fm as determined by the Sommer scale [216] $r_0 = 0.50$ fm. This provides a spatial length of 2.56 fm, enabling safe simulations at the lowest pion mass of 300 MeV. The large volume lattice also ensures a good density of low-lying momenta which are key to giving rise to chiral non-analytic behaviour in the observables simulated on the lattice [217, 218]. A high-statistics analysis using a large sample of 400 configurations was used for the lightest eight quark masses. We also considered a subset of 200 configurations for the three heaviest quark masses in order to explore the approach to the heavy-quark regime, however these results won't be reproduced here.

For our present calculation we use dynamical gauge fields provided by the PACS-CS collaboration [21] and obtained using the International Lattice Data Grid (ILDG) [219]. The ensembles consist of $32^3 \times 64$ lattices with a continuum lattice spacing of $a = 0.0907(3)$ fm. The gauge fields were generated using a NP-clover improved-fermion action with $C_{SW} = 1.715$ and the Iwasaki gauge action [220].

We consider two values of the pion mass, $m_\pi = 296$, and 701 MeV. This allows us to both investigate the expected chiral curvature in the light mass regime, and the prediction from the constituent quark model, which should hold at heavy quark masses. The Sommer scale, with $r_0 = 0.50$ fm, gives an estimate of $a = 0.095(1)$, and $0.102(1)$ fm for the configurations at the light and heavy pion masses respectively. These compare favourably with the lattice spacings from the Lüscher-Weisz gauge configurations.

For the original Lüscher-Weisz configurations we used a fat-link irrelevant clover (FLIC) Dirac operator [27] which provided $\mathcal{O}(a)$ improvement [28]. For the present calculation we prefer to match the fermion action used in creating the gauge fields and use a NP-clover Dirac operator with $C_{SW} = 1.715$, such that we have $\mathcal{O}(a)$ improvement. For the vector current, we use an $\mathcal{O}(a)$-improved conserved vector current [213]. We use fixed boundary conditions and consider a Gaussian smeared source [221] at $t_0 = 16$, with smearing parameter [222] $\alpha = 0.7$, and 50 sweeps of smearing. The current insertion is centred at $t_1 = 23$.

In order to improve systematics we use the U^* trick [223], which is discussed in App. D. The error analysis of the correlation function ratios is performed via a third-order, single-elimination jackknife, with the χ^2 per degree of freedom (χ^2_{dof}) obtained via covariance matrix fits. We perform a series of fits through the ratios after the current insertion at t_1. By examining the χ^2_{dof} we are able to establish a valid window through which we may fit in order to extract our observables. In some instances we select fits to ensure that fit windows agree between different baryon. We can therefore be confident that any differences in the results are a result of the different baryons under consideration. The values of the static quantities quoted in this paper on a per quark-sector basis correspond to values for single quarks of unit charge.

The following calculations are performed in the lab frame $\vec{p} = 0$, $\vec{p}\,' = \vec{q} = |\vec{q}|\,\widehat{x}$ at $|\vec{q}|a = 2\pi/L_x$ with $L_x = 20$ for the quenched ensemble and $L_x = 32$ for the dynamical ensemble. Although the values of q^2 differ, our focus is on a reconstruction of the magnetic moment at $q^2 = 0$. Where a spatial direction of the electromagnetic current is required, it is chosen to be the z-direction.

Because lattice momenta are restricted to discrete values, the decay $\Delta \to \pi N$ cannot occur due to energy conservation if the Δ is initially stationary. On the light dynamical ensemble, the stationary Δ has energy $E_\Delta = m_\Delta \sim 1.45$ GeV. To decay into a nucleon and pion moving in opposite directions requires at least $E_N + E_\pi = \sqrt{m_N^2 + |\vec{q}|^2} + \sqrt{m_\pi^2 + |\vec{q}|^2} \sim 1.69$ GeV. Stationary Δ particles are therefore stable on our lattice. If we consider the case where a moving Δ decays into a moving proton and a stationary pion, then we find that the initial energy $E_\Delta \sim 1.50$ GeV, and the final energy $E_N + m_\pi \sim 1.50$ GeV. Because the Δ and πN states have degenerate energies one would therefore expect that a mixed Δ, πN state will exist on the lattice. In this case the usual technique of evolving through Euclidean time may not isolate the Δ ground state. However, we use three quark interpolating fields to excite and annihilate the Δ from the vacuum. We therefore expect that the overlap with the five quark πN state to be small, and for the majority of the spectral strength to be provided by contributions from the Δ. With this assumption we proceed in the usual manner.

We note that the scales for the NP-clover dynamical and Lüscher-Weisz quenched ensembles differ. In order to remove any ambiguity in comparing the results it is therefore

beneficial to consider ratios of lattice quantities. Fortunately, this is exactly what we wish to do. As we are working in the scaling regime, any differences resulting from the different lattice spacings should therefore be largely eliminated in our results.

8.4 Expectations

In the simple constituent quark model the magnetic moments of the proton and Δ^+ can be expressed as (see e.g. Ref. [224]),

$$\begin{aligned} \mu_p &= \frac{4}{3}\mu_u - \frac{1}{3}\mu_d \,, \\ \mu_{\Delta^+} &= 2\mu_u + \mu_d \,, \end{aligned} \tag{8.52}$$

where $\mu_{u,d}$ represent the intrinsic magnetic moments of the constituent u, d quarks. If we assume that the constituent u, d quark masses are degenerate then this implies that,

$$\begin{aligned} \mu_u &= \frac{2}{3}\frac{e\,\hbar}{2\,m_u\,c} \\ &= -\frac{1}{2}\left(-\frac{1}{3}\frac{e\,\hbar}{2\,m_d\,c}\right) \\ \mu_u &= -\frac{1}{2}\mu_d \,. \end{aligned} \tag{8.53}$$

If we consider the ratio of the proton magnetic moment over the Δ^+ magnetic moment,

$$\begin{aligned} \frac{\mu_p}{\mu_{\Delta^+}} &= \frac{4/3\,\mu_u - 1/3\,\mu_d}{2\,\mu_u + \mu_d} \\ &= \frac{3/2\,\mu_u}{3/2\,\mu_u} \\ \frac{\mu_p}{\mu_{\Delta^+}} &= 1 \,, \end{aligned} \tag{8.54}$$

we see that in this simple model it is 1. However, this model doesn't take into account explicit meson cloud contributions to the magnetic moments. Therefore, one would only expect this result to hold at unphysically large quark (i.e. pion) masses.

The "Access" quark model provides a formalism for extrapolating from the heavy quark region into the chiral regime [225]. The model uses both leading and also the next-to-leading non-analytic (NLNA) structure of chiral perturbation theory (χPT) in the extrapolation function. In Fig. 8.2 we reproduce a plot from Ref. [225] showing the extrapolation of the proton and Δ^+ magnetic moments. At heavier masses the moments are equal as discussed above. However, as the chiral regime is approached the proton magnetic moment is slightly larger than that for the Δ^+ due to differences in the chiral non-analytic behaviour.

A key difference is associated with the $\Delta \to N\pi$ dressing. Curvature associated with this non-analytic behaviour appears at larger pion masses near the N-Δ mass splitting, $m_\pi \sim M_\Delta - M_N$. As described below, quenched-QCD decay-channel contributions come

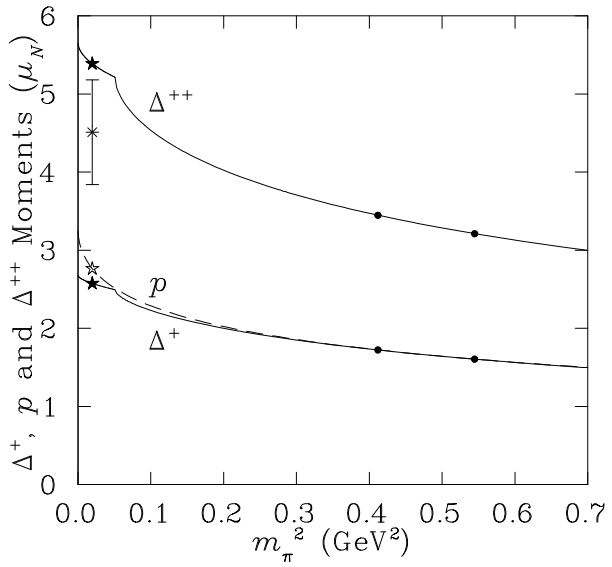

Figure 8.2: An extrapolation of the proton and Δ^+ magnetic moments in nuclear magnetons. The extrapolation used the "Access" quark model and included next-to-leading non-analytic terms. Figure reproduced from Ref. [225].

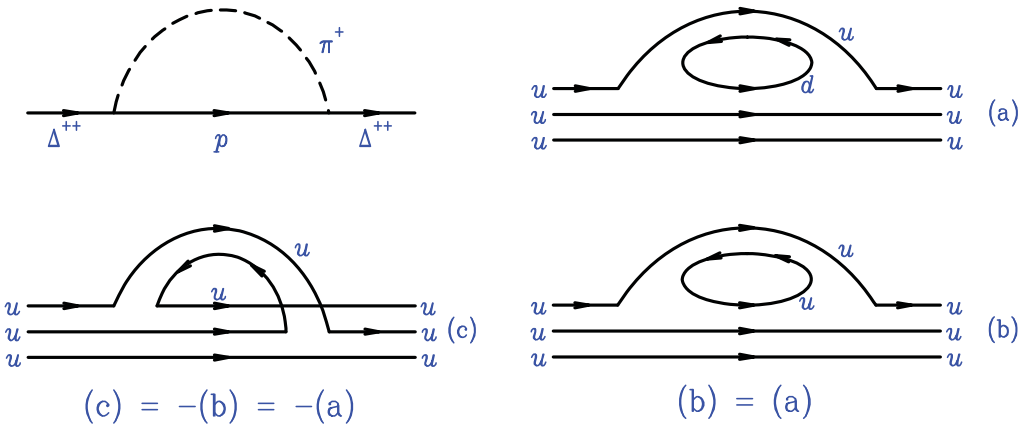

Figure 8.3: Quark-flow diagrams for the meson-cloud contributions to the Δ^{++} in full QCD.

with a sign opposite to that of full QCD. This artifact holds tremendous promise for revealing unmistakable signatures of the quenched meson cloud.

The change in sign for the decay-channel contributions is easily understood through the consideration of the quark flow diagrams in Fig. 8.3, illustrating the meson-cloud contributions to the Δ^{++} resonance in full QCD. Quark flow diagram (a) corresponds to the hadronic process described in the top left diagram of Fig. 8.3. Since QCD is flavor-blind, the process illustrated in diagram (b) is equivalent to diagram (a) provided the masses of the u and d quarks are taken to be equal. On its own, diagram (b) describes the decay of the Δ^{++} to a doubly-charged uuu "proton," which we denote p^{++}. Of course, such states do not exist in full QCD and diagram (c) provides a contribution which is exactly equal but opposite in sign to diagram (b) when the intermediate state is a uuu proton. Upon quenching the theory, both diagrams (a) and (b) are eliminated, leaving only diagram (c). Hence the physics of the $\Delta \to N\pi$ decay is present in the quenched approximation [226] but its contribution has the wrong sign.

We therefore expect that this calculation will expand upon the results of earlier chapters, by revealing the physical differences introduced by the inclusion of the dynamical sea degrees of freedom. In the quenched approximation we expect the μ_{Δ^+}/μ_p ratio to show significant curvature at lighter quark masses. For the dynamical simulation we still expect the ratio to remain much closer to 1, as illustrated in Fig. 8.2.

8.5 Quenched results

We now provide a summary of our earlier results using the Lüscher-Weisz gauge configurations. We focus primarily on the Δ baryon, however extensive results for the entire baryon decuplet are provided in Ref. [205]. Figures showing sample fits of the effective mass and form factor correlation functions were also provided, and so won't be repeated here. For the proton we include results from Ref. [213] which used the same Lüscher-Weisz gauge configurations.

Figure 8.4 is a plot of the proton and Δ baryon masses from the quenched calculations. The mass of the Δ baryon begins to show a small upward chiral curvature as the m_π^2 becomes lighter. This behaviour, anticipated in χEFT, has already been discussed in Refs. [111, 227, 228]. The numerical values of the masses are available in the relevant references.

The quark sector contributions to the electric form factor of the proton is shown in Fig. 8.5 and for the Δ in Fig. 8.6. Calculations on the lattice are performed using degenerate up and down quark masses. One consequence of this approximation is that the up and down quark sector contributions to the three-point correlation function of the Δ baryon (normalised to the contribution of a single quark) are exactly equal. All form factors for the Δ^+ can therefore be calculated using $f_{\Delta^+} = 2 \times \frac{2}{3} \times f_u + 1 \times \frac{-1}{3} \times f_d = f_{u,d}$. Similarly, the electromagnetic form factors for the Δ^0 are all exactly zero and we have $f_{\Delta^{++}} = 2\, f_{\Delta^+}$, and $f_{\Delta^-} = -f_{\Delta^+}$.

Note that at the light quark masses, we fit the change in the form factor correlation function from one quark mass to the next and add this to the previous result at the heavier quark mass. This approach provides significant cancellation of correlated systematic errors and makes the selection of the fit regime transparent. Greater detail is

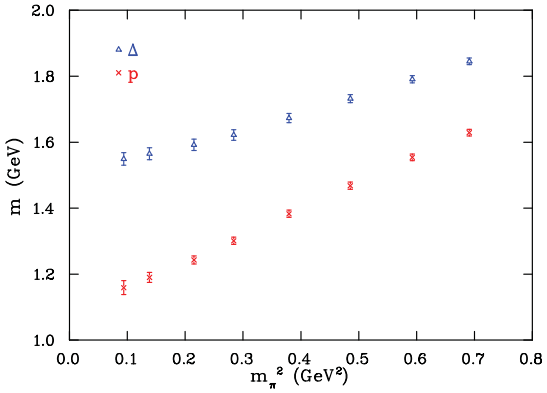

Figure 8.4: Masses of the proton and Δ baryon as a function of the squared pion mass from the quenched calculations [205, 213].

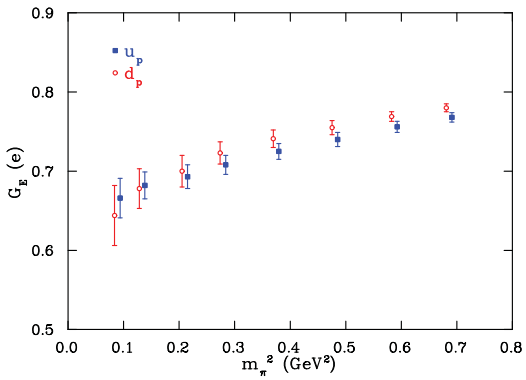

Figure 8.5: Quark sector contributions to the proton $\mathcal{G}_E$ electric form factor from the quenched calculation. The values for the d quark are slightly offset for clarity.

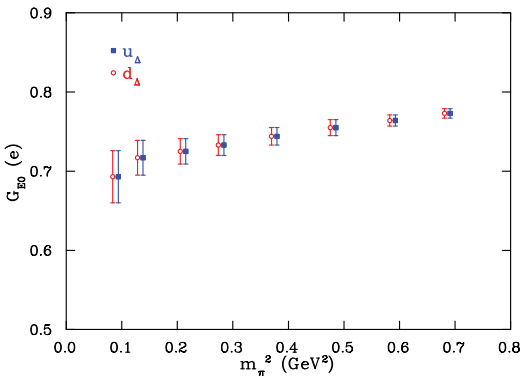

Figure 8.6: Quark sector contributions to the Δ^+ $\mathcal{G}_{E0}$ electric form factor. The values for the d quark are slightly offset for clarity.

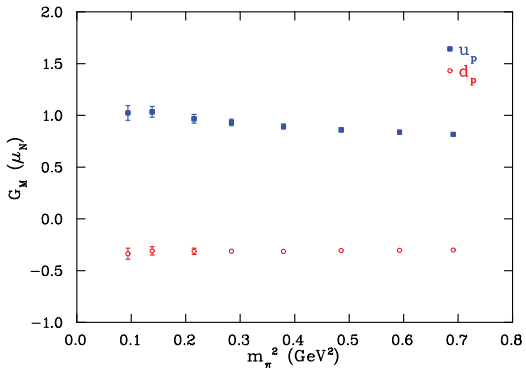

Figure 8.7: Quark sector contributions to the proton $\mathcal{G}_M$ magnetic form factor from the quenched calculation.

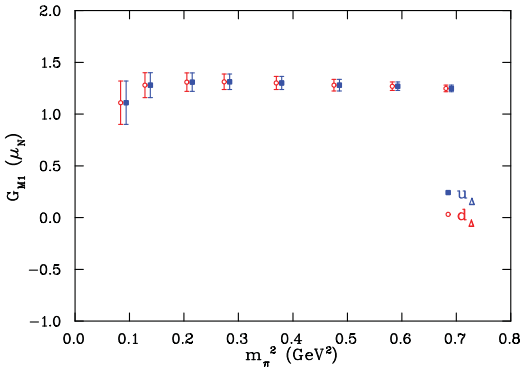

Figure 8.8: Quark sector contributions to the Δ^+ $\mathcal{G}_{M1}$ magnetic form factor. The values for the d quark are slightly offset for clarity.

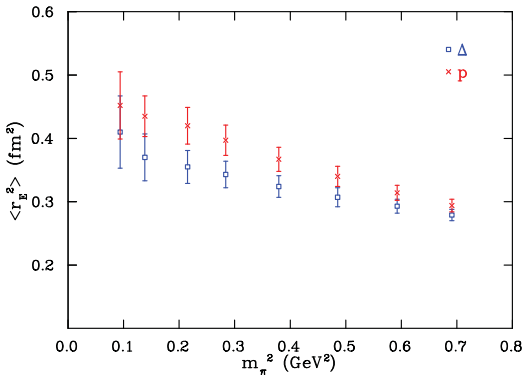

Figure 8.9: The electric charge radii of the proton and Δ^+ baryon from the quenched calculation.

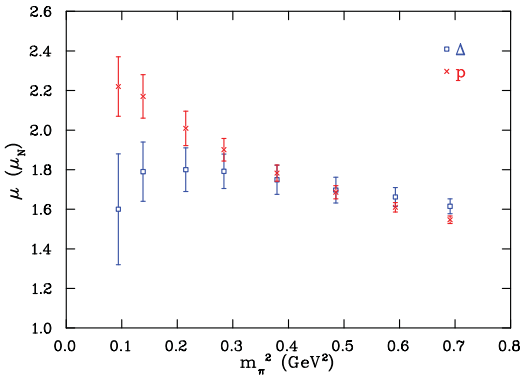

Figure 8.10: The magnetic moment of the Δ^+ baryon from the quenched calculation compared with the magnetic moment of the proton.

provided in Refs. [205, 213].

The quark sector contributions to the magnetic form factors $\mathcal{G}_M$ and $\mathcal{G}_{M1}$ for the proton and Δ are shown in Figs. 8.7 and 8.8 respectively. Here we report results in units of the nuclear magneton, $e/(2\,m_N)$ by multiplying the lattice results by the ratio $m_N/m_{p,\Delta}$. We note the beginning of chiral curvature at the lightest pion mass in Fig. 8.8.

8.5.1 Charge radii and magnetic moments

The charge radius and magnetic moment are calculated from the electromagnetic form factors using the techniques described in Sec. 8.2.6. The charge radii of the proton and Δ^+, as a function of the pion mass, are plotted in Fig. 8.9, and the magnetic moment is shown in Fig. 8.10.

The differences in the magnetic moments of the proton and Δ^+ seen in Fig. 8.10 are particularly interesting. In Fig. 8.11 we show the ratio μ_{Δ^+}/μ_p. As already discussed, the physics of the $\Delta \to N\pi$ decay comes with the wrong sign in the quenched simulation.

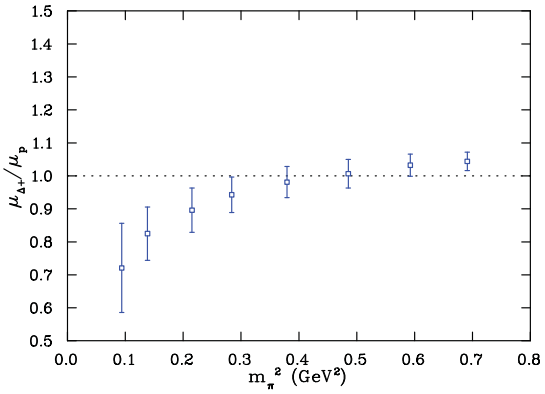

Figure 8.11: The ratio μ_{Δ^+}/μ_p for the quenched calculation. There is a strong negative chiral curvature at light quark masses.

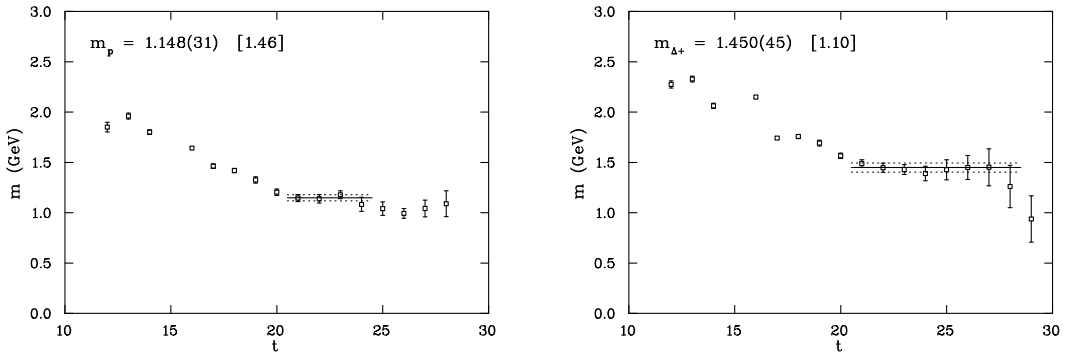

Figure 8.12: Effective mass plots for the proton (left) and Δ^+ (right) baryons at $m_\pi = 296$ MeV as a function of Euclidean time. χ^2_{dof} are given in square brackets next to the fit result.

This leads to the strong negative chiral curvature seen in Fig. 8.11. This is where we will focus our attention for the dynamical calculation.

8.6 Dynamical results

We now present our results for the electromagnetic form factors of the proton and Δ^+ in dynamical QCD. Focusing on the μ_{Δ^+}/μ_p ratio, we expect that the chiral curvature seen in Fig. 8.11 will be suppressed following the inclusion of dynamical sea quarks, and that the ratio will remain much closer to 1. In the following we refer to the two dynamical ensembles as the "light" and "heavy" ensembles for the configurations with pseudoscalar masses $m_\pi = 296$ and 701 MeV respectively.

The effective mass plots for the proton and Δ^+ masses are shown in Figs. 8.12 and 8.13 for the light and heavy ensembles respectively. For the light ensemble we find that $m_p = 1.15(3)$ GeV, and $m_{\Delta^+} = 1.45(5)$ GeV. For the heavy ensemble we find that $m_p = 1.43(2)$ GeV, and $m_{\Delta^+} = 1.68(3)$ GeV.

The fit results for the electric and magnetic form factors at the light mass of $m_\pi = 296$ MeV are shown in Figs. 8.14 and 8.15, along with the numerical values and χ^2_{dof}.

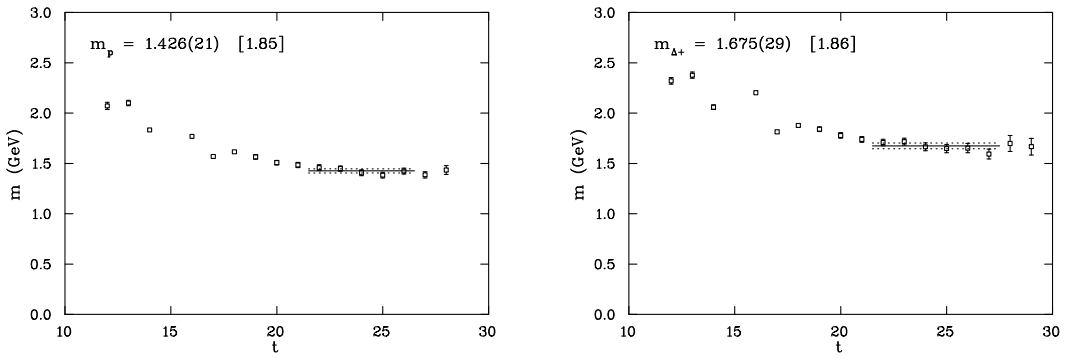

Figure 8.13: Effective mass plots for the proton (left) and Δ^+ (right) baryons at $m_\pi = 701$ MeV as a function of Euclidean time. χ^2_{dof} are given in square brackets next to the fit result.

Figures 8.16 and 8.17 show the fit results at the heavier mass of $m_\pi = 701$ MeV.

At the light mass, we see that for each form factor a clear plateau appears soon after the current insertion at $t_1 = 23$. In contrast to this, the heavier pion mass displays a systematic drift in both the electric and magnetic correlation functions. In order to obtain a reasonable χ^2_{dof} for each fit, this drifting forces one to select fits at larger Euclidean times. However, this means that the fits are taken from the tails of the correlation functions, where it is well known that the central values do not fairly represent the true ensemble average. For example, using the fits shown in Figs. 8.16 and 8.17, one obtains a value for the magnetic moment of the Δ^+ of 2.80(28) μ_N, which is far higher than the quenched result of 1.70(7) μ_N and comes with a much larger error. Similarly, for the proton one finds that $\mu_p = 2.08(13)$ μ_N in the dynamical case, which also does not agree with the quenched result, $\mu_p = 1.68(3)$ μ_N. At this heavy quark mass, one expects only small differences between quenched and full QCD. Certainly these differences should be smaller than those observed at light quark masses. These large discrepancies indicate that the fits seen in Figs. 8.16 and 8.17 are plagued by uncertainties and do not accurately represent the ensemble average.

We therefore perform a self consistent analysis between the light and heavy dynamical ensembles, where fits at the heavy pion mass are selected such that the Euclidean time scales match those at the lighter pion mass. In this way we ensure that any phenomenological differences in the final values are a direct result of the different quark masses used, and are not due to systematic errors introduced by fitting the tails of correlation functions.

Figure 8.18 shows the final result for the proton charge radius at both $m_\pi = 296$ and 701 MeV, compared with the previous quenched results. The Δ^+ charge radius is shown in Fig. 8.19. In both cases we see little change from the quenched results.

The magnetic moments of the proton and Δ^+ are shown in Figs. 8.20 and 8.21. The Δ^+ shows the greatest deviation from the quenched result. Since the two calculations are performed with different lattice spacings, we focus on the μ_{Δ^+}/μ_p ratio where scale dependence is largely eliminated.

For the magnetic moment ratio we find that $\mu_{\Delta^+}/\mu_p = 0.92(9)$ for the light ensemble and $\mu_{\Delta^+}/\mu_p = 1.07(3)$ for the heavy. A comparison with the quenched magnetic moment

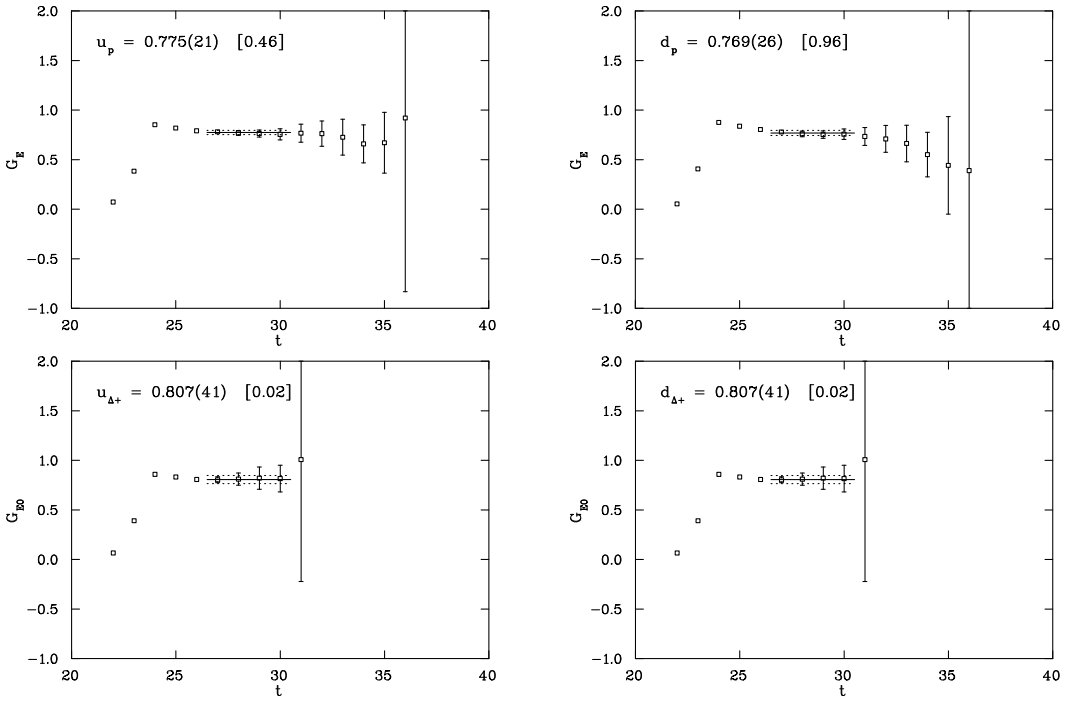

Figure 8.14: Contributions to the proton (top) and Δ^+ (bottom) electric form factors for the doubly represented u (left) and d (right) quark sectors at $m_\pi = 296$ MeV as a function of Euclidean time. χ^2_{dof} are given in square brackets next to the fit result.

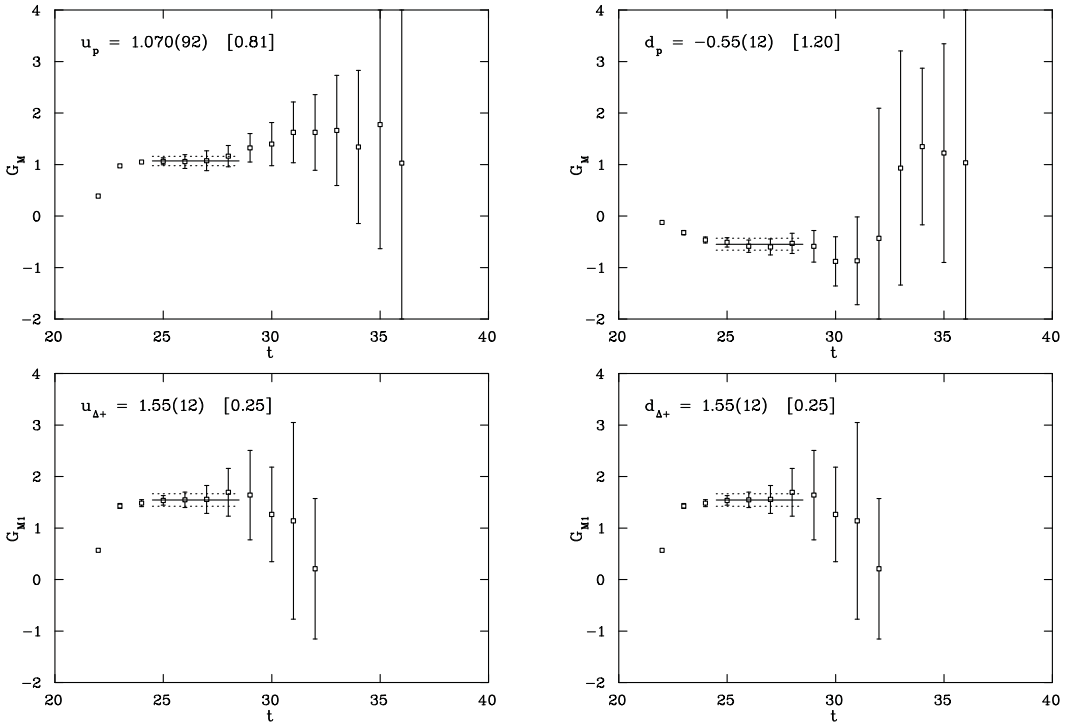

Figure 8.15: Contributions to the proton (top) and Δ^+ (bottom) magnetic form factors for the doubly represented u (left) and d (right) quark sectors at $m_\pi = 296$ MeV as a function of Euclidean time. χ^2_{dof} are given in square brackets next to the fit result.

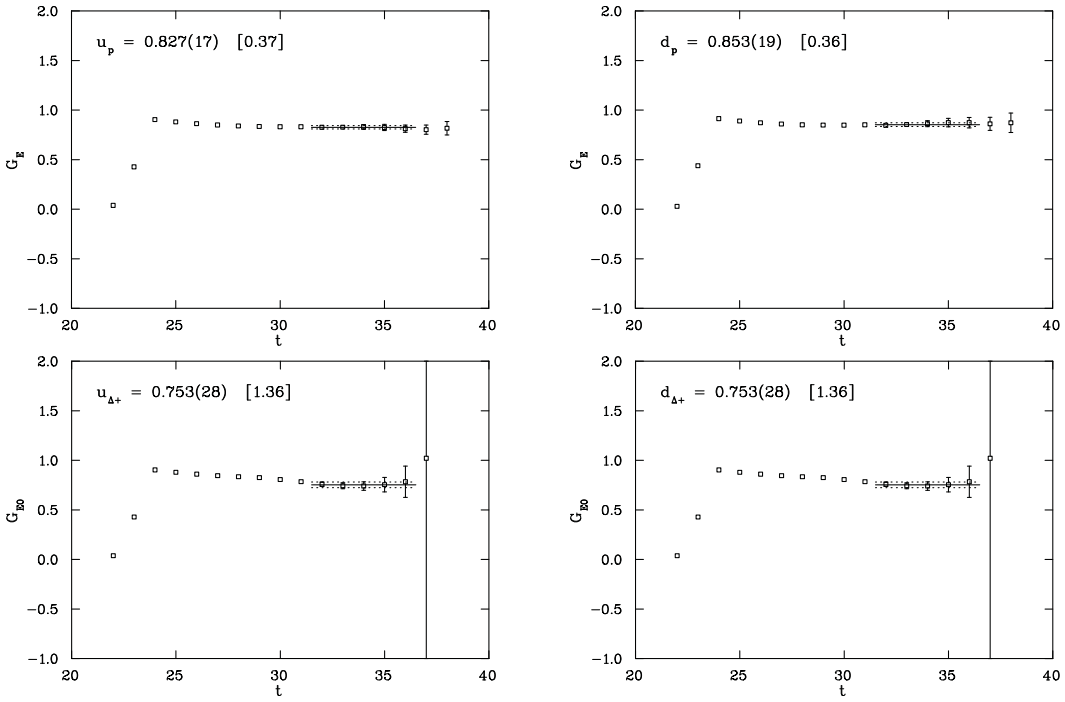

Figure 8.16: Contributions to the proton (top) and Δ^+ (bottom) electric form factors for the doubly represented u (left) and d (right) quark sectors at $m_\pi = 701$ MeV as a function of Euclidean time. χ^2_{dof} are given in square brackets next to the fit result.

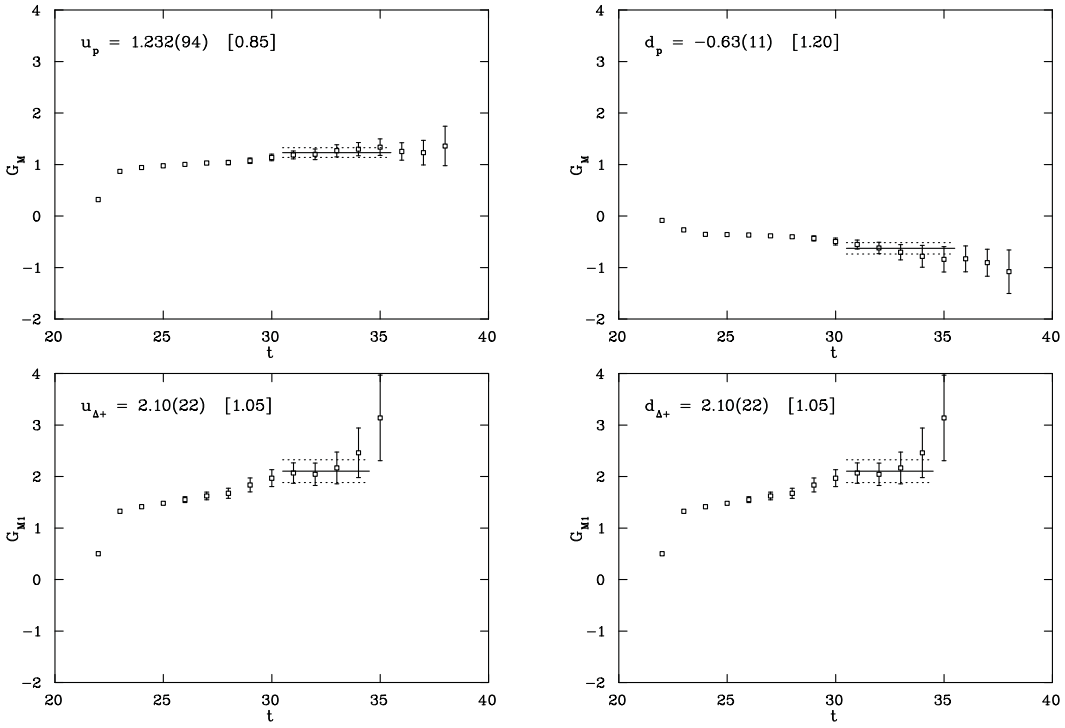

Figure 8.17: Contributions to the proton (top) and Δ^+ (bottom) magnetic form factors for the doubly represented u (left) and d (right) quark sectors at $m_\pi = 701$ MeV as a function of Euclidean time. χ^2_{dof} are given in square brackets next to the fit result.

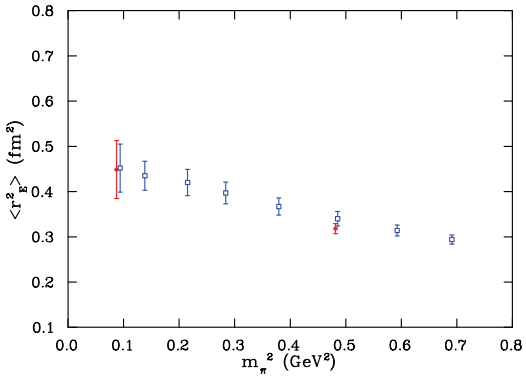

Figure 8.18: The charge radii of the proton calculated in dynamical QCD (full symbols) compared with the previous quenched results (open symbols).

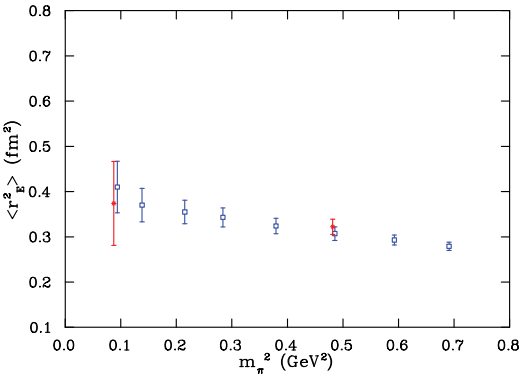

Figure 8.19: The charge radii of the Δ^+ calculated in dynamical QCD (full symbols) compared with the previous quenched results (open symbols).

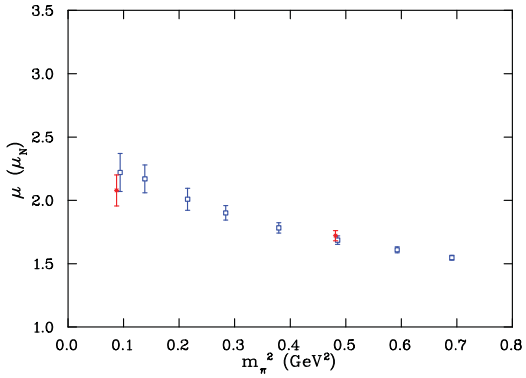

Figure 8.20: The magnetic moment of the proton calculated in dynamical QCD (full symbols) compared with the previous quenched results (open symbols).

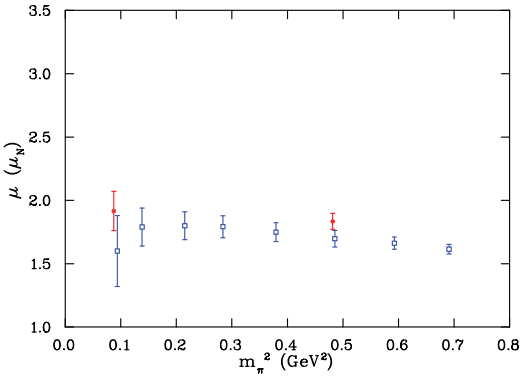

Figure 8.21: The magnetic moment of the Δ^+ calculated in dynamical QCD (full symbols) compared with the previous quenched results (open symbols).

	Proton		Δ^+	
m_π (MeV)	296	701	296	701
$\mathcal{G}_E$ (e)	0.776(26)	0.839(5)	0.807(41)	0.837(7)
$\mathcal{G}_M$ (μ_N)	1.61(10)	1.45(3)	1.55(12)	1.54(5)
$\langle r_E^2 \rangle$ (fm^2)	0.449(64)	0.318(11)	0.374(93)	0.322(17)
μ (μ_N)	2.08(12)	1.72(4)	1.92(16)	1.83(6)
μ_{Δ^+}/μ_p	0.92(9)	1.07(3)	0.92(9)	1.07(3)

Table 8.1: Collected final results for the proton and Δ^+ electromagnetic form factors, charge radii and magnetic moments from the dynamical calculation.

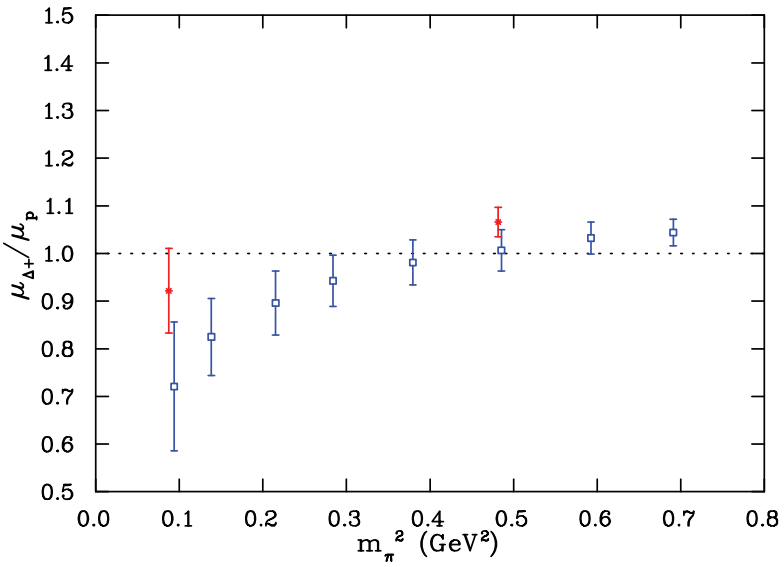

Figure 8.22: A comparison of the magnetic moment ratio μ_{Δ^+}/μ_p in dynamical QCD (full symbols) with quenched QCD (open symbols).

ratio is provided in Fig. 8.22. Here we see the expected suppression of the chiral curvature in the dynamical case. At the light pion mass the ratio agrees with 1 within errors, and supports the model of Ref. [225]. The central value suggests that the Δ^+ magnetic moment is still slightly smaller than the proton's at this mass. At the heavier pion mass the ratio is just above 1, agreeing with earlier Lattice QCD calculations [205, 206, 211, 213]. Quark Model considerations anticipate $\mu_{\Delta^+}/\mu_p > 1$, as hyperfine repulsion between constituent quarks leads to smaller effective masses and thus larger intrinsic moments in the Δ^+ [206]. The final numerical values from our calculation are listed in Table 8.1.

8.7 Summary

We have performed a calculation of the proton and Δ^+ charge radii and magnetic moments using dynamical NP-clover gauge fields. The results were compared with earlier calculations that used the quenched approximation [205, 213].

We demonstrated how the suppression of sea-quark loop contributions in quenched QCD reduces the Δ^+ magnetic moment considerably, and showed that in dynamical QCD the μ_{Δ^+}/μ_p ratio remains close to 1, as anticipated from models incorporating the non-analytic effects of χEFT. At large pion masses, the Δ^+ moment is enhanced relative to the proton moment in accord with earlier lattice QCD calculations [205, 206, 211, 213] and model expectations [206]. As the chiral regime is approached, the non-analytic behaviour of the quenched meson cloud starts to be revealed, enhancing the proton relative to the Δ^+, in accord with the expectations of QχPT.

While there are still more statistics to be gathered, this calculation represents an important first look into the effects of chiral dressings on the electromagnetic properties of baryons.

Chapter 9

Conclusions and outlook

This work has presented an extensive study on the differences between quenched and dynamical QCD vacuum structure. In order to facilitate this, a new over-improved stout-link smearing algorithm was formulated. As far as we aware, this is the first time link paths beyond the staple have been included in the stout-link smearing algorithm. This work highlights the importance of using improvement for topological studies of the QCD vacuum. The over-improved stout-link smearing algorithm is currently the most topologically stable smearing algorithm available in Lattice QCD.

The utility of over-improved stout-link smearing was demonstrated in both Chapters 3 and 6. The comparison with the overlap topological charge $q(x)$ revealed a strong correlation between topological objects in the QCD vacuum, regardless of the method used to extract $q(x)$. This chapter demonstrated how to tune the number of smearing sweeps n_{sw} against an UV cutoff λ_{cut} in the overlap operator, providing strong support for the use of smearing in studies of QCD vacuum structure. It would certainly be interesting to increase the statistics of this study to see if the relationship between λ_{cut} and n_{sw} can be strengthened. In this chapter we also observed an intimate relationship between the location of Dirac zero- (and near zero) modes, and the gluonic topological charge density.

Chapter 4 continued the comparison of smearing to the overlap operator by considering variations in the negative Wilson-mass in the overlap Dirac input kernel. Here we saw how the freedom usually associated with smearing algorithms, through the variable number of applied sweeps, also exists in the overlap operator through the Wilson-mass regulator parameter. This should be of interest both to Lattice researchers studying the QCD vacuum and to advocates of fat-link fermion actions. Whilst the effects may be small, it should be investigated further by anyone intending to use the overlap operator to make accurate physical predictions.

The use of smearing as a preconditioner for Maximal Centre Gauge fixing in Chapter 6 enabled a study of centre vortices in QCD. Here, in contrast to $SU(2)$, we showed that MCG gauge fixing is not sufficient to explain the essential non-perturbative features of the QCD vacuum.

The over-improved stout-link smearing algorithm was employed in Chapter 5 in order to probe the structure of the dynamical QCD vacuum. At short distances we observed the proposed, rapidly oscillating sheet-like structure of the vacuum. On longer scales, however, we also saw the more traditional instanton dominated picture of the vacuum

emerge. Importantly, we discussed how these two pictures can be considered complementary, and are not self-exclusive. Finally, when structure within the sheets is rendered, one discovers a speckled sandy structure in the topological charge density of the QCD vacuum.

The way in which this structure is affected by dynamical quarks was also studied. This analysis showed an increase in non-trivial topological charge fluctuations in the dynamical vacuum, leading to "rougher" gauge fields. Perhaps surprisingly, there was also an increase in the observed number of instanton-like objects. The reasons for this were discussed; that the increased density of instantons leads to fewer near zeromodes, which are suppressed by the inclusion of the fermion determinant in full QCD. An obvious extension here would be to consider the use of different lattice fermion actions. Unfortunately, at the current time differences in the lattice spacings and quark masses of the publicly available lattice ensembles prevent a thorough comparison. However, given time this will change, and this question should then be revisited.

Chapter 7 shifted the focus onto the quark propagator and examined the effects of smearing on the wave renormalisation and mass functions. This is currently of relevance given the increased use of fat-link fermion actions in modern simulations [106]. Here smearing was shown to have a strong effect on heavy quarks, but less of an effect at lighter masses. Nevertheless, at the lightest quark mass, a suppression of dynamical mass generation was observed, which may be of concern for fat-link actions. Clearly this should be investigated further, should fat-link actions become more common.

Finally, in Chapter 8 we returned to the issue of dynamical vacuum structure by investigating the effects of sea-quark loops on the electromagnetic properties of baryons. Focusing on the proton and Δ^+, we performed a dynamical calculation of the particles' charge radii and magnetic moments at a light pion mass of 296 MeV and a heavy mass of 701 MeV. Focusing on the μ_{Δ^+}/μ_p ratio, we showed how near the chiral limit, the addition of sea quark loops leads to a suppression of the negative chiral curvature observed in previous quenched results. This work could be extended to an analysis of the Ω^- in which chiral effects are also expected to be important and accurate experimental results are already available.